Testing and Interface Modeling of the Mechanical and Damping Behavior of Nanocrystalline Cellulose Reinforced Bio-based Polyamides

by

Yufeng Tian

A dissertation submitted in partial fulfillment
of the requirements for the degree of
Doctor of Philosophy
(Mechanical Sciences and Engineering)
in the University of Michigan-Dearborn
2022

Doctoral Committee:

Professor Alan Argento, Chair
Professor Hong Tae Kang
Wonsuk Kim, Associate Research Scientist
Associate Professor Joe Lo
Professor Ya Sha Yi

Yufeng Tian

yufengt@umich.edu

ORCID iD: 0000-0002-5992-3104

Dedication

To my parents, grandparents, and ancestors. Thank you.

Acknowledgements

I would like to thank my advisor Dr. Alan Argento for his guidance, trust, and support. Thank you for offering me the precious opportunity to participate in the research program when I was in my senior year at the undergraduate level. It has been a great time working in your bio-mechanical lab. I have learned so much about material testing, research, academic writing, and presentation skills. I very much appreciate your warm encouragement when I confront obstacles in research. It helps me get over the most difficult times. Moreover, thank you for advising me on the direction of the research so that I can contribute to my research field.

I am also grateful to Dr. Wonsuk Kim. Thank you for your kind guidance for the testing and for my research work. I am deeply influenced by your circumspective and professional character. You have always provided me with insightful suggestions for my work. The accomplishment of my research could not have begun without you.

Thanks also to my committee Dr. Alan Argento, Dr. Wonsuk Kim, Dr. HongTae Kang, Dr. Joe Fujiou Lo and Dr. Ya sha (Alex) Yi. Your expertise guides and supports me to accomplish my research work. Thank you for the commitment to serve on my committee.

I want to extend my special thanks to my cooperative partners in Ford Motor Company, including Alper Kiziltas, Deborah Mielewski, and Sandeep Tamrakar. Thank you for the support of the material supply and manufacturing equipment, the help and guidance for the sample production, and the opportunity to present my research work at conferences.

I would like to thank all of the current and former members of the bio-mechanical lab: Elise Kowalski, John Riesterer, Rana Dabaja, and Elizabeth Arroyo. It has been a pleasure to work with all of you. Many thanks to Elise Kowalski for your great work on microscopy, which is an essential part of my research publication. Thanks for the testing work of Rana Dabaja and John Riesterer. It is an important part of my testing results.

I want to recognize Geoffrey Hosker for the grammar check of my dissertation drafts. It is an incredible help for me, an international student, to finish my dissertation work.

I also wish to thank my family and friends: my father, Qiang Tian; my mother, Suxia Yang; my aunt, Sujuan Yang; my girlfriend, Jinghui Li; and my friends, Jinze Du, Jiahao Zhang, Xinrui Xia, Linyan Xiang, and Yu He. I would like to extend my deepest gratitude to my father and mother for the love and the effort that has supported me to become what I wish to be. Many thanks to my girlfriend. You give me the light when I feel lonely in the darkness. I am grateful to all of my friends for the support and the great time we have spent together. This joy helps me get through the hardships in my life.

Funding

This dissertation is based upon work supported by the National Science Foundation under Grant CMMI 1537360. Any opinions, findings, and conclusions or recommendations expressed in this material are those of the authors and do not necessarily reflect the views of the National Science Foundation. This support is gratefully acknowledged.

Table of Contents

List of Tables

List of Figures

List of Appendices

Abstract

Bio-based polyamide 610 (PA610) reinforced with micro- and nanocellulose were manufactured by melt compounding followed by injection molding. The resulting composites had fiber sizes ranging from nanoscale to 100 μm at 2.5%, 5% and 10% fiber mass fractions. These composites were mechanically characterized by tensile tests followed by scanning electron microscopy to examine the tensile fracture surface. The primary focus of the work was the damping behavior of these nanocomposites, which was found to be substantial. Damping was characterized using the damping ratio extracted from the measured decay of mechanical vibrations. Cellulose nanocrystal-reinforced PA610 at 10% mass fraction was found to produce a 210% increase in damping ratio compared to control PA610. Larger fiber sizes and lower mass fractions resulted in smaller, but significant, increases in damping. Comparison to cellulose reinforced polypropylene composites showed that PA610/cellulose composites produced significantly greater relative damping. Additionally, since both cellulose and PA610 are hydrophilic materials, a study was made on the effects of moisture absorption on the damping. It was found that the pronounced effect of the filler on damping was diminished by absorbed moisture and did not return after removing moisture from the samples. The origin of the damping increase and the effects of moisture were discussed in the dissertation.

A damping model was developed based on the mechanism of interfacial interaction in nanoscale particle reinforced composites. The model included the elasticity of the materials and the effects of interfacial adhesion hysteresis. The presence of hydrogen bonding at the interface between the particle and matrix and the large interfacial area due to the filler's nano size were shown to be the main causes of the high damping enhancement. The influence of other parameters, such as interfacial distance and stiffness of the matrix materials were also discussed. The modeling work can be used as a guide in designing composites with good damping properties.

Chapter 1 Introduction

1.1 Cellulose

The overuse of plastic has created or exacerbated many environmental problems such as plastic pollution and the greenhouse effect. The demand for biodegradable and renewable materials has increased in society. As one of the most abundant natural resources, cellulose has attracted increasing attention for replacing traditional petroleum-based materials.

1.1.1 Cellulose Sources

Studies have estimated that the production of cellulosic material is about 13 billion tons per year[1, 2]. Cellulose can be derived from several materials. (i) Wood is one of the most abundant sources in nature. Currently, there is mature and complete infrastructure to harvest and process wood. Cellulose can be extracted from processed wood with most of the impurities removed. (ii) Plants are another main cellulose source. Natural fibers consisting of cellulose, such as cotton [3, 4], sisal [5], and flax [6], have been studied and applied for centuries. Cellulose can be derived from these fibers. In addition to these traditional plants, agricultural residues, including palm trunks, empty fruit bunches, corncobs, wheat straw, coconut husks, and sugarcane bagasse [7], are attracting more attention in society. Transforming these low-cost wastes into cellulose material provides great potential for the material industry in the future. (iii) Bacteria can produce cellulose. The bacterium named Gluconacetobacter xylinus is the most commonly used. Under certain conditions, the bacteria secrete a gel consisting of cellulose micro fibrils and water. It is believed that the cellulose in the gel can be used to protect the bacteria from fungi and ultraviolet light. Studies have shown that the crystallization of the micro fibril can be altered by adjusting the culturing conditions [8]. (iv) Cellulose micro fibrils can be produced in the cell wall of certain species of algae. The structures of these cellulose micro fibrils vary among different species because of their unique biosynthesis processes. The cellulose micro fibrils from green algae (such as Micrasterias denticulata [9, 10] and Valonia [11] have been the most studied. (v) Tunicates are sea animals that can produce cellulose micro fibrils embedded in the protein matrix of their mantle. Similar to algae, the structures of the cellulose micro fibrils are slightly different between species because of the different formation processes [12]. The most common tunicate species that have been studied are Halocynthia roretzi [3], Halocynthia papillosa [13], and Metandroxarpa uedai [14].

1.1.2 Cellulose Structure

Consisting of ring-shaped glucose molecules, the shape of cellulose is normally like a long linear ribbon. The monomer (basic repeatable unit) in the cellulose chains is two connected anhydroglucose rings ($C_6H_{10}O_5$), as presented in Figure 1(a). The number of monomers in a single cellulose chain is usually from 10,000 to 15,000 [15], based on the specific sources. Note that each glucose ring is covalently bonded by an oxygen atom between two carbon atoms at position 1(C1) and 4(C4) in two rings, respectively, which is called the glucosidic bond [16]. The hydroxyl group attached to C3 creates an intramolecular hydrogen bonding connected to the oxygen atom in the adjacent glucose ring. Because of this hydrogen bonding, as well as the glucosidic bond between the glucose rings, the shape of the cellulose chain maintains a linear configuration. In addition, the hydroxyl groups at C6 and C2 play a role in the formation of hydrogen bonding between cellulose chains. The network of the intermolecular hydrogen bonding stabilizes the crystalline structure of the cellulose. Different structures of crystalline cellulose are formed, depending on the stacking directions and positions of the cellulose chains. As is shown in Figure 1(b) [15], a group of cellulose chains creates a cellulose fibril 5–50 nm in diameter. However, this highly crystallized structure (cellulose nanocrystals) is not consistent along the fibril. There are disordered regions between cellulose nanocrystals at intervals. This amorphous cellulose gives the fibril flexibility, while the highly crystallized region strengthens the stiffness of the fibril. The amorphous cellulose can be removed by acid hydrolysis. In contrast, cellulose nanocrystals remain in the process due to the insolubility gained from strong hydrogen bonding between cellulose chains (Figure 1(c)).

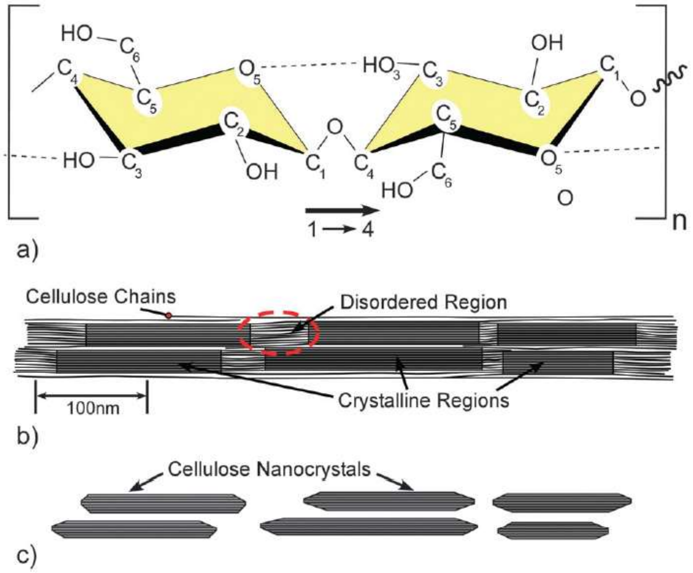

Figure 1.1. Schematics of (a) chemical structure of the unit of cellulose chains. with hydrogen bonding shown in dashed lines; (b) cellulose fibril consisting of crystalline and disordered regions; (c) remaining cellulose nanocrystals after acid dissolving (from [15]).

As mentioned above, the network of the hydrogen bonding between cellulose chains determines the chemical structure of crystalline cellulose. Such networks are generally categorized into type I, II, III, and IV according to their polymorphs [17]. Cellulose I is derived naturally from organisms, such as wood, plants, bacteria, etc. It is sometimes called “native cellulose.” Cellulose II and III can be obtained by specific treatments of cellulose I [17].

Additionally, cellulose I can be divided into two groups (Iα and Iβ). They have a triclinic (Iα) and a monoclinic (Iβ) structure, respectively. These two polymorphs commonly coexist in nature [17, 18], and their proportions depend on the specific species. Cellulose Iα is predominant in primitive organisms such as algae and bacteria, and cellulose Iβ is the dominant form in higher plants. Studies show that cellulose Iα can be transformed into cellulose Iβ by treatments in organic solvents and helium gas at high temperature [19] or by treatments in hot alkaline solution [20]. Only a portion of cellulose Iα can be successfully converted into cellulose Iβ, even if the parameters of the treatments are carefully controlled [19, 20]. The lattice structures of cellulose Iα and Iβ are characterized by synchrotron X-ray and neutron fiber diffraction in studies [21, 22]. The parameters of the unit Iα cell are a = 0.672 nm, b = 0.596 nm, c = 1.040 nm, α = 118.08˚, β = 114.80˚, γ = 80.375˚[22], and the parameters of the unit Iβ cell are a = 0.778 nm, b = 0.820 nm, c = 1.038 nm, γ = 96.5˚. The shape of the lattice structures can be seen in Figure 2.

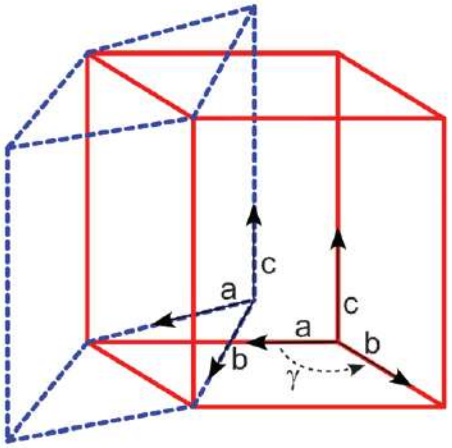

Figure 1.2. Schematics of the lattice for cellulose Iα (triclinic shape in dashed line) and cellulose Iβ (monoclinic shape in solid line) [15].

Cellulose II is found to have the highest stability and can be produced by regeneration and mercerization processes [23]. Studies show that cellulose II has a monoclinic unit cell structure with dimensions a = 0.810 nm, b = 0.903 nm, c = 1.031 nm, γ = 117.10˚[24]. Cellulose

III can be converted from cellulose I or II by liquid ammonia treatments [25]. It is reported to have a monoclinic unit cell with parameters a = 0.445 nm, b = 0.785 nm, c = 1.031 nm, γ = 105.1° [26]. Cellulose IV is obtained from cellulose II or III by treatment in glycerol at 260 °C [27]. This dissertation focuses on cellulose I, which is the material used in producing CNC/PA610 composites.

1.1.3 Production of Cellulose Fibrils and Particles

Cellulose materials can be produced from a variety of organisms. To obtain good mechanical properties, the impurities and amorphous regions need to be removed by treatments. The isolation of pure cellulose materials commonly requires two steps. The first step is purification and homogenization of the raw materials to remove the most irrelevant materials, which reduces the difficulties in the following processes. Specific pretreatments are needed for different source materials, depending on the degree of morphology of cellulose. For wood and plants, the matrix materials containing hemicellulose and lignin are removed by the treatments. Micro-sized cellulose fibers remain for the second steps [28, 29]. Deriving cellulose fibrils from tunicate requires removal of the protein matrix from the mantle [30]. For obtaining algae cellulose, the task is dealing with the algal wall matrix [10]. Bacterial cellulose pretreatments comprise not only the process of removing the residue of the bacteria but also the procedures for controlling the cellulose growth rate in the cells[31].

The second step is further purifying the cellulose material and separating larger-sized cellulose fiber into micro/nano cellulose fibrils or cellulose particles. The treatments include mechanical treatments, acid hydrolysis, and enzymatic hydrolysis [29]. To achieve a good purifying and separating effect, a combination of the above treatments should be applied to the materials. The mechanical treatments include grinding, cyrocrushing, and high-intensity ultrasonic treatments [15, 32]. The mechanism of these treatments is the production of high shear force between individual cellulose sub-fibrils to separate them in a group. To obtain smaller-sized cellulose, more cycles of treatments need to be repeated. These mechanical treatments require subsequent steps of chemical purifying processing to remove amorphous cellulose.

Acid hydrolysis focuses on removing amorphous regions of cellulose fibrils. Sulfuric acid is commonly used in this process, and it produces good suspension of cellulose particles [33]. After a period of time of acid reaction with cellulose, the solution is diluted by deionized water. Then the small-sized cellulose is separated by centrifugation and filtration. The residue of the acid is removed by rinsing with deionized water.

1.1.4 Types of Cellulose Fibers and Particles

According to the characteristics (size, crystallinity, aspect ratio, crystal structure) of the cellulose fibers, they can be categorized into different groups. In macro scale (larger than 10 microns), there are wood and plant fibers (WF, PF) and microcrystalline cellulose (MCC). The remaining types of cellulose are close to nano size. This group includes cellulose micro and nano fibrils (MFC and NFC), nanocrystalline cellulose (CNC), tunicate nanocrystalline cellulose (TCNC), algae cellulose particles (AC), and bacterial cellulose particles (BC). In this dissertation, MCC and CNC are used to produce composites samples.

WF and PF are the largest-sized fibers among all types of cellulose (typically larger than 2000 microns). These natural fibers have a variety of fiber lengths, which can be used according to different applications. The diameter of the fiber is from 20 to 50 microns. However, because of less treatment of the fibers, the crystallinity (43–65%) is lower than that of other types of cellulose particles[23].

MCC is produced by acid hydrolysis of wood and plant fibers. Due to the strong hydrogen bonding force, this cellulose is actually an aggregation formed by micro cellulose fibrils in various sizes. Therefore, the structure of MCC is typically a porous particle in diameter of 10 to 50 microns. It will potentially break up when compounded with other materials. In addition, it is reported that this cellulose has high crystallinity (80–85%) [34, 35].

MFC is obtained from highly purified wood and plant fibers. It contains a set of elementary cellulose fibrils grouped together in a certain crystal structure[36]. It has a high aspect ratio (0.5 to 10 microns in length and 10 to 100 nm in width). The crystallinity of MFC is normally from 51% to 69% [37].

NFC is produced by a specific refining approach in the mechanical treatment of wood and plant fiber [4]. It is commonly composed of 36 cellulose chains in a single fibril. The nano fibril is 4–20 nm in width and 0.5 to 2 microns in length, which is smaller than the dimensions of the micro-size fibril. In addition, the particle has a square-shaped cross-section. The crystallinity in this particle is nearly 100%, including both amorphous and crystalline regions [38, 39].

The CNC particle is derived through acid hydrolysis of WF, PF, MCC, MFC, and NFC. It has several other names: cellulose nanocrystals, cellulose nano whiskers, cellulose whiskers. The shape of CNC is normally like rods or whiskers 3–5 nm in width and 50–500 nm in length [40]. It has high crystallinity, from 54% to 88%. Studies show that the parameters of the acid hydrolysis process determine the properties of CNC. Inadequate acid hydrolysis results in elementary crystals and amorphous regions remaining in the particles. It changes the morphology of the CNC particles. Excessive acid hydrolysis can possibly depolymerize the crystalline region, which decreases the size of the particles [3]. Due to the small size of the CNC, the total surface area of the particle is larger than that of MCC or MFC of the same mass. The intermolecular force is proportional to the surface area. Therefore, CNC particles tend to agglomerate together into larger particles[3].

TCNC is derived from acid hydrolysis of tunicates. The morphology and mechanical properties of this particle are different from those of CNC. The shape of TCNC is like a ribbon with height, width, and length of about 8 nm, 20 nm, and 100 to 4000 nm, respectively. It has high crystallinity (85% to 100%) [3, 41]. Compared with CNC, TCNC has a larger aspect ratio (70–100) and a parallelogram-shaped cross-section.

AC is produced from the cellulose microfibrils of algae cell walls by mechanical treatments and acid hydrolysis. The aspect ratio of AC is more than 40. The length of the particle is normally larger than 1 micron. According to the species that produce the cellulose fibril, AC has square (20 nm in width, 20 nm in height) and rectangular (5 nm in width and 20 to 30 nm in height) shapes in the cross-section [42, 43].

BC is the cellulose microfibril produced from bacteria. Similar to the dimensions of AC, it has a larger aspect ratio (greater than 50) and is more than 1 micron in length. BC has a rectangular cross-section (6 to 10 nm in width, 30 to 50 nm in height) [44]. It has also been found that the crystal structure (the ratio of $I\alpha/I\beta$) can be changed by different culturing conditions [42].

1.1.5 Mechanical Properties of Cellulose Particles

The mechanical properties of the cellulose particles are essential to the application of these materials. However, the characterizing method is limited by the size of the particles. In addition, there are a variety of factors that affect the mechanical properties of certain types of cellulose, such as processing methods, chemical structures of the source material, and defects and flaws in the organisms during the growing period. This increases the difficulty of obtaining an accurate value of a certain mechanical property. Currently, most studies are focusing on the elastic properties of cellulose particles. The elastic properties of larger-sized fibers are normally characterized by tensile tests on specimens. For cellulose at micro and nano scale, there are several approaches that can obtain the properties indirectly. Raman spectroscopy is a technique that provides stress-strain information by the shifting of the characteristic Raman peak [45]. It has been applied to characterize a variety of materials, including cellulose [46-48]. Atomic force microscopy (AFM) indentation is another approach for measuring the elastic modulus of the fiber. The test is conducted by a rigid nano-sized probe contacting the substrate made of the testing material. The elastic modulus of the material can be calculated based on the displacement of the tip of the probe and the contacting force as the probe is scanning on the surface of the substrate[49]. For the mechanical properties of various cellulose crystal structures that have high crystallinity and are even smaller than CNC, X-ray diffraction and an inelastic X-ray scattering spectrometer can be used to characterize them [50, 51]. In addition, the mechanical properties of crystal structure can be estimated by models built in a computer [52, 53]. The following Table 1 summarizes the mechanical properties of cellulose particles in categories.

Table 1.1. Mechanical properties of cellulose materials

Material	E_a (GPa)	E_t (GPa)	σ_f (GPa)	ε_f (%)	Reference
WF	14-27	-	0.3-1.4	4-23	[54]
PF	5-45	-	0.3-0.8	1.3-8	[55-58]
MCC	21-29	-	-	-	[58]
MFC&NFC	N/A	-	-	-	N/A
CNC	57-105	18-50	-	-	[59, 60]

TCNC	124-180	-	-	-	[41, 61]
BC	61-114	-	-	-	[62, 63]
Cellulose Iα	128-155	5-8	-	-	[52, 64]
Cellulose Iβ	120-168	14-16	7.5-7.7	-	[50, 52, 65]
Cellulose II	9-90	-	0.2-1.0		[53, 57]

Note that: *Ea* is axial elastic modulus, *Et* is transverse elastic modulus, σ_f tensile strength, ε_f is failure strain

As shown in Table 1.1, the stiffness of CNC is significantly greater than that of larger-sized cellulose such as WF, PF, and MCC. The reason for this is considered to be that CNC has higher crystalline content compared with larger-sized particles and that the structured and dense crystalline is stiffer than the amorphous cellulose. This idea can also be applied to the case of TCNC. Due to higher crystallinity, higher content of Iβ crystal structure, and uniform morphology of the particle [15], TCNC is much stiffer than CNC. In the aspect of the crystal structure of cellulose, Iα and Iβ have approximately the same axial elastic modulus, but Iβ has a much higher transverse elastic modulus than that of Iα. It can be seen that both Iα and Iβ are stiffer than II and that Iβ presents greater tensile strength.

Table 1.2. Properties of common structure and reinforcement materials

Material	Elastic modulus (GPa)	Density (g/cm^3)	Reference
Aluminum	69	2.7	[66]
Steel	200	7.8	[66]
E-glass	72	2.5	[67]
Kevlar-49	124	1.4	[67]

MWCNT	270-950	-	[68]
CNC	57-180	1.5	[60]

Note that: MWCNT is multiwalled carbon nanotube

Table 1.2 shows the elastic modulus and density of several materials in comparison with CNC (including TCNC). It can be seen that the average elastic modulus of CNC is greater than that of aluminum and E-glass and approximately the same as Kevlar-49, but it is lower than that of steel and MWCNT. This shows that CNC has good stiffness as a reinforcement for common polymers. In addition, CNC presents lower density compared with metallic material and E glass, which suggests that the application of CNC can reduce the weight of a structure, with good mechanical performance.

1.1.6 Thermal Properties

As a bio-based reinforcement material, cellulose is compounded with polymers above the melting temperature of the matrix material. Therefore, it is important to investigate the thermal properties of cellulose. In this dissertation, the thermal chemical degradation and the coefficient of thermal expansion (CTE) will be discussed.

To characterize thermal chemical degradation, thermogravimetric analysis (TGA) is used to measure the weight loss of samples at the setting temperature. Normally, the degradation of cellulose begins at 200–300˚C, depending on heating temperature, heating rate, chemical structure, particle size, and surface modification [69-71]. In study [69], freeze dried MCC, CNC, and chemically modified CNC were tested by TGA. The tests showed that MCC starts to degrade at 300˚C. In contrast, the degradation temperature of CNC is about 260˚C. The chemically modified CNC particles present a shift of onset degradation temperature, either lower than 260˚C or higher than 300˚C. In another study [71], TGA was conducted on MCC from different sources (cotton sliver, jute felt, newsprint, filter paper). It was found that jute-made MCC had the lowest onset degradation temperature (250 ˚C) of all types of MCC, to which the higher content of hemi-cellulose contributed.

The CTE of crystalline cellulose in the axial direction was calculated as 0.1 ppm K-1 [72]. Compared to most of metallic material and ceramics [67], the value is much lower. However, it is about the same level as materials of high elastic modulus, for example, carbon fibers. In the aspect of larger-sized cellulose particles, the CTE of BC was measured as 2–3 ppm K-1 in [73]. Moreover, the CTE of NFC [70] and MFC [74] were found to be 2.7 ppm K-1 and 15–25 ppm K-1, respectively. It can be seen that the CTE increases with the particle size.

1.1.7 Modification of Cellulose

Containing a hydroxyl group, cellulose is a hydrophilic material that tends to form agglomeration by intramolecular hydrogen bonding, and the agglomeration gets severe when the particle size is small. In addition, the cellulose material can absorb moisture from the ambient air. The dissertation will study the effects of hydrogen bonding and agglomeration by microscopy and modeling in the following chapters. This prevents adhesion at the interface between the cellulose filler and the matrix in composites. The degradation of cellulose is another problem that commonly occurs during compounding with polymers. To overcome disadvantages such as poor dispersion and degradation and to enhance the adhesion between the cellulose and the matrix material, surface modification of cellulose is one of the most efficient approaches and has been widely applied in industry[75].

Silanization is one of the most common pretreatment techniques for cellulose surface modification. A silane coupling agent creates crosslinking intermolecular bonds at the interface of the filler and the matrix. It is found that the silane treatment is more suitable for alkaline-treated fibers, where there are more reactive sites for silane reaction than those of the untreated fibers. However, a silane coupling agent may reduce the hydroxyl groups in cellulose chains. When the coupling agent is applied, the hydrolyzable alkoxy groups will first transform into silanols in the presence of moisture. The hydroxyl groups in cellulose chains interact with silanols and form strong covalent bonds[76]. More detailed studies have been done to investigate the effect of silane coupling agents by applying a variety of silane solutions to different cellulose materials. Three aminopropyl trimethoxy sliane solutions were used for a flax fiber surface. 60% stiffness improvement was reported in the modified flax-reinforced epoxy composites [77]. Aminosilane solution-treated soaked sisal fiber was found to have a 23.6% tensile strength enhancement in epoxy-based composites compared to untreated sisal fiber [78]. It is shown in study [76] that removal of lignin from the surface of cellulose increases the absorption of silane coupling agent, while ploysiloxanes prevent the absorption.

Mercerization is another effective modification approach. In this process, cellulose fibers are soaked in an alkali solution at a certain temperature. The intramolecular hydrogen bonding of cellulose chains dissociates after a period of time, which breaks cellulose fibril into several groups of sub-fibrils. It dramatically increases the aspect ratio of cellulose fibers and the interfacial area of cellulose filler and matrix materials, but it also damages the network of hydrogen bonding and produces more amorphous cellulose. The study indicates that a rough surface topography was created after the modification that resulted in good cellulose/matrix adhesion [79]. In addition, mercerization increases the possible interacting spots in cellulose chains, which gives good fiber wetting in compounding. It is found that the degree of polymerization and the orientation of cellulose crystallites were altered due to the removal of lignin and hemicellulose in mercerization.

It significantly affected the stiffness and strength of the cellulose fiber [80]. A variety of studies have been done to optimize the effect of mercerization. In [81], a 10–30% sodium hydroxide solution was used for the mercerization of flax fibers. It was found that 5%, 10%, and 18% sodium hydroxide concentrations showed the best modification effects. Mercerization time is investigated in study [82]. Jute fibers were immersed in a 5% alkali solution for 8 hours at 30 ˚C. It showed that 2 hours is the best processing time due to the hemicellulose removal ceasing after 2 hours. Moreover, study [83] reported that 2% alkali solutions under conditions of 200 ˚C and 1.5 MPa pressure had good defibrillation effect on cellulose fibers.

Peroxide treatment is applied to cellulose fibers in particular for enhancing their mechanical properties. The free radicals decomposed from peroxide can easily react with the hydrogen groups of cellulose fibers and matrix material, and they then create the coating on the fiber surface. Benzoyl peroxide and dicumyl peroxide were applied to flax fiber in acetone solution in study [81], and alkali pretreatment was conducted prior to the use of peroxide.

Benzoylation treatment creates benzoyl groups in cellulose fiber and prevents the hydrophilic effect caused by hydrogen bonding. Benzoyl chloride is commonly used in this treatment. The detailed treatment process was investigated in several studies. In study [79], 18% NaOH solution was used in pretreatment of cellulose fibers for half an hour. Then 10% NaOH solution and 50 ml benzoyl chloride were applied to the treated fibers. A similar treatment process was done in [84], in which 15 min of benzoylation treatment was conducted on sisal fibers and the fibers were then soaked in ethanol for 1 hour after the treatment.

1.1.8 Application of Cellulose Materials

Cellulosic materials, including macro-sized natural fibers, micro- and nano-sized fibrils, and particles have advantages of good stiffness and tensile strength with low density. They are widely applied as filler materials in composites. This will be discussed in the cellulose-filled composites part later.

1.1.9 Challenge of Cellulose in Application

Even though great effort has been taken in the study of cellulose materials and they have already been applied in many fields, there are still challenges in aspects of the properties of cellulose and its production.

The hydroxyl groups in cellulose chains enable the cellulosic material to absorb moisture from the ambient environment. This hydrophilic nature of cellulose has been found in many studies [85-87]. However, it becomes a problem when the cellulosic materials are used as fillers in composites. A reduction has been found in flexural strength, modulus, and fracture toughness of cellulose fiber-reinforced epoxy composites after absorbing moisture for two week [88]. Similar effects are also shown in study [89]: the tensile strength of bacterial cellulose fiber-reinforced starch biocomposites in different fiber loadings decreased after 24 and 182 hours of moisture absorption. Study [90] reported that cellulose fiber swelled in absorbing moisture, which potentially generated micro cracks in the matrix material. This may eventually result in debonding between the cellulose fibers and the matrix. Another study [91] showed that the structure of amorphous cellulose became unstable in the presence of moisture, which can affect the mechanical and thermal properties of cellulose-reinforced composites. In addition, it is shown in study [92] that the interfacial distance of the cellulose filler and polyester resin matrix increased after successive moisture absorption and drying. It significantly affected the adhesion of the filler and the matrix material, resulting in debonding issues. This study also showed that the free volume [93], which is the small space such as gaps or pores existing between polymer chains, increased with moisture absorption. It is believed that this encourages the mobility of the cellulose and polymer chains that leads to a softening response of the composites. In some cases, researchers were able to overcome the problems caused by water absorption. A special modification of cellulose fibers was done in study [94] that made their surface hydrophobic. In study [95], nano-sized clay particles were used in cellulose fiber-reinforced vinyl-ester resin to absorb moisture. It effectively reduced the water absorption in the composites. Certain formulations of cellulose and polymer were found to have a decrease in water sensitivity. Study [96] showed that unmodified ramie cellulose-reinforced starch-based composites were insensitive to moisture.

Nano-sized cellulose with large surface area and hydroxyl groups tends to form agglomeration during compounding. The agglomeration in the composites may result in reduction of mechanical properties [97]. In study [98], cellulose and graphene nanocomposites were investigated by molecular dynamic simulation. A decrease of the in-plane elastic modulus is found in composites with agglomeration of the cellulose and graphene, compared with the case of a system with well-dispersed fillers. CNF-reinforced epoxy composites were studied by tensile tests and multi-scale FEA (finite element analysis) [99]; it was reported that both the aspect ratio of CNF and the elastic modulus of the composites decreased in the presence of agglomeration of CNF. Additionally, agglomeration can potentially increase the stress concentration in the composites. Even though very little research has been done about stress concentration with cellulose agglomeration, it was found in a study of carbon nanotube-reinforced composites that the agglomeration of the filler led to additional stress concentration [100]. This may result in the failure of the composite material at lower strain, compared with the well-dispersed carbon nanotube-reinforced composites. Moreover, the agglomeration of a variety of fillers was investigated in study [97]. It was found that adhesion between the fillers and the matrix materials decreased with the increased mass ratio of filler agglomerations. The tensile modulus shows the same trend as the adhesion properties.

The thermal degradation problem significantly affects the mechanical properties of cellulose and its application. As has been mentioned in the earlier discussion of the thermal properties of cellulose, cellulosic materials normally begin to degrade at 200–300˚C, which is about the same range as the melting temperature of most thermoplastics [101]. Therefore, degradation of cellulose is inevitable when it is compounded with thermoplastics or other materials at these temperatures. A dramatic decrease of stiffness in cotton fiber was found when the temperature was above 180 ˚C, while the stiffness remained constant below 180 ˚C [102]. A similar trend was found in study [103], in which the elastic modulus of different cellulosic materials decreased when the temperature increased to 230 to 250˚C. In addition, jute and flax fibers were tested in an oven over a range of temperatures in study [104]. It showed that jute fibers have higher thermal stability compared to flax fibers, which indicates that specific types of cellulose fiber can reduce the influence of degradation. However, both fibers showed a decrease of tenacities at 210 ˚C after 2 hours. It was also found that the alkali-treated flex fibers had greater tenacity compared with untreated ones at 210 ˚C. This suggests that the modification techniques used on cellulose material can provide an effective approach to deal with degradation issues of cellulose.

Modification treatments are effective approaches to alter the properties of cellulosic materials, but the cost of modification varies among different treatment chemicals and processes. Moreover, due to the high surface area of nano- and micro-sized cellulose particles, the cost of the treatments also increases. The cost of modified nano-sized cellulose may prevent the materials from reaching commercialization. Researchers need to develop new modification approaches to optimize the effect with comparatively lower costs. In aspects of the production of cellulose, cellulose with smaller size normally comes with complex processing techniques and a high price. However, in consideration of the potential better mechanical properties of nano-sized cellulose compared with the macro-sized, there is a difficulty in balancing the improvement of properties and the cost of nanocellulose applications.

Even though a lot of research has been done to characterize cellulose particles, the specific structures and mechanical properties of nano-sized particles are still challenges for researchers. Due to the limitation of the small size of nanocellulose, most of the properties, including the percentage of crystallinity, location of amorphous areas, the ratio of Iα/Iβ, and surface chemistry, are predicted by atomic models. Currently, the properties of nanocellulose and cellulose crystalline structure are obtained by AFM (atomic force microscopy) [49], Ramen [45], X-ray diffraction, and inelastic X-ray scattering spectrometer [50, 51], but it is difficult to compare the data of properties from different characterizing techniques. There is a need for standardized measurement with high sensitivity, which can provide specific data with small deviation. This will promote research and application of nanocellulosic materials.

1.2 Polyamides

As a member of the thermoplastics family, polyamides have been widely applied as structural plastics for decades. “Nylon” is another name broadly used for all types of polyamides. This material is famous for its good stiffness, strength, and toughness. In addition, it has resistance to oils, greases, lubricants, hydrocarbons, strong mineral acids, and oxidizing agents [105]. Polyamides are synthesized from monomers containing amide (-CONH-) groups. The majority of commercial polyamides are semicrystalline materials that make up almost 90% of global consumption. The other groups of polyamides contain amorphous regions such as ring-shaped structures. This type of polyamide is typically produced by a variety of monomers.

The principles of nylon synthesis were first published in the late 1920s [106]. The actual nylon (poly hexamethylene adipamide) was then produced in a DuPont laboratory in 1935. The properties of this type of nylon were also characterized. Based on this work, synthesis of nylon 6 was done from polycaprolactam in 1938, and the patent was issued in 1941 [105]. Different types of processing methods and polyamides have been studied and developed since then.

Bio-based polyamides, different from fossil-based ones, are derived from a variety of vegetable oils. Researchers started to study techniques to produce bio-based polyamides in the 1940s. For instance, polyamide 11 (PA 11) synthesized from castor oil was developed [107]. Although the bio-based polyamides are produced from different source materials, their properties are almost the same as the ones synthesized from petroleum. Due to concerns about the environmental problems and the demand for renewable resources, the production of bio-based polyamides keeps increasing. It reached a global capacity of 40000 tons in 2010, which is about 5% of the biopolymer market [108].

1.2.1 Types of Polyamides and Their Production Processes

According to their constituents, polyamides can be generally categorized into two groups: aliphatic and aromatic polyamides. The aliphatic polyamides family includes nylon 6, 11, 12, 46, 66, 610, 612, etc. Today nylon 6 and 66 account for nearly all polyamides production. Aromatic polyamides were developed later than the aliphatic groups. A glassy aromatic polymer poly(trimethylhexamethylene terephthalamide) was produced in the 1960s, and various other aromatic polyamides were made in the 1970s and 1980s [109]. This dissertation is focusing mainly on aliphatic polyamides. Bio-based PA610 and PA1010, which are used as matrix material for cellulose, belong to this group.

Different polyamides are named for the number of carbon atoms between the amide groups in the monomer. For example, PA 6 and PA 11 have 6 and 11 carbon atoms connected between ketone (-CO) and amine (-NH). Sometimes, there are multiple amide groups in a single monomer of polyamides, such as PA46. There are 4 carbon atoms between two amine groups and 6 carbon atoms between ketone groups. Note that carbon atoms in ketone groups are also included in the counting of carbon atoms.

For bio-based polyamides, PA 610, 1010, and 11 are the three commonly used ones that are mainly covered in this dissertation. There are also other types of bio-based polyamides, such as PA 42, 44, 46, 510, etc. These polyamides will not be discussed here.

PA610 is partially (63%) derived from bio sources, while PA11 and 1010 are fully based on bio sources [108]. Synthesis starts from castor oil, consisting of ricinoleic acid. After steps of pyrolysis, bromination, and ammonia treatment, ricinoleic acid transforms into 11-aminoundecanoic acid, which is a crystalline solid. It is then used to produce PA11 by a polycondensation process. PA610 and PA1010 can be also be derived from ricinoleic acid. Alkali fission is applied to convert ricinoleic acid to sebacic acid. Hexamethylene diamine (HMDA) and decamethylene diamine (DMDA) can be produced from sebacic acid, and PA610 and PA1010 are obtained finally from polycondensation of HMDA and DMDA, respectively. More details of the synthesis process can be found in study [108].

1.2.2 Properties

Polyamides are widely used because of their good stiffness and tensile strength. These properties of common polyamides are summarized in Table 3.

Table 1.3. Mechanical properties of common polyamides

Material	Elastic modulus (GPa)	Tensile strength	Failure strain (%)
PA 46	3	100	30
PA 6	2.8	81	100-200
PA 66	2.83-3	83	60
PA 610	2.1	55	100-150
PA 1010	1.278	51	-
PA 11	1.17-1.4	57	120
PA 12	1.41	49	250

The data above is obtained from [105, 109, 110]

The structures of all types of polyamides contain amide groups (-CONH-); this functional group forms inter-chains hydrogen bonding that has a significant effect on the properties of polyamides. The ratio of hydrogen bonding formed by amide groups to CH_2 groups in the backbone chains accounts for the hydrogen bonding density of polyamides. Generally, the crystallinity of polyamides is proportional to this hydrogen bonding density, and the crystallinity is directly related to multiple characteristics of the material, such as stiffness, melting temperature, etc.

It can be seen in Table 1.3 that the elastic modulus and the tensile strength of the series of polyamides decreases from 3 GPa in PA46 to 1.41 GPa in PA12, which corresponds with the decreasing trend of hydrogen bonding density. In contrast, the failure strain increases with the reduction of elastic modulus. However, there are exceptions regarding the odd or even numbers of CH2 groups in the polymer chains when the hydrogen bonding densities are approximately equal. In the case of PA 6 and PA 66, the odd number of CH2 groups between amide groups in PA 6 requires inverting the entire adjacent polymer chains to form intermolecular hydrogen bonding, but just a segment lateral movement is needed to form intermolecular hydrogen bonding in the case of an even number of CH2 groups between amide groups in PA 66. The greater difficulty in forming hydrogen bonding in PA 6 than in PA 66 is believed to result in lower crystallinity [105]. It can be proved that PA 66 has slightly higher stiffness and tensile strength.

Polyamides tend to absorb moisture from the ambient environment. Water molecules are attracted by amide groups in polymer chains, which prevents the formation of intermolecular hydrogen bonding. The crystallinity of polyamides decreases with the reduction of hydrogen bonding. Thus, the mechanical properties are significantly affected. Table 1.4 shows the properties changes before and after absorption of moisture.

Table 1.4. Properties of common polyamides after moisture absorption

Material	E (GPa)		σ_f (GPa)		ε_f (%)		T_g (°C)	
	Dry	Wet	Dry	Wet	Dry	Wet	Dry	Wet
PA 46	3	-	100	-	30	-	-	-
PA 6	2.8	0.97	81	69	100-200	300	41	3
PA 66	2.83-3	1.21	83	77	60	≥ 300	48	15
PA 610	2.1	-	55	-	100-150	-	42	10
PA 1010	1.278	-	51	-	-	-	-	-
PA 11	1.17-1.4	1.03	57	54	120	300	43	-
PA 12	1.41	1.03	49	47	250	250	42	-

Note that: E is elastic modulus, σ_f is tensile strength, ε_f is failure strain, T_g is glass transition temperature. The wet condition is 50% relative humidity. The data are obtained from [105, 109, 110].

It can be seen that the tensile strength and elastic modulus of PA 6, 66, 11, and 12 decrease after moisture absorption. The involved water molecule weakens the intermolecular bond and increases the free volume in the material [111]. Therefore, it is believed that the mobility of the polymer chains increases because of these changes, which results in failure strain increase and softening of the material. Moreover, the moisture in polyamides stiffens the material at low temperature. It is reported that the brittleness temperature of PA 66 in dry and wet conditions is -80 ˚C and -65 ˚C, respectively [105].

Glass transition is defined as a reversible process in which the polymer transforms from the glassy state to the rubbery state when the temperature increases [112]. The glass transition temperature is measured at the moment the state changes. Even though the mechanism of glass transition is not completely clear, it has been found in studies that polyamides with fewer amide groups show lower glass transition temperature and a smaller change in it in the presence of moisture [113, 114].

Thermal properties are important in manufacturing polyamides-based composites. The common thermal properties (besides glass transition temperature) of polyamides are summarized in Table 1.5.

Table 1.5. Thermal properties of common polyamides

Material	PA46	PA6	PA66	PA610	PA1010	PA11	PA12
Melting point	295	215	264	215	202	185	175
Deflection temperature	150–170	60	75	55	-	55	51

Coefficient of linear expansion	9.2	9.5	10	15	-	15	12

Note that: the unit of melting point and deflection temperature is ˚C. The load for deflection is 264 lbf/in^2. The unit of coefficient of linear expansion is 10^{-5} ˚C^{-1}. The data are obtained from [109, 115].

As shown in Table 1.5, PA 46 has highest melting temperature among all the types of listed polyamides, and there is a trend of decreasing melting and deflection temperature from PA 46 to PA 12. In the case of PA 46, it is believed that its high hydrogen bonding density leads to a high level of crystallinity. It requires greater energy input to break the bonding of the crystalline structure, which results in a higher melting temperature compared with other polyamides. In addition, the stiffness is enhanced with the increase of crystallinity. Deflection temperature is defined as the minimum temperature required to bend the testing specimen to 0.25 mm with the set load. It required higher temperature to soften the polyamides of greater stiffness.

In summary, PA 46 has the highest stiffness, crystallinity, and melting temperature of the common commercial nylons, but its high amide-to-methylene ratio gives a high tendency for moisture absorption. PA 6, with a moderate amide-to-methylene ratio (1:5), has good stiffness. However, the odd number of methylene groups between amide groups leads to more amorphous polyamides and lower melting temperature compared with PA 66 and PA 46. This can be beneficial in the polymer manufacturing and in processing with other materials, but it also makes the polymer more sensitive to moisture and additives. PA 66 has good tensile strength, stiffness, and creep resistance and great gas barrier properties, which make it a widely applied structural material in industry. PA 610 and PA1010 can be partially or fully derived from bio-based source material. They have balanced mechanical properties in common with other polyamides. Even though their stiffness and strength are lower than PA 46, 6, and 66, they have lower processing temperature and good creep resistance and barrier properties. PA 11 and 12 have low amide-to-methylene group ratios. At a cost of lower stiffness and strength compared with other polyamides, they show good dimensional stability, low-temperature toughness, low moisture absorption, and crack resistance [105]. Low melting temperature is suitable for compounding with the fillers that have low heat resistance.

1.2.3 Applications

Polyamides, with excellent stiffness and strength, high thermal resistance, and great abrasion resistance, have a variety of applications that are summarized in the following paragraphs.

Automotive parts are one of the largest nylon markets [116, 117]. Depending on the use of the parts, processing additives and reinforcing fillers are applied in production. With high melting temperature, nylon is a suitable material for the parts under the hood, such as the engine cover, fuse box housing, etc., and the addition of high-performance mineral or glass to nylon makes it even tougher. Reinforced nylon is found to be an ideal material, as automotive manufacturers are seeking light-weighted materials for the engine compartment. Other than the applications under the hood, reinforced nylon is also used in steering wheels, clutch pedals, wheel rims, fender extensions, and mirror housings. In aspects of its chemical resistance to various automotive fluids, nylon is also used to produce brake fluid reservoirs, power steering reservoirs, air intake manifolds, and radiator end tanks [105].

Nylon is also widely applied in the electrical and electronic fields. Its flame-retardant ability is the most important feature compared with other characteristics of plastic materials. It is found that nylon requires more heat absorption (characterized by heat release rate and effective heat of combustion) to reach the fire point, compared with most common polymers [118]. Nylon products include plugs, connectors, terminal blocks, and antenna mounts. In addition, some of the polyamides showing lower stiffness and good abrasion resistance are suitable for making wire and cable coatings.

Other nylon applications are miscellaneous, such as consumer products (toys, fishing line, ski boots, power tools, housing, handles, brushes, packaging material, kitchen equipment, etc.) [105]. These products take advantage of the good tensile and impact strength and abrasion, heat, and chemical resistance of nylon material.

1.3 Cellulose Composites

Due to its good tensile strength and stiffness, renewable features, and low density, cellulosic material has been extensively studied and widely used as reinforcement in composites [15, 29, 119, 120]. The processing techniques and the properties of cellulose-reinforced matrix composites are discussed in the following subsections.

1.3.1 Processing Techniques

Generally, there are two different composite design perspectives using different processing methods. One direction of research is focusing on producing composites by maximizing the effects of the interaction between cellulose fillers and matrix materials. This requires processing techniques to improve the dispersion of the fillers, which results in a reduction of the agglomeration and an increase of the interfacial area of the fillers. Another route of study undertakes efforts on creating a network of cellulose filler in the composites. This approach requires modification of cellulose and polymer materials to maximize the reinforcement. There are four processing techniques for cellulose-reinforced composites that are introduced here.

The melt-compounding process is one of the most commonly used techniques for cellulose-reinforced composites [29, 33, 55]. The cellulosic fillers and matrix polymers are mixed in a piece of equipment called an extruder. The materials are sufficiently compounded by the rotation of the screws in the extruder, and this process is conducted at a temperature above the melting points of the fillers and the matrix under a certain pressure. This process is suitable for low concentrations of cellulose particles (less than 30 mass ratio of the whole composites), because a high content of cellulose normally introduces great shearing force, which results in congestion in the extruder. Degradation of the cellulose may occur during this process [121]. Thus, it requires careful control of temperature and the rate of screw rotation to reduce the degradation. Research focusing on the dispersion issue of cellulose during this process can be found in [122, 123].

Solution casting is another approach for making cellulose-reinforced composites. Initially, the cellulose particles are dispersed in a medium such as water. In different cases, various organic mediums can also be applied. Then the dispersion of cellulose is mixed with the desired polymer solutions. Compared with the melt-compounding process, the range of compositions (mass ratio of cellulose and matrix materials) can be designed from 0 to 100 % by controlling the weight of the cellulose and matrix added into the mixture [124, 125]. The composite is then produced from the mixture of cellulose and polymer, in general by two different techniques. The first one is casting the mixture on a surface. Evaporation, freeze-drying, and compression molding are then applied to the mixture to produce the composites, or the mixture is freeze-dried followed by extruding and compression molding. To achieve good dispersion of cellulose particles, a variety of modifications of this technique have been developed

[29]. It is found in study [126] that a network of cellulose is formed when the solution casting process is performed.

Electrospinning is a process that produces fiber-shaped composites. Similar to the first step of solution casting, the dispersed cellulose particles are mixed with polymer in a solution in preparation. The mixture is then melted and ejected through a small nozzle, where a high voltage is applied between the nozzle and a conductive plate [127]. The ejected compounded composite then cools down on the plate for further treatments. This process produces composite fibers at micro or nano scale. A wide range of cellulose compositions can be achieved by controlling the weight ratio of cellulose and polymer in the mixture. There are several studies on improving the strength of the composite fiber by aligning more cellulose particles along the axial direction of the fiber [127-129]. The effects of the interfacial properties on the mechanical properties of the composite fiber are also studied in [127, 129].

Partial dissolution is a process that compounds cellulose particles with a regenerated cellulose (cellulose II) polymer. A film made of cellulose particles is activated and partially dissolved in a solution of N-dimethylacetamide (DMAc) and lithium chloride/DMAc for a certain period of time. After removal of DMAc by rinsing the film, Cellulose II is then applied to the film by precipitation. This film is finally dried and molded at a certain pressure and temperature [130].

In this dissertation, the melt-compounding process is applied to produce cellulose composites. The details of the procedures are covered in the specimen preparation section.

1.3.2 Properties of Cellulose Composites

This part focuses on the mechanical properties of cellulose composites. The damping properties will be discussed in the damping section later.

Cellulose particles have been used as reinforcement in a number of polymer materials, and the properties, especially the mechanical properties, of the composites have been characterized in many studies [15, 29, 79] for composites with cellulose particles or fibers in macro scale (WF and PF). In study [131], unidirectional laminated composites were made from flax fibers and polypropylene (PP). It was found that the axial elastic modulus of the composites increased about 5%. In contrast, the tensile strength had a significant increase (27.5%). However, the elastic modulus and tensile strength in the transverse direction decreased at the same time. A similar trend can be found in study [132]. Unidirectional flax fiber-reinforced epoxy composites were produced in a range of filler mass ratio from 30% to 50%. It was reported that the longitudinal tensile strength dramatically improved by about 400% at a 50% filler mass ratio. More studies of unidirectional macro-sized cellulose fiber reinforced composites are provided here: jute fiber/PP [133], sisal fiber/epoxy [134], flax fiber/starch [135], and kenaf fiber/polylactic acid (PLA) [136]. It can be seen in these studies that cellulose fibers generally improve the stiffness and elastic modulus in the longitudinal direction. In addition, the reinforcement effects depend on specific matrix materials and modification methods of cellulose fibers. In aspects of isotropic WF- and PF-reinforced composites, multiple matrix materials, including PLA, poly(3-hydroxylbutyrat) (PHB), and poly(butylene adipate-co-terephtalate) (PBAT), were used to compound with flax fibers in study [137]. It was reported that the tensile strength of PLA, PHB, and PBAT improved approximately 47%, 100%, and 200%, respectively. Moreover, an increase in elastic modulus of more than 160% was found in all three types of matrix materials. It can be seen from the results that the reinforcing effect of the flax fibers was more pronounced in soft matrix materials. In another study, banana fiber in various lengths and filler loadings was added into polyester [138]. The results showed that the fibers at 30 mm showed the best improvement of elastic modulus and tensile strength in the composites. It is believed that there are not enough contacting surfaces between short fibers (less than 30 mm) and the matrix that transfer the stress from the matrix to the fiber under tensile loading. For fibers longer than 30 mm, the stress transfer was not effective due to the bending and entanglement of fibers, which led to a reduction of elastic modulus and tensile strength. In addition, the stiffness and strength increased with the addition of fibers up to 40% mass ratio, but these mechanical properties began decreasing when the fiber loading was greater than 40%. SEM results showed that there were more voids formed on the fracture surfaces with 50% fiber loading compared to that of 40%. This indicated that there were dispersion issues in the composites with high fiber loading that resulted in stress concentration and cracks. However, it was shown in study [139] that a decrease of tensile strength of PP was found with addition of wood fibers. The researcher proved that the poor adhesion between the filler and matrix material led to the reduction of the strength. This indicates that surface modification of cellulose fibers is required to achieve a good reinforcement effect. Researchers produced wood fiber-reinforced polyethylene with or without a silane coupling agent [140]. It is reported that the composites with the treatment of silane coupling agent showed higher stiffness compared to that of the untreated ones. It was believed that the dispersion of the fibers improved after the addition of the coupling agent. More studies about the isotropic modified WF-reinforced composites are provided [141-144]. All of these studies showed that modified wood fibers improved the mechanical properties of the polymers.

As cellulose processing techniques advance, micro- and nano-sized cellulose fibers (MCC, MFC, NFC, CNC) are currently attracting more attention in composites production. Limited by the small size of the fibers, unidirectional composites are rarely made in this case. Therefore, the studies shown below focus on isotropic or laminated composites. MCC particles derived from PF and WF are generally smaller than PF and WF and larger than MFC, NFC, and CNC. However, the reinforcement effects of MCC in various polymers are reported differently in various studies. MCC was added into a hydroxypropylcellulose (HPC) matrix in study [145]. It was found that the tensile strength and elastic modulus increased about two and three times after reinforcement by 20% mass ratio of MCC. Additionally, these mechanical properties got further improvement after application of a surface treatment agent (1,4-butyldiisocyanate). In another study [146], MCC and polyurethane (PU) composites were made and characterized. The highest tensile strength was reported as 257 MPa at 5% mass ratio of the filler This was much higher than that of pure PU samples, which was 39 MPa. In addition, a significant increase of failure strain (49%) and elastic modulus (163%) was also found. It was believed that the hydrophilic nature of MCC and PU enhanced the adhesion bonding between the fillers and the matrix, which helped the dispersion of the MCC particles and stress transfer in the composites under loading. Therefore, the mechanical properties were dramatically improved in this composite formulation.

However, several other studies showed negligible improvement or even lower mechanical properties of polymers with the addition of MCC. In study[147], MCC-reinforced PP composites were prepared at various filler loadings (2%, 5%, 10%, 15%). The results showed that there was less than 3% tensile strength improvement at 5% MCC loading, compared to that of neat PP. When the filler loading was more than 5%, MCC started to show negative effects on the tensile strength of PP. It was believed that the agglomeration formed by MCC was the cause of the strength reduction. A similar trend can be found in study [148], in which MCC was compounded with PLA by extruding and injection molding. A decrease of tensile strength and failure strain of the composites at 25% filler loading was reported, compared to neat PLA.

However, the elastic modulus improved 39% in this case. In contrast with WF- and wood pulp-reinforced PLA, MCC/PLA composites had the lowest tensile strength and elastic modulus. The poor adhesion between the filler and the matrix and the low aspect ratio of the filler were believed to be the main causes of the poor mechanical properties of MCC/PLA.

MFC and NFC are the cellulose fibrils with high aspect ratios, which are suitable for stiffening polymers. NFC is normally thinner and shorter than MFC. Here, this introduction is mainly focusing on MFC-reinforced composites because very few studies are available on NFC-reinforced composites. MFC/PLA composites were prepared and studied in [149]. It was reported that the composites had an increase of approximately 40% and 25% in elastic modulus and tensile strength with unaffected yield strain at 10% mass ratio of MFC. In another study [150] of MFC-reinforced PLA composites, 5% MFC showed a 30% increase of stiffness, negligible enhancement of tensile strength, and a decrease of failure strain compared to neat PLA samples. The effect of MCF on polyvinyl alcohol (PVA) was studied in [151]. A significant increase of stiffness is found at 5% filler loading compared to that of the control matrix. However, the enhancement of MCF was compromised at filler loadings higher than 5% due to the increase in entanglement of MCF. MCC/PVA composites were also prepared by the researchers at the same time. The results showed MCF had better improvement on stiffness of PVA polymers in comparison with MCC.

CNC with high crystallinity and specific aspect ratios has been used as reinforcement in composites. CNC-reinforced polyacrylamide (PAM) was made in a range of filler loadings (4.6%–50.3% mass ratio) in [152]. The mechanical test results showed approximately 134% and 24% increases of elastic modulus and tensile strength at 40.1% filler loading. Due to the melting temperature of PAM being much lower than that of CNC, the degradation of CNC during the compounding was mitigated, which was believed to be the main reason for the good stiffness and strength enhancement. However, the optimal fiber loading for the failure strain of the composites is 4.6%. This indicates that defects can be introduced into the composites with the addition of CNC. Researchers made treated and untreated CNC-reinforced poly (-ethylene-co-acrylic acid) (EAA) composites with three filler loadings (0.1%, 1%, 10% mass ratio) in [153]. It was interesting to find that the elastic modulus of EAA decreased about 16% with the addition of 0.1% untreated CNC, but a significant increase (9.6% and 186%) of elastic modulus was reported in 1% and 10% untreated CNC-reinforced EAA compared to neat EAA samples. In addition, a great reduction of the failure strain (from 255% to 6 %) was noticed in EAA after addition of 10% untreated CNC. The results indicated that the improvement of stiffness was achieved at the cost of a decrease of failure strain in untreated CNC-filled EAA composites. It was also reported that N,N-diallyl-3-hydroxyazetidinium-treated CNC had less stiffening effect on EAA but higher failure strain compared to the untreated CNC. In study [154], 5%, 10%, 15% mass ratio CNC-reinforced PLA composites were prepared and characterized. Tensile testing results showed an increasing trend of elastic modulus as the CNC loading increased from 5% to 15%. The highest improvement of elastic modulus was 3.8 GPa, which improved 8.5% over pure PLA samples. However, the tensile strength reduced from 65 MPa to 45 Mpa when 15% CNC was added. In contrast, a different reinforcing effect was reported in study [155]. CNC was added into polyvinylpyrrolidone (PVP) in a filler loading from 4.4% to 39.9% based on mass ratio. It was reported that there were maximum improvements of both elastic modulus and tensile strength at the same filler loading (29.2%). This indicated that the mechanical properties enhancement from CNC were significantly influenced by the types of polymers used in compounding. The degradation issue of CNC significantly affects the mechanical properties of

CNC-filled composites. Researchers made CNC-reinforced PP composites using two processing temperatures (175 ˚C and 210 ˚C) in [156]. It was reported that CNC enhanced of the stiffness of PP by 39% at maximum. Compared with the samples processed at higher temperature (210 ˚C), the samples made at 175 ˚C showed greater stiffness. This indicates that the degradation of CNC reduced its stiffening effect in the composites. The results also showed that the tensile strength is negligibly affected by addition of CNC. In aspects of failure strain, it was lower than neat PP in both cases of processing temperature and decreased with higher CNC content. However, it was interesting to find that the failure strain increased in the composites at higher processing temperature. This indicates that there were complex mechanisms other than degradation of CNC contributing to the failure strain of the CNC/PP composite system. More studies of CNC-filled composites (CNC/Poly(butylene succinate-co-butylene adipate, CNC/poly(butylene adipate-co-terephthalate, and CNC/PU) can be found here [157-159].

The mechanical properties of various CNC-filled composites have been introduced. Because this dissertation is based on work on various-sized cellulose-reinforced bio-based polyamides, an introduction to cellulose-reinforced polyamides is provided here specifically. However, only a few studies have been done on polyamides reinforced with CNC or larger-sized cellulose particles. Custom-made cellulose fiber-reinforced bio-based polyamides (PA 610 and PA 1010) were made in study [160]. The cellulose fibers used in the composites had great aspect ratios (several millimeters in length and 12 microns in diameter). The researchers studied the effects of filler loading and processing methods on the mechanical properties of the composites. An increasing trend of stiffness and tensile strength was found in both PA 610-based and PA 1010-based composites after the addition of more cellulose fibers (up to 30% mass ratio). A special processing method was proposed for producing unidirectional composites. These good improvements were believed to be obtained from the unidirectional distribution of cellulose fibers with a high aspect ratio. Similar improvement of mechanical properties was also found in study [161]. Special-made cellulose fibers in a size between WF and MCF were added to dimer fatty acid-based polyamides (DAPA). The test results showed a good stiffening effect of cellulose fibers at filler content up to 20%. In addition, the optimal filler loading for improving tensile strength is 15%, but the failure strain decreased with the addition of cellulose fibers. A research group published a study on three types of cellulose particles (MCC, CNF, and CNC)-reinforced PA 6 [162]. Three filler loadings (2.5%, 5%, and 10% mass ratio) were used for different formulations of the composites. The specimens were manufactured by thermal compounding with the addition of 3% processing aid. It can be found in the test results that MCC-reinforced PA 6 had the highest elastic modulus increase of about 28.3% at 10% filler loading compared to that of neat PA 6. CNC, the smallest among these three cellulose fillers, showed the lowest stiffening effect. Minor improvement of flexural modulus, flexural strength, and tensile strength was found in all three sizes of cellulose-reinforced PA 6. In addition, reduction of the impact strength of all composites was reported. With the increase of cellulose content, the impact strength decreased, and CNF showed the highest impact strength of the three cellulose sizes. It can be seen that the mechanical properties improvement from cellulose materials in PA 6 is limited due to the high stiffness of polyamides in nature. Moreover, the high processing temperature of PA 6 (close to the degradation temperature of cellulose) may also affect the properties of the composites.

1.3.3 Nano Mechanisms of Cellulose-filled Composites

Nano-sized fillers are found to have remarkable effects on a variety of features of composites, compared with conventional filler materials. In study [163], silica in micro and nano sizes was used to enhance the mechanical properties of epoxy polymers. It was found that nanosilica provided greater improvement in fracture toughness compared with that of microsilica filler. In another study [164], researchers investigated the effect of filler size by producing and characterizing spherical alumina particles of various sizes in reinforced vinyl ester resin. The tensile test results showed that nanoalumina particles-filled composites had the highest stiffness and tensile strength compared to micro-sized alumina-reinforced composites. It was also reported that nano-sized TiO2 particles gave great improvement on the failure strain of epoxy resin [165]. All of the studies above indicate that nano-size fillers provide special features in composites reinforcement. Therefore, CNC with an average size in the nano scale has already attracted the attention of researchers.

There are two principal methodologies accounting for the mechanisms at different length scales. Continuum mechanics is valid from macro (10^{1}) to micro (10^{-6}) scale. FEA [166] is a common method for predicting the stress and strain in materials. However, when the length scale decreases to nano (10^{-8}-10^{-9}) and pico (10^{-10}-10^{-12}) scale, the discrete structure of the molecules becomes more obvious and starts to influence the properties of the material. In this case, the classical continuum mechanics is no longer valid. Molecular dynamics [167] and quantum mechanics [168] are developed to account for the phenomena at nano and pico scales. In a common composite system, the interaction at the interface between the fillers and the matrix material is mainly associated with the properties of the intermolecular bonding. Nano-scale fillers have a larger contact surface compared with larger-sized fillers. Therefore, the interfacial interaction is believed to significantly affect the properties of the nanocomposites, and molecular dynamics can be applied to study the interaction. In addition, due to the molecular bonding forces existing at the interfacial area, the mechanical and dynamic properties of the materials at the interface are different from the rest of them. These materials are then proposed as an "interphase" to study the nano effects of the fillers. The interphase was found to be strongly dependent on its thickness and temperature [169].

Interphases have been modeled and applied in a variety of nanocomposites studies. The interphase was characterized in single-walled carbon nanotube (SCNT)-reinforced PVA [170]. It was reported that the interphase region was the key component for the stress transfer between SCNT and PVA, which resulted in remarkable improvement of the stiffness and strength in the composites. In study [171], the interphase called the nanocarbon structure was modeled between carbon fibers and epoxy matrix. The simulation results showed that the incorporation of interphase significantly improved the fracture toughness of the composites. Researchers built a model of nanocomposites with reinforced and weak interphases in study [172]. The characteristics of the interphase, including the volume fraction, thickness, moduli, and Poisson ratio were carefully studied. It was reported that the volume fractions of both reinforced and weak interphases are associated with the geometry and volume fraction of the nanofillers.

When the size of the filler decreases to nano scale, the diameter of the particle becomes similar to the length scale of the gyration radius of a common polymer chain. The moments of inertia of the particle and the chain are comparable. The dynamics of the chain is significantly influenced by the filler and vice versa [173-175]. It was shown in the study that the distance between the particles was reduced to below 2 gyration radii of polymer chains by the addition of nanoparticles at 2% volume fraction [176]. In another study [177], researchers found that nearly all the polymer chains were contacting with a surface area that could be assumed to be the surface of the fillers. The segmental mobility of the chains was reduced at a temperature above the glass transition point. It was also believed that a great number of entanglements of the chains could be immobilized by the nanosized fillers [178].

CNC with hydroxyl groups on its chemical structure can form hydrogen bonding with hydrophilic polymers. Unlike nonbonded forces such as the Van der Waals force existing in common composites, hydrogen bonding is much stronger, which potentially has great effect on the interaction between the filler and the matrix material. More details will be covered in the following modeling part.

1.4 Damping

Damping is a property that characterizes the energy dissipation capability during the dynamic response of materials. Materials with good damping have wide application in noise and vibration control and shock absorption in the automotive and aerospace industries [179, 180]. Among all the damping materials, fiber-reinforced composites have been extensively studied for decades [181-183]. This introduction focuses on the damping characterizing methods and damping mechanisms of common fiber reinforced and cellulose filled composites.

1.4.1 Methods for Characterizing Damping

Free vibration testing is one of the most common methods for characterizing the damping properties of materials. Before testing, the material is normally produced into beam-shaped samples. The sample is clamped horizontally at one end. The testing begins with exciting the vibration of the cantilevered sample. The response of the beam is captured by displacement, or other, sensors, which can be used to obtain the damping ratio (a dimensionless term characterizing the energy dissipation ability of the material) by the decay of the oscillation after the excitation. There are a variety of studies reporting the damping properties of composites through free vibration testing [184-187]. More details of this method are introduced in the damping test method for cellulose-reinforced PA610 composites.

Dynamic mechanical analysis (DMA) is another approach to study the damping properties and the glass transition temperature of materials [188]. A sinusoidal wave of stress is applied to the samples. The viscosity of the material is reflected by the phase lag between the applied stress and the resulting strain. DMA provides a material's complex modulus, consisting of the storage modulus and the loss modulus. The storage modulus accounts for the ability of the material to store and return energy, and the loss modulus shows the tendency of the material to lose energy. The ratio between the loss modulus and the storage modulus, which is called the loss tangent (tan δ), reveals the damping properties of the material. The dynamic properties of a variety of composite materials are studied using DMA in [189-193].

1.4.2 Damping Mechanisms in Composites

Even though damping materials have been applied for decades, the mechanisms of the damping sources still have not been fully investigated. Especially for the damping properties of composites, energy may be dissipated due to the characteristics of the matrix materials and fillers or mechanisms at the interface between the fillers and the matrix.

The viscoelastic nature of the matrix material is the most common source of energy dissipation in composites. It is believed that the viscoelasticity arises from the relaxation and recovery after the deformation of macromolecular polymer chains [194]. In study [195], researchers proposed a model based on the dynamics of the polymer chain clusters to investigate the viscoelasticity of polymers. It showed that the interacting behaviors of clusters with the matrix is dominated by the time scale of the structural relaxation of the clusters. It was reported that the shear modulus of the rigid phase formed at the interfacial layers of polymer clusters increased with the increasing of the volume fraction of the clusters. Many testing results of composites showed the effect of viscoelastic properties of matrix materials on enhancing damping properties. Glass fiber-reinforced epoxy composites were prepared in study [196]. It was reported that the damping of the composites dramatically increased as the volume fraction of the matrix material increased, and the damping improvement diminished at 60% of matrix volume fraction. Similar trends can also be found in studies [197, 198]. However, it is noted that the stiffness and strength of the composites decreases with the increasing volume of matrix material. In the aspect of the damping nature of fillers, their stiffness is normally much higher than that of the matrix materials. Therefore, the damping contribution of the fibers is minor due to the small deformation under loading compared to the matrix materials.

In addition to the viscoelasticity of the matrix materials, introducing fibers can improve the damping properties of composites compared to the pure matrix materials. Extensive studies have been done so far on the damping properties of fiber-reinforced composites. In aspects of synthetic fillers, Kevlar fibers, found to have higher damping capacity than glass fibers [199], were used as the filler in epoxy-based composites [200]. It was shown that high damping characteristics were achieved with the addition of Kevlar fiber to epoxy resin. Moreover, the results indicated that the damping improvement is independent of the elastic modulus of the composites in the range of 6–70 GPa. In addition, it was reported in several studies that carbon nanotube improved the damping of epoxy resin [201, 202]. The viscoelastic behaviors or the energy dissipation capacities of other synthetic fiber-reinforced composites, such as basalt fiber-reinforced PP [203], PVA fiber-reinforced concrete [204], and aramid fiber-reinforced epoxy [205] were also studied.

Besides synthetic fibers, the damping properties of cellulosic fiber- and particle-reinforced composites have obtained increasing popularity. Many damping studies were conducted on cellulose-filled composites, including banana fiber-reinforced polyester[206], hemp and flax fiber-reinforced PP [207], flax fiber-reinforced epoxy [208], short coir fiber-reinforced natural rubber [209], kenaf/hemp/flax fiber-reinforced PLA hybrid composites [210], and MCC-reinforced PA6 [189]. In study [184], it was found that the damping ratio of PP composites improved by 164% with the addition of 30% weight percent of hemp fibers, compared to neat PP. A similar trend was also reported in short banana and sisal fibers-reinforced polyester composites. For smaller-sized cellulose, an approximately 33% of loss tangent increase was obtained when adding 2.5% weight percent of MCC in PA 6 at 20 ˚C. However, the peak value of the loss tangent decreased with the addition of MCC.

Multiple mechanisms may account for the damping improvement in the presence of fillers in the matrix materials. The interphase [211] is a factor altering the damping of composites. The interphase is the region adjacent to the surface of the filler. Because of the discontinuity of the material chemical structure from the matrix to the filler in composites, the properties of the interphase are different from those of the filler and the matrix, and the thickness and the mechanical properties of the interphase depend on the specific combination of filler and matrix materials. DMA was conducted on carbon fiber-reinforced epoxy composites [212], and it was reported that the nature of the interphase (strong, ideal, or weak) influenced the mechanical and damping properties of the composites. The modeling work on interphase related to the damping of composites will be discussed in the modeling section later.

Permanent damages occurring between filler and matrix materials, such as crack formation, delamination, and fracture of fibers, dissipate the energy as heat from the system, which can be viewed as another damping mechanism existing in composites. However, the damage process is irreversible such that it is not commonly characterized by free vibration tests and DMA. Several studies have shown the energy dissipation from the internal damage of composites. In one study, impact tests were conducted on glass fiber-reinforced unsaturated polyester resin. The results revealed that the detachment of the fiber from the matrix contributed to the good energy dissipation [213]. The energy dissipation characteristics of polyethylene fiber-reinforced engineered cementitious composites were studied in [214]. It was found that the micro cracks obviously increased with the increase of fiber volume fraction. Moreover, the introduction of polyethylene fiber improved the strength of the composites, resulting in higher packing density in the matrix. It mitigated crack initiation and increased the fracture energy. In aspects of delamination, a study of unidirectional glass/carbon hybrid composites was conducted in [215]. The results showed that the energy dissipation from delamination depended on the volume of the layers experiencing high shear strain. This indicated that the geometry of the specimens may affect the energy dissipation.

The friction sliding occurring at the interfacial unbonded area between the fiber and the matrix material also plays a role in the damping properties of composites. However, it requires a certain amount of applied stress or strain to the composites to initiate the frictional sliding. Single-walled carbon nanotube-reinforced polycarbonate composites were produced and characterized in study [216]. It was found that the interfacial slip was activated at a low dynamic strain level (0.35%) at 90 ˚C. This strain was much lower than that in typical polymers [217]. This feature was believed to be the origin of the excellent damping in these composites. Additionally, the sliding became insensitive to dynamic strain when the strain amplitude was larger than 1.2%. In study [218], the friction coefficients of glass particles-filled polytetrafluoroethylene composites was characterized. It was reported that the average friction coefficient between the filler and the matrix is approximately 0.11, and the friction coefficient is negligibly affected by the size of the glass particles. The stick-slip friction phenomenon was found at the interface of the filler and matrix material in [219]. During the frictional sliding, a sudden increase and drop of friction force was observed. It was reported that the stick-slip (sometimes called "seating-unseating") cycle occurred at an interval of 10 to 20 μm, and it was believed that the cause of the stick-slip depended on the pattern of the surface asperities on the fiber and matrix interfaces. Detailed stick-slip friction was studied in [220]. The results showed that the stick-slip friction took place at a certain level of applied normal load. Based on the test results, the friction coefficient reached its maximum at about 8000 of the friction sliding cycles and showed a decreasing trend beyond this number of cycles.

An adhesion phenomenon occurs when the contacting surfaces approach closely enough. The energy dissipated in the irreversible process of adhesion may account for the damping mechanisms, and the energy dissipation is normally quantified by the hysteresis curve, which is obtained from one surface advancing and receding on another contacting surface. Adhesion hysteresis was observed between poly (dimethylsiloxanes) (PDMS) and the monolayer-coated mica surfaces in study [221]. It was concluded in the study that the magnitude of the adhesion hysteresis corresponded to the interfacial energy dissipation in a contacting and departing cycle. Another study [222] showed that the adhesion hysteresis was negligible between silane-coated surfaces in a condition of low relative humidity (less than 5%). However, a significant adhesion hysteresis increase was found after the surfaces were exposed to the ambient environment at 90% relative humidity. This indicated that the moisture had great effect on the adhesion process. It was believed that the adhesion hysteresis originated from the slow coalescence or chemical sintering reactions in the adhesion between metal and inorganic materials. In addition, a sudden decrease of the distance between two surfaces is often noticed during the adhesion process, such as AFM [223]. This phenomenon results in dramatic acceleration of the molecules attached to the contacting surface. Due to the adhesion being spontaneous, the dynamic energy obtained in the process is irreversible and finally dissipated as heat [224].

More mechanisms of damping, including viscoplastic damping (under the conditions of large amplitudes of vibration and high applied stress) [225] and thermoelastic damping (due to cyclic heat flow through the regions of tension and compression in the material) [226], will not be introduced in detail.

In the case of cellulose-reinforced composites, the base damping of polyamides is low (damping ratio is 0.39%) in nature. The damping attributed to the matrix material is minor. The damping improvement after the addition of cellulose indicates that the hidden mechanisms are potentially related to the interfacial mechanism. Due to the friction sliding often occurring at the unbonding area at the interface under moderate levels of loading and deformation, it is unlikely that friction sliding takes place in the free vibration test. Therefore, the most likely mechanism of energy dissipation in cellulose/polyamides systems is believed to be adhesion. More details are covered in the modeling part.

1.5 Modeling

While the damping properties of various composites have been characterized, extensive modeling work has been done to explain the mechanism of energy dissipation. In this part, analytical and numerical damping models of materials, including composites, are introduced. This part focus on current modeling work related to the energy dissipation in composites. The models are categorized based on the damping mechanisms.

1.5.1 Viscoelasticity in Matrix Material

For composites consisting mainly of a high-damping polymeric matrix, linear viscoelastic phenomenological models (such as Kelvin-Voigt, Maxwell, and Zener models) [227, 228] are commonly used to estimate the damping properties of the materials. These models are composed of a few linear spring and damper elements connected in parallel or in series. Using only a few parameters of the elements, the models predict the damping properties of the material with acceptable accuracy. In addition, they reduce the calculation effort in commercial FEA software. Based on these simple viscoelastic models, more damper and spring elements can be added to achieve better accuracy by accounting for different materials. Researchers built a modified fractional Kelvin-Voigt model in study [229] to describe the dynamic behaviors of biopolymer. It was reported that the model showed good correlation to the testing results for kuzu starch pastes. Additionally, this model was found to be more accurate in describing the viscoelasticity of the material than Maxwell-type models. In another study [230], the author proposed a fractional derivative viscoelastic model based on the properties of more than 30 materials. It successfully predicted the asymmetrical shape of the loss factor curve (the term also characterizes the damping capacity) of materials in a wide range of logarithmic frequency. Moreover, the asymmetrical shape of the loss factor curve was also described in study [231]. A modified fractional derivative Zener model was proposed. The results showed good fitting between the model calculations and the experimental data. It was concluded that the asymmetry of the loss factor peak and the dynamic behavior at high frequency was governed by the orders of time derivatives of stress and strain.

As the studies of energy dissipation mechanisms at the molecular level advance, models based on the dynamics of polymer chains are proposed. Crude models for polymer molecules consisting of a group of small particles interacting by elastic springs have evolved into detailed models with exact chemical structures and molecular bonding. In a system of interacting particles, it is believed that the energy dissipates between the regions when there is a great difference in the number of degrees of freedom [232]. A model composed of a chain of particles was built to explain this mechanism in study [233]. A particle in the center of the chain was set with an initial displacement. The results showed the displacement decay of the central particle, which indicated the energy lost to the rest of particle system from the central particle with only one degree of freedom. The decay was also found to be non-exponential and proportional to $t^{-1/2}$. Modified models were developed in the case of semi-infinite chains [234] and non-uniform chains [235]. A more detailed model was built and calculated by molecular dynamic simulation. In study [236], a molecular model of polyurethane/phenolic resin was developed with (COMPASS) force field [237] and simulated in a computer. It was found that the presence of hydrogen bonding in the resin increased the free volume. A low-energy barrier to rearrangement and movement of the polymer chain segments was found in the presence of high free volume, which resulted in great energy dissipation by the internal friction between polymer chains. In another study, polymer chains in different shapes were modeled and simulated. Higher hysteresis loss was found in a ring-shaped chain structure than in a crosslinked structure due to more internal sliding between chains. More models of polymer chains for damping study were reported in [238, 239].

1.5.2 Crack and Delamination

A variety of models have been developed to study the energy dissipation mechanisms from cracks and delaminations in composites. In study [215], a 2D finite element model was built to investigate the delamination propagation occurring at the surfaces of glass fiber and epoxy resin. It was shown that the region of high local shear strain gradually moved from the damaged spot to the intact spot as the tensile load increased. In addition, the area of the high shear strain increased with the increase in applied tensile stress. This indicates that energy dissipated through the nonlinear deformation from the shear force during the delamination. Crack resistance of particle-reinforced composites was studied by the model in [240]. The results showed that the particle size was irrelevant to the crack resistance. Moreover, the debonding energy increased with the increase of particle diameters. Both a finite element model and a molecular model were built to explore the deformation mechanism near the crack in study [241]. Defects, including dislocation and twin boundaries, were observed during the simulation and were viewed as major contributors to the energy dissipation. Additionally, it was reported that significant plastic deformation caused by dislocation occurrence and evolution near the crack tip region prevented crack propagation. In study [242], a molecular model consisting of thousands of atoms in a lattice structure was used to investigate the crack propagation phenomenon. The simulation results showed intersonic crack propagation and “mother-daughter” crack mechanism.

1.5.3 Interfacial Friction

Great effort has been taken in the study of the mechanisms of interfacial friction between the fillers and the matrix. Different types of friction models were developed and obtained good correlation to the damping test results. In aspects of an analytical model, an interfacial “stick-slip” friction mechanism between carbon nanotubes and matrix material was modeled in [243]; the effective shear stress at the interface during the frictional sliding was expressed by the elastic shear moduli of the filler and the matrix. A systematic parameter study was done on the model. It was reported that the damping ratios of the carbon nanotube-reinforced poly-ether-ether-ketone and epoxy composites were sensitive to the interfacial shear strain and strength. In addition, the damping ratio increased substantially with the increasing volume fraction of carbon nanotube filler. In another stick-slip friction model for carbon nanotube-reinforced composites [244], the author defined the stick-slip phenomenon by introducing critical stress. Interfacial slip occurred when the external loading exceeded the critical stress value. The energy dissipation was calculated by the phase lag of the critical stress and strain in one loading cycle. In study [245], a multiscale friction model was built to investigate single-walled carbon nanotube-reinforced composites. The shear stress at the interface during frictional sliding was investigated by a molecular dynamic model. This shear stress was used as the threshold of the slip initiation in the constitutive model of the composites. The studies above described the frictional sliding by the shear stress measured at the interface. However, none of these could show the details of the friction phenomenon in nano scale. Therefore, friction models based on the atomic or molecular dynamics were proposed. One of the most famous models is called the "Prandtl-Tomlinson" (PT) model [246]. This model described the friction forces from a single mass making contact with a surface in the presence of periodic intermolecular potential. Based on this pioneering work, vast numbers of molecular friction models were built. In study [247], researchers calculated the friction force from the model of AFM (similar to the PT model). It was reported that friction depended not only on the interaction potential between the surfaces but also on the construction parameters of AFM. A one-dimensional PT model was built to study the atomic stick-slip friction [248]. The features of the model included elastic potential, surface potential, and stochastic thermal-activation force. It was found that the thermal effect decreased the energy accumulation during sticking and increased the reversible energy when the slipping began. In study [249], the Frenkel-Kontorova (FK) model was proposed to account for the friction when a molecular chain is sliding on a substrate, and an improved version of the FK model called the

Frenkel-Kontorova-Tomlinson (FKT) model was built that included the feature of the contact size [250]. In addition, the behaviors of the intermolecular bonds affect the interfacial friction. A friction model was built with features of spontaneous dissociation and formation of the intermolecular bonds in study [251]. It presented that the stick–slip phenomenon started to occur when the sliding velocity was larger than a critical value. Another study [252] reported that temperature influenced the spontaneous dissociation and formation rates of the intermolecular bonds at the interface, which substantially affected the behaviors of the interfacial friction. Benefiting from advances in computation capacity, more detailed models were built and simulated by molecular dynamic simulation. Interfacial friction was studied in [253] by creating a model with spider silk molecules and diamond substrate. It was found that hydrogen bonding was essential to the increase of friction, especially at low sliding velocity. A similar study [254] also confirmed this conclusion.

1.5.4 Interfacial Adhesion

Adhesion is strongly affected by the intermolecular forces between the contacting surfaces. It requires a certain amount of energy to separate two contacting surfaces to infinite distance. This amount of energy, called adhesion energy, varies for different materials. However, a part of the energy will dissipate from the system during a sudden intermolecular change in state, termed an "intermolecular jump [224]." This phenomenon was observed in many AFM experiments [223] when two surfaces are brought close enough, the intermolecular force pulls the surfaces close to each other abruptly, and this sudden intermolecular distance change also occurs when these two surfaces are pulled so as to depart from bonded status with each other. In study [255], the author proposed a conceptual model similar to the structure of AFM, consisting of an elastic force and an intermolecular force. It showed that the "intermolecular jump" occurred when the gradients of the elastic and intermolecular force curves were the same. It was also reported that the jump process was spontaneous and irreversible. The energy during this process dissipated from the system as heat. During the approaching and departing of the surfaces (bonding and debonding cycle), there were two intermolecular jumps, which resulted in adhesion energy hysteresis. Based on this work above, a model was built with detailed intermolecular and elastic force functions to account for the adhesion hysteresis between a rigid micro-sized asperity and an elastic substrate [256]. Another study [257] showed adhesion hysteresis between inelastic contacting surfaces, while the composition of the model is similar to the studies above. A finite element model was created in study [222] to investigate the influence of moisture on the adhesion hysteresis of silane-coated surfaces. This dissertation focuses on the energy dissipation from adhesion.

1.6 Conclusion

Extensive review work has been done so far for cellulose, polyamides, cellulose-reinforced composites, and models for energy dissipation mechanisms in composites. Nanocellulose and bio-based polyamides are materials proposed for the next generation of composites, due to their renewable features, good mechanical properties, and potential energy dissipation capabilities. In the following chapters, details of the research work on cellulose-reinforced polyamides or PP will be covered, including the manufacturing process, characterizing approach and results, and evolution of the composites models.

Chapter 2 Samples Preparation

2.1 Materials

Three types of biocomposite fillers are used: CNC (NVC 100, manufactured by CelluForce); 4 µm and 100 µm cellulose particles (VIVAPUR CS 4 FM, VIVAPUR 102, both manufactured by JRS Pharma). Samples are manufactured by injection molding these fillers with (1) PA610 bio-based nylon resin (BASF), (2) PP (manufactured by RheTech), and (3) PA 1010 bio-based nylon resin (BASF) (only with CNC). The coupling agent PP-g-MA (manufactured by RheTech) is used in cellulose/PP composites.

2.2 Manufacturing

Sample preparation has been conducted using standard procedures on equipment at Ford Motor Company, Dearborn, MI. For cellulose-reinforced PA610 or PA1010 composites, all the materials are dried in an oven at 80°C for about 16 hours and then extruded in a double screw extruder (Davis Standard H-series, DS-15HM). For cellulose/PP composites, only the cellulose filler is dried. The drying process for PP is skipped due to its hydrophobic nature. The extruding temperature setup along the barrel of the extruder is shown in the following table:

Table 2.1. Temperature setup for extrusion

Composites	Temperature at different positions along the barrel (˚C)						
	1	2	3	4	5	6	7
PA610/cellulose	215	215	220	220	225	225	230
PA1010/CNC	200	200	205	205	210	210	215

PP/cellulose	175	175	180	180	185	185	190

The positions 1 to 7 represent the locations from the feed hopper to the nozzle. Each temperature is measured by thermocouples located at the top of the barrel. The screw speed is set at 200 rpm. The filler and matrix material are fed by two separate feeders at speeds calibrated to provide a constant mass ratio of filler material in the composites. The compounded materials are then re-dried, chopped, and re-extruded to ensure good material mixing.

For the injection molding process, an 80-ton BOY screw-fed injection molding machine (Dr. Boy GmbH & Co., Germany) is then used to produce ASTM-standard tensile (Type 1) and bending bars having fiber mass ratios of 0% (control), 2.5%, 5%, and 10%. The temperature setup for the injection molding machine when producing specimens is shown in the table below:

Table 2.2. Temperature setup for injection molding

Composites	Temperature at different positions along the barrel (˚C)				
	1	2	3	4	5
PA610/cellulose	240	245	250	255	260
PA1010/CNC	225	230	235	240	255
PP/cellulose	195	200	205	210	215

Positions 1 to 5 represent the locations from the feed hopper to the nozzle. Based on the processing parameters of pure polymer materials, several important parameters are investigated and modified to obtain good-quality composite specimens. Table 2.3 shows the important processing parameters:

Table 2.3. Processing parameters for injection molding composites

Composites	PA610/cellulose	PA1010/CNC	PP/cellulose
Screw speed (rpm)	80	80	70
Back pressure (kPa)	586	610	689
Hold pressure (kPa)	8000	7600	5000
Hold time (s)	5	5	1
Cooling time (s)	25	25	25
Mold Temperature (˚C)	60	55	29.4

Because the machine will be purged by pure polypropylene (PP) before each run, to eliminate the influence of PP on the composites, each sample will be weighed when the injection molding machine starts to produce samples. All samples of light weight will be discarded until the weight of samples stabilizes. The weight change of the injection molding parts (control PA610) is shown in the figure below:

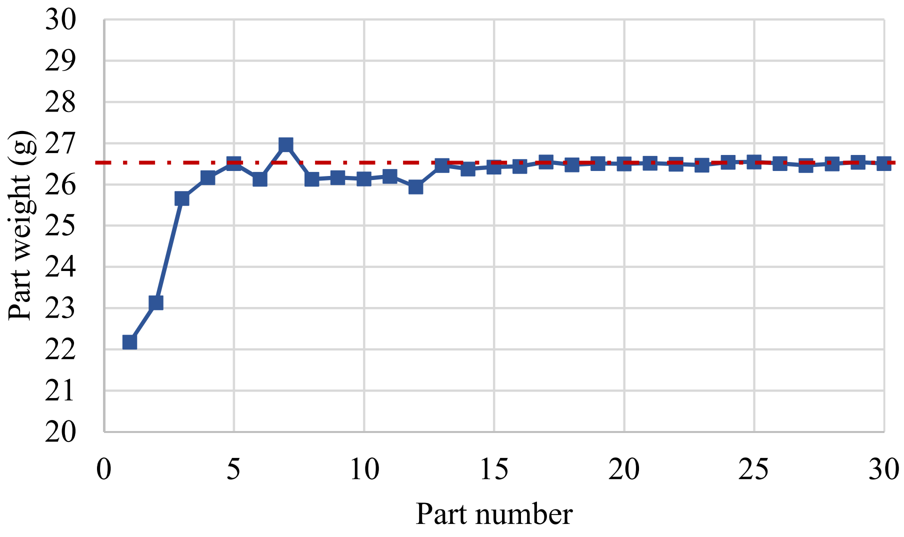

Figure 2.1. The weight change of the injection molding PA610 parts.

The dashed red line in the graph in Figure 2.1 indicates that the mean weight of the injection molding parts is around 26.5 grams. The first three parts are abandoned due to the large deviation of the weight compared to the average value.

After the production of the samples, each sample are carefully checked and samples with flaws discarded. All the samples are preserved in plastic bags with a zip lock to prevent moisture absorption by the samples.

2.3 Common Defects of the Parts and Solutions

Production of test specimens without defects is essential for characterizing the material properties accurately. This part discusses the common defects that occur during injection molding. The solutions to prevent defects are also introduced.

Flow line is one of the most common defects in injection molded parts. It occurs when the melted material in the mold cools down at different rates. Normally, the flow lines are along the directions of the melted material flow, and they appear in the center of the parts. This defect may affect the mechanical properties of the specimens. Figure 2.2 shows the flow lines in a PA610 control sample.

Figure 2.2. Flow lines in an injection molded part.

Vacuum voids are pockets of air trapped in the injection molded parts, as shown in Figure 2.3:

Figure 2.3. Vacuum voids in an injection molded part.

After application of external loading, these voids introduce stress concentrations in the specimen. Voids can cause a reduction of strength and also initiate a crack that leads to the failure of the material. The reasons for vacuum void formation vary. In the case of PA610-based composites, moisture remaining in the material is one of the potential causes of the voids. At the PA610 melting temperature, the moisture absorbed in PA610 and cellulose starts to evaporate and escape from the material. However, the moisture is constrained in the enclosed mold and then forms vacuum voids in the parts. In addition, it is found that voids start to build in the specimen when the holding pressure is smaller than 3100 kPa during manufacturing. Therefore, careful moisture removal and appropriate holding pressure are essential for avoiding vacuum voids.

Sink marks are craters and depressions that develop on the surface of injection molded parts. They occur in PA610/cellulose specimen production, as shown in Figure n. During tensile tests of composite specimens, this defect causes slip at the gripping regions because of the reduction of the gripping area. Sink marks originate from shrinkage of the materials, which takes place when the cooling time is too short. Moreover, insufficient holding pressure and time also contribute to sink marks.

Figure 2.4. Samples with (left) and without (right) sink marks.

Flash is the defect of a thin layer of material attached at the edge of the injection molded specimen, which is shown in Figure 2.5. It forms when the melted material escapes from the mold and cools in the gap of the mold. Even though this defect has minor influence on the mechanical properties of the samples, it creates difficulties in measuring the mass of each specimen. The main cause of flash is normally excessive holding pressure. If flash still exists after application of an appropriate holding pressure, decreasing the shot size of the injection molding can be an effective correction.

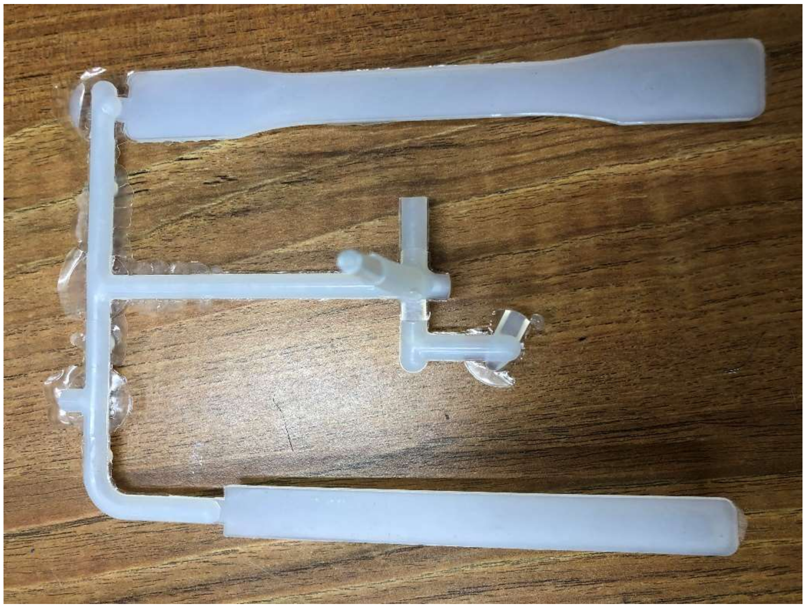

Figure 2.5. Flash on the edge of an injection molded part.

2.4 General Observations

The control PA610 and PA1010 samples have a gray, translucent appearance, while the PP samples are white and more transparent than PA610 and PA1010. After the addition of cellulose fiber, the color of the PA610 and PA1010 samples is black at all levels of filler loading, while the color of PP samples is from light to deep brown as the mass ratio of the filler increases. Some small particles can be seen in the specimens at low filler load (2.5%) by visual inspection. The surface of all samples is smooth to the touch, slightly rougher than the control ones, and there is a roast wheat smell from the specimens after they are filled by cellulose. Figure 2.6 shows the appearance of the samples.

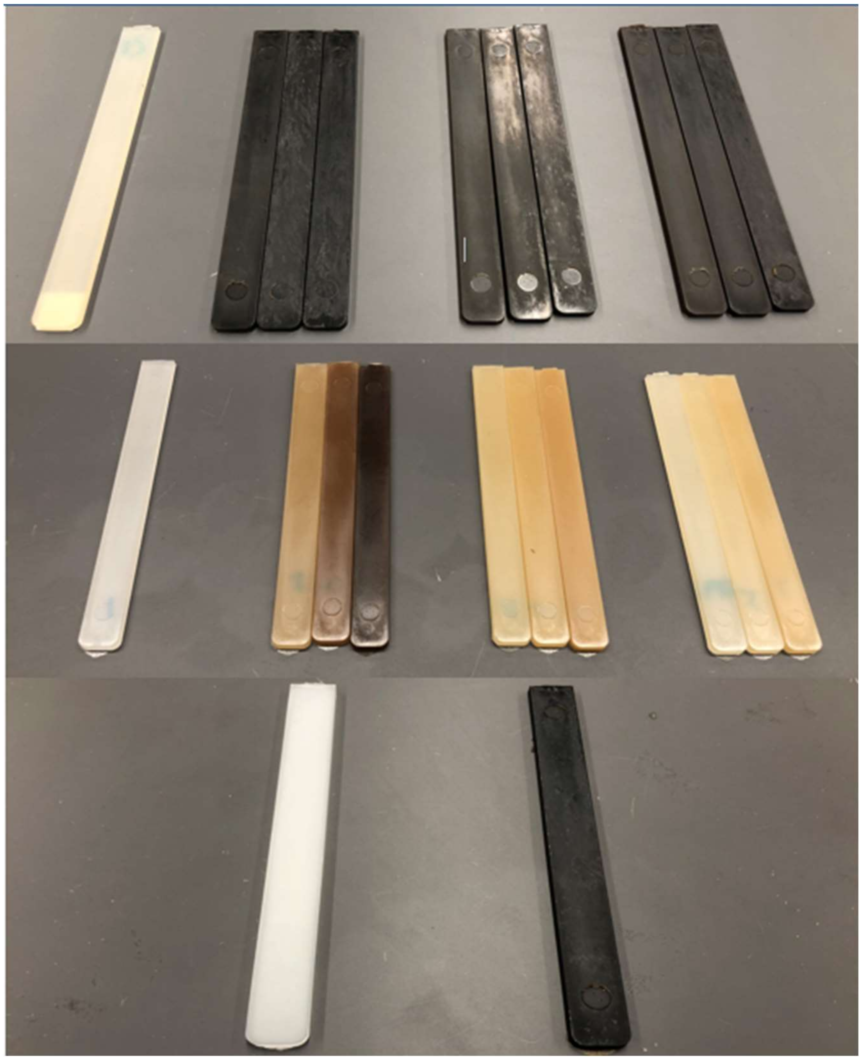

Figure 2.6. Appearance of the parts. First row, PA610: left to the right- control; 2.5%, 5%, 10% CNC filled; 2.5%, 5%, 10% 4μm cellulose filled; 2.5%, 5%, 10% 100μm cellulose filled. Second row, PP: left to the right- control; 2.5%, 5%, 10% CNC filled; 2.5%, 5%, 10% 4μm cellulose filled; 2.5%, 5%, 10% 100μm cellulose filled. Third row, PA1010: left to the right- control; 5% CNC filled.

Chapter 3 Mechanical Testing

3.1 Mechanical Testing System Overview

The mechanical tests are performed on a testing system (see Figure 3.1) that is designed for rate testing. It includes a gripping system with ball bearing rails, compressed air-activated impact system, actuator with high precision, controller, and data acquisition system, and has been used for a variety of materials [258-262]. For the gripping system, different types of grips can be used depending on the surface roughness and the stiffness of the samples. For the controllers, both are used for the low rate and impacted tests, respectively. They collect data from the force cell, which is attached to the grip. For the low rate test, it controls the actuator to push grips apart. The compressed air-activated impact system consists of a steel pressure vessel with a valve and a steel barrel that guides the direction when shooting a steel cylinder. The testing rate can be switched by changing loading means between actuator and impact steel cylinder.

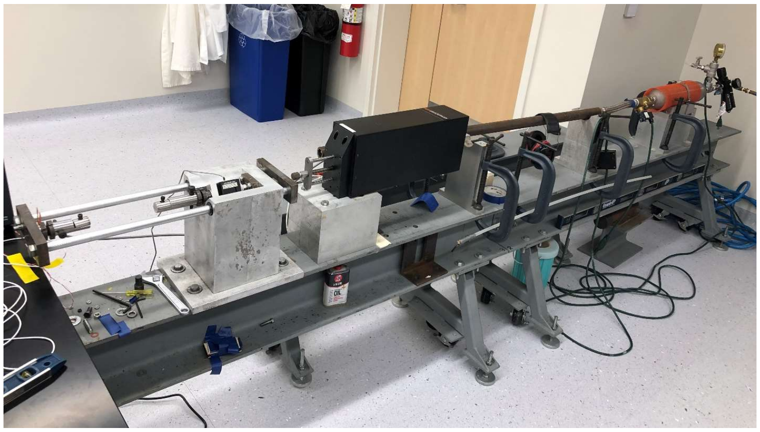

Figure 3.1. Tensile test machine.

Heating and cooling chambers (shown in Figure 3.2) can be fit between grips to enable testing at various temperatures. The heating chamber contains a heating coil inside of the chamber wall. A K-type thermocouple is attached on the inner wall in the heating chamber to monitor the heating temperature and temperature is controlled by a PID controller incorporating a relay. When the heating chamber reaches the desired temperature, the controller sends a signal to the relay, which will switch off the heating process. When the temperature begins to drop, the heating will turn on. The cooling chamber is made of aluminum with two plastic caps. The cooling channels are distributed inside of the wall of the chamber. Liquid nitrogen flows through the channels. The temperature is monitored and controlled by opening and closing the valve of the liquid nitrogen input.

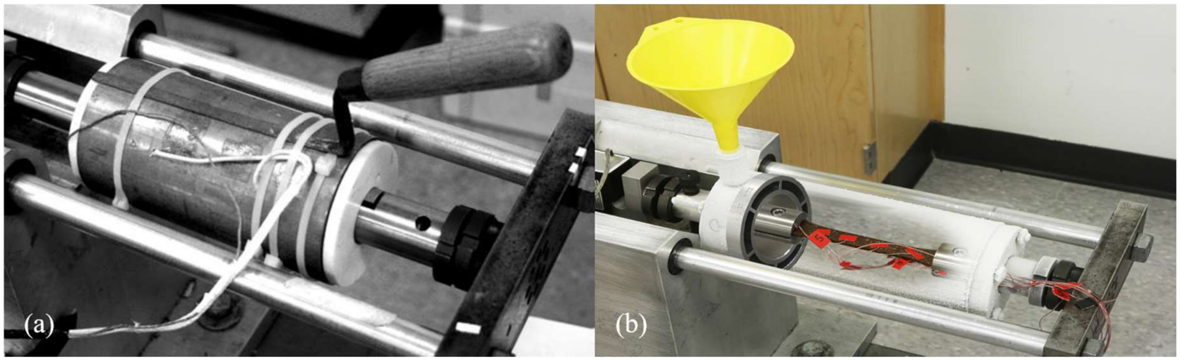

Figure 3.2. Hot chamber (a) and cold chamber (b). (from [263])

3.2 Mechanical Testing Procedures

The tensile tests in this dissertation are performed under four different strain rates: quasi-static (0.0005/s), moderate (0.025/s), and high (14/s, 26/s). For the quasi-static and moderate rates, the mechanical testing system is switched to actuator loading. Before the testing, the specimens are carefully checked so that there are no obvious flaws in them. Each batch of samples is numbered after the order in which they were manufactured. Three specimens are picked by the number on them at an interval of at least 10. This method increases the randomization of the testing results. After the samples are prepared, holes at each gripping area of the samples are drilled. To reduce slipping at the grip, the specimens are fastened between the grips by screws going through these holes. The dimensions of the samples, including the width, the thickness, and the distance between the grips, are recorded. Each dimension is measured at three different spots on the specimen and averaged by three measured values. The dimensions are used to calculate the stress and strain after testing. The testing profile set in the controller of the actuator includes the loading rate, the extreme position of loading, and the data logging rate before testing. The test begins after the steps are done in the description above. The test ends when the material fails or reaches the set extreme position. After testing, the samples are properly stored in zip-seal bags with testing information. The testing data are saved and transmitted to the computer for later use.

For the high-rate testing, the loading is switched to the impact steel cylinder launched by compressed air. The samples are prepared and gripped the same as for the testing at the quasi-static rate. To compensate for the noise generated by the vibration after the impact, two acceleration sensors are attached on the nearby surfaces at the two grips. Compressed air is injected into the pressure vessel. The pressure values shown on the gauge are recorded for later use. The steel impact cylinder is then pushed into the barrel that is connected to the outlet of the pressure vessel. When the valve is opened, the steel cylinder is launched and hits the bar, which is connected to the ball bearing rail and the grips. The specimen is thereby stretched. To obtain the desired peak strain rate (shown in Figure 3.3) for different materials, several trial impact tests are necessary before the final tests. Three tests need to be done for each formula of the material. Data are collected using a four-channel OROS data acquisition system (OR34).

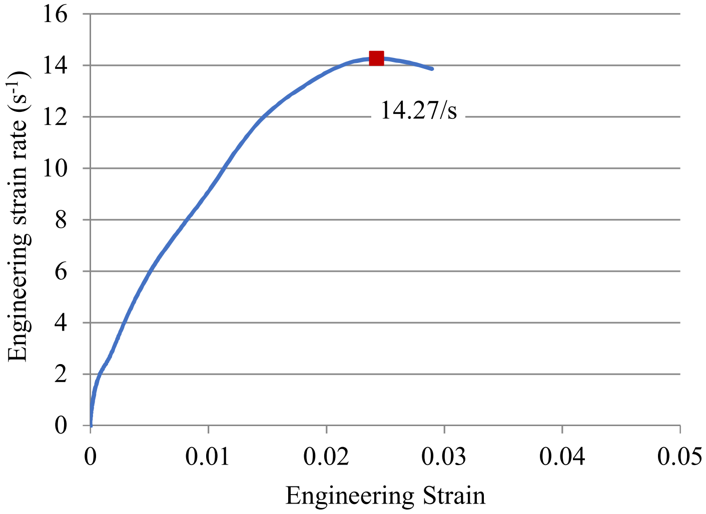

Figure 3.3. Engineering strain rate vs strain curves of 5% nano-cellulose fiber-reinforced PA610 at rate of 14/s.

The hot tests are conducted with the hot chamber. The temperature is monitored and controlled by a thermocouple attached on the inner wall of the chamber. To access the temperature of the specimen, calibration tests on dummy samples are carefully done as in the following description. A specimen is gripped at one side and a K-type thermocouple is attached on the surface of the specimen. Then the heating chamber is put on with the specimen sliding into it. The specimen is gripped at the other side. Another thermocouple is placed inside of the chamber to collect the data of the ambient temperature. After the heating starts, the time is recorded when the temperature of the sample reaches the desired value and becomes stable for 10 minutes. If the temperature is not stable in the end, the setting of the controller needs to be adjusted until the temperature is finally stable. The deviation of the temperature should be less than 2 ˚C. Then the controller setting and the heating time are recorded to be used in the hot tests later. In the hot test, the sensors attached on the samples are removed. It follows a similar procedure as in the calibration tests, with recorded controller settings and heating times. Three tests are conducted for each formula of specimen.

For cold tests, the cold chamber is placed between the grips. Liquid nitrogen is obtained from the pressure vessel and temporarily stored in a thermos flask. After the sample is gripped, a thermocouple is placed inside of the chamber to monitor the ambient temperature. Similar to the hot tests, calibration is done for a dummy sample with a thermocouple attached on the sample surface. Then the liquid nitrogen is filled into the channels of the chamber. The volume of the liquid nitrogen is controlled by the valve. The temperature will be stable at the desired temperature with deviation at approximately 3˚C. The cold tests are then conducted.

3.3 Results for Cellulose/PA610 Composites

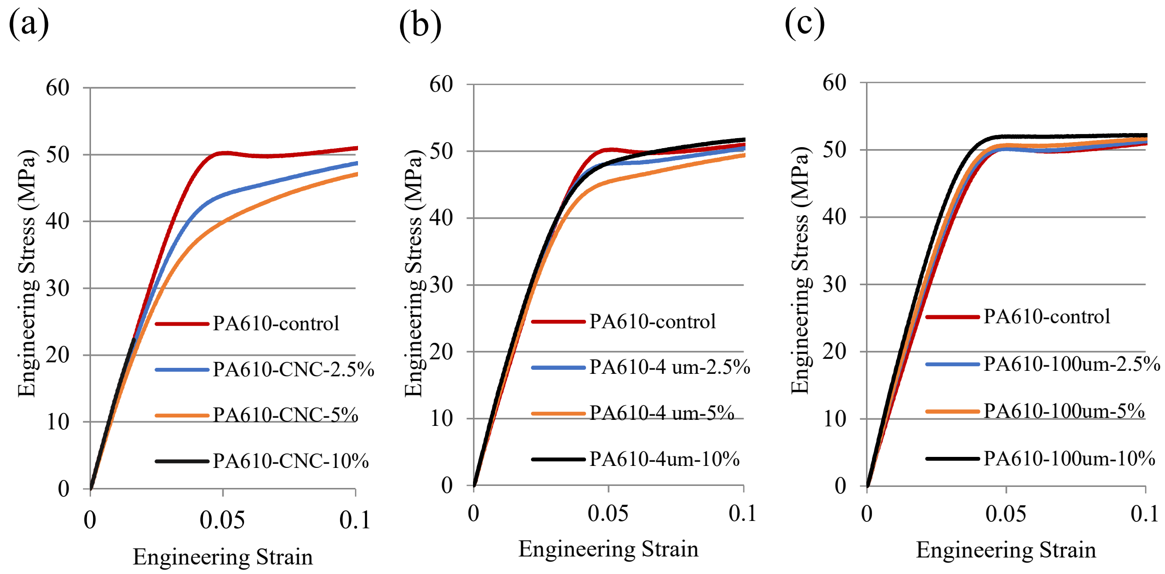

Figure 3.4. Stress-strain curves of cellulose reinforced PA610 at 3 weight ratios of filler (2.5%, 5%, 10%) and 3 filler sizes (a) CNC, (b) 4 µm, (c) 100 µm. Tests conducted at strain rate of 0.0005/s at room temperature (23°C) approximately 20 days after drying.

Figure 3.4 shows the results of tensile stress-strain tests conducted at a constant strain rate of 0.0005/s at room temperature (23 ˚C). Each stress-strain curve is an average of tests on three specimens. Each curve ends at the minimum failure strain of the 3 specimens or at 0.2, which is the set maximum strain of the test, if failure did not occur. In all cases, the elastic modulus is negligibly affected by the addition of cellulose. In the 2.5% and 5% cases in Figure

2(a), CNC is seen to soften the response at strains beyond about 0.05, and softening increases with increased percentage. In the larger-fiber cases, Figures 2(b) and 2(c), the softening effect observed in Figure 2(a) diminishes and the response of the composites approaches that of the control.

Table 3.1. Mechanical properties of PA610/cellulose composites.

Composites	Filler Mass Ratio	Young's Modulus (MPa)	Peak Stress (MPa)	Failure Strain ("-" means no break)
Control PA610	0	1371.4	53.1	-
CNC/ PA610	2.5%	1356.7	52.3	-
	5%	1276.8	50.2	0.1724
	10%	1420.9	22.3	0.0164
4 μm cellulose/ PA610	2.5%	1465.8	53.0	-
	5%	1431.0	52.1	-
	10%	1522.3	52.4	0.1392
100 μm cellulose/ PA610	2.5%	1499.9	53.1	-
	5%	1529.9	52.8	-
	10%	1672.2	52.2	0.1206

In Table 3.1, values of the Young's modulus are calculated at the strain 0.01. In addition to the softening response of CNC-reinforced PA610, the stiffening effect start to appear as the particle size increases. 100 μm cellulose-reinforced PA610 has the highest increase (22 percent based on the control PA610) of Young's modulus at 10% filler mass ratio compared to other composites. A minor decrease of the peak stress with the addition of cellulose is observed. For

10% CNC-reinforced PA610, a low failure strain is noticed. It is believed that the poor adhesion and flaws at the filler and matrix interface results in crack propagation and failure, and the case become more severe for nano-sized particles at a high filling ratio.

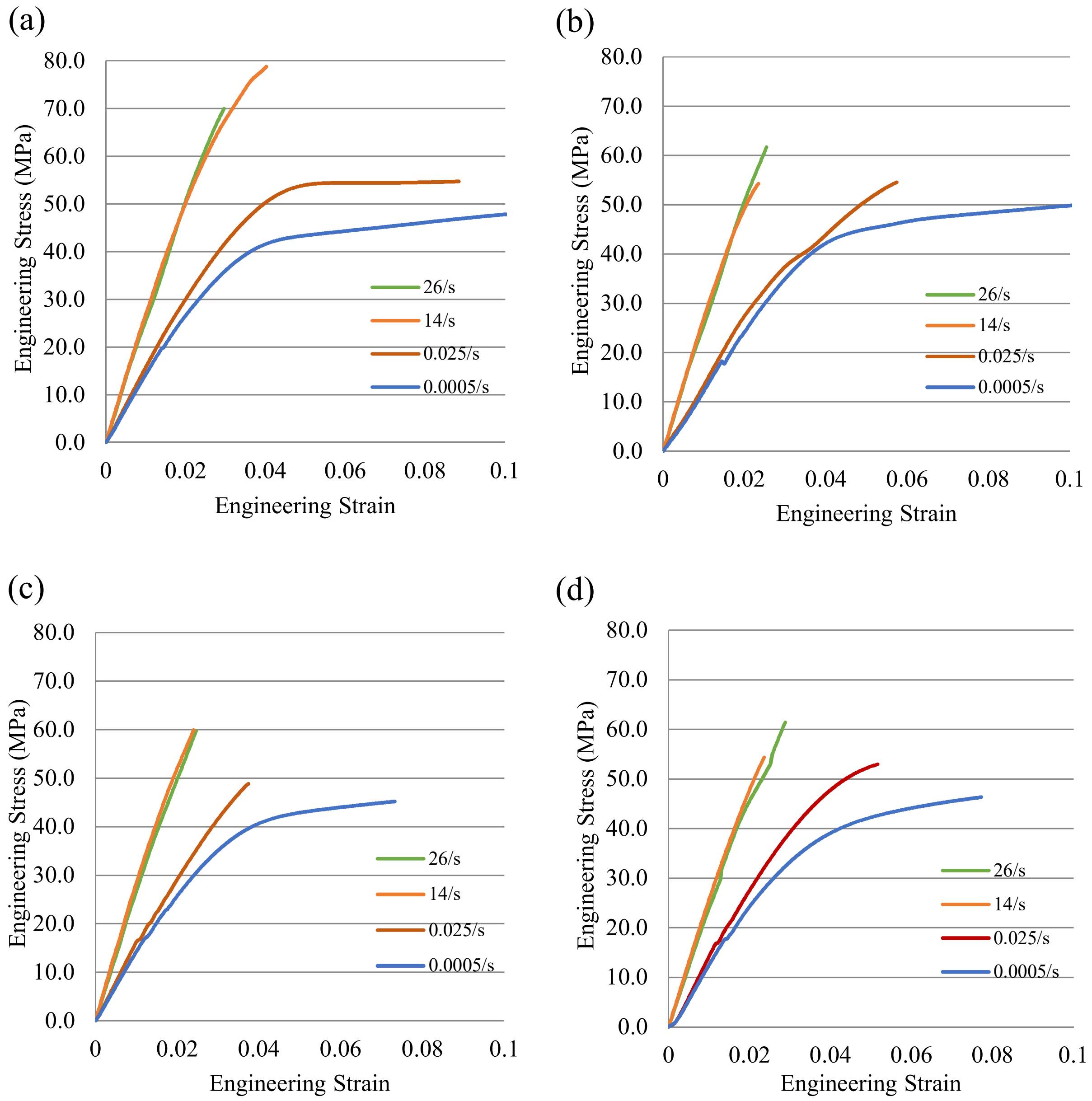

Figure 3.5. Stress-strain curves of (a) control, (b) 2.5%, (c) 5%, and (d) 7.5% CNC reinforced PA610 at four strain rates. Tests conducted at room temperature (23°C) approximately 2 months after drying.

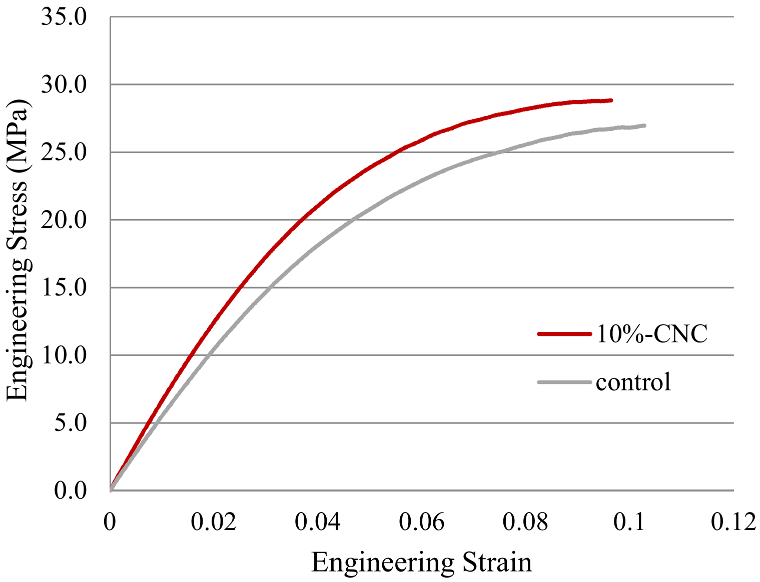

Figure 3.6. Stress-strain curves of control and 10% CNC reinforced PA610 at strain rate 14/s. Tests conducted at hot temperature (105 °C) approximately 2 months after drying.

Tensile tests at various strain rates and temperatures are given in the following graphs. All results are an average of 3 tests. Rate dependence of CNC-reinforced PA610 is shown in Figure 3.5 for strain rates of 0.0005/s, 0.025/s, 14/s, and 26/s. These tests were conducted at room temperature. Stress-strain curves at higher rates generally have larger Young's modulus and tensile strength but smaller failure strain, as is typically found in polymeric composites. The effect of cellulose fillers on the stress-strain behavior at this temperature is seen to be minor. However, at moderately high temperature (Figure 3.6) the addition of 10% CNC to the control is seen to reduce the typical loss of stiffness and strength typically found in the high-temperature response of polymers.

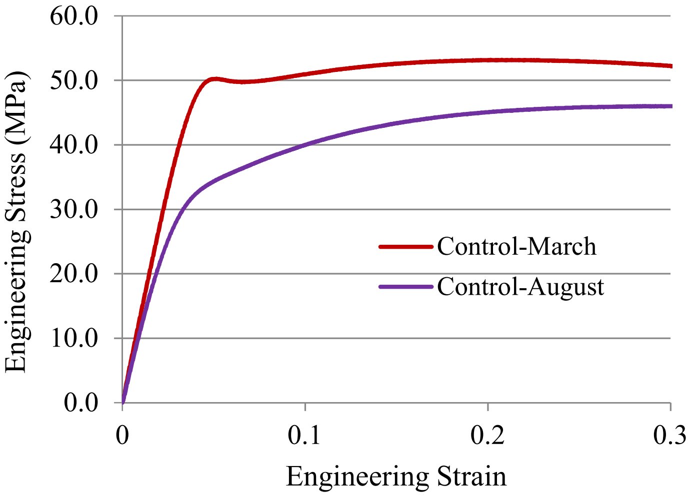

Figure 3.7. Stress-strain curves of control PA610 samples at strain rate 0.0005/s. Samples are from same sample batch tested in March and absorb moisture in 5 months (August) at room temperature.

PA610 is a hydrophilic material, which tends to absorb moisture from the ambient environment. Figure 3.7 presents the stress-strain behavior of the PA610 before and after it absorbs moisture. It shows that the moisture softens the material and decreases its tensile strength. It is believed that moisture absorbed in the PA610 weakens the intramolecular bonding between PA610 polymer chains.

3.4 Results for Cellulose/PA1010 Composites

Figures 3.8 and 3.9 give results for cellulose-filled PA1010 composites. The stress-strain behavior of the nano-filled material is compared to the control at 3 temperatures for the case of quasi-static testing rate in Figure 3.8. In Figure 3.9, results are given at three testing rates. These materials all exhibit rate hardening phenomena similar to the PA610 composites. Changes in the stress-strain behavior from the addition of the filler to this polymer are seen to be negligible at all three temperatures and strain rates. This trend is similar to the behavior of the cellulose-reinforced PA610.

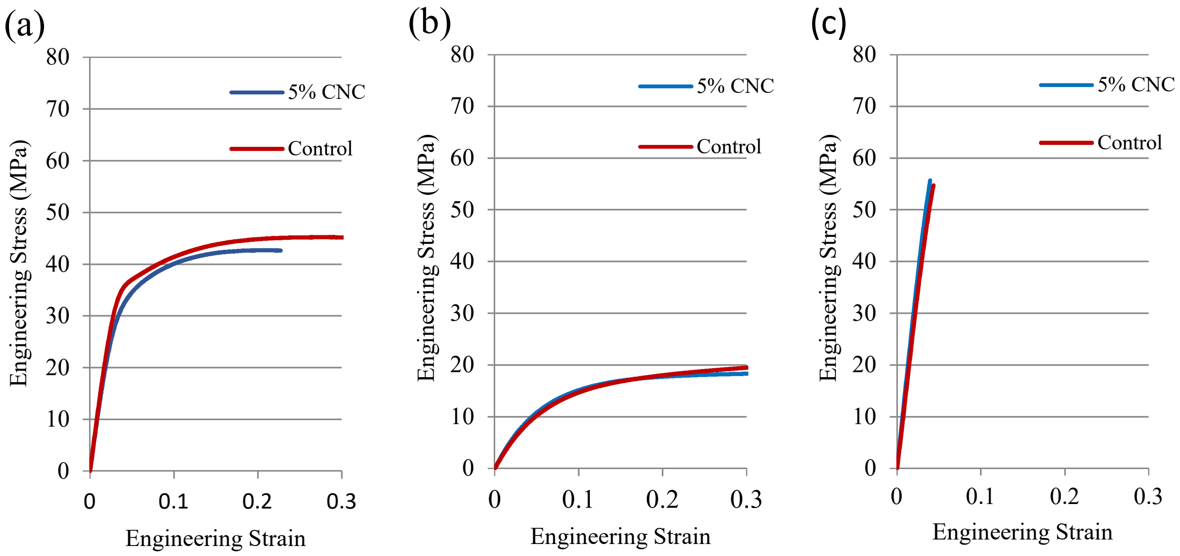

Figure 3.8. Stress-strain curves of control and 5% CNC reinforced PA1010 at strain rate 0.0005/s. Tests conducted at 3 temperatures: (a) room (23°C), (b) hot (105 °C), (c) Cold(-30°C).

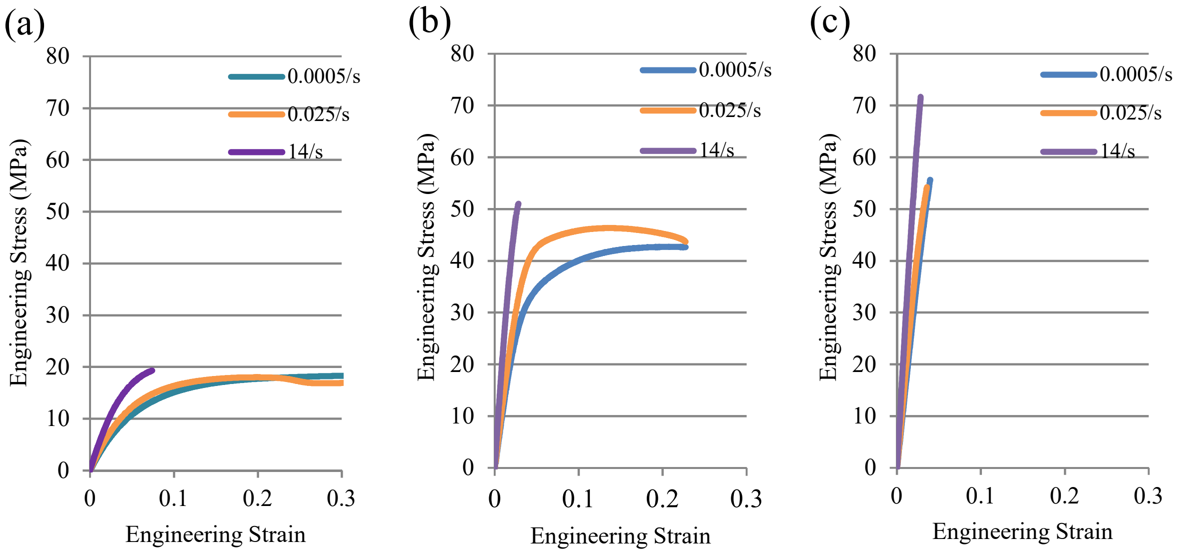

Figure 3.9. Stress-strain curves 5% CNC reinforced PA1010 at 3 strain rates 0.0005/s, 0.025/s and 14/s. Tests conducted at 3 temperatures: (a) room (23°C), (b) hot (105 °C), (c) cold (-30°C).

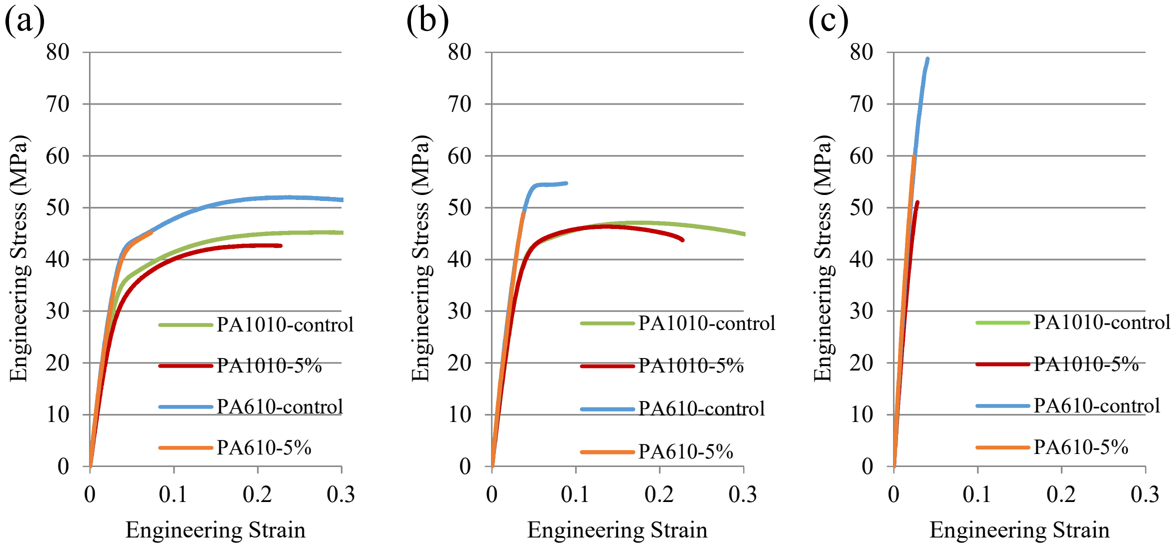

Figure 3.10. Stress-strain curves 5% CNC reinforced PA1010 and PA610 at room temperature (23°C). Control PA610 and PA1010 curves are used for comparison. Tests conducted at 3 strain rates: (a) 0.0005/s, (b) 0.025/s, (c) 14/s.

Figure 3.10 shows the comparison of the stress-strain behaviors between CNC-reinforced PA610 and PA1010. The elastic modulus and tensile strength of CNC-reinforced PA610 is higher than that of CNC-reinforced PA1010. However, the failure strain of CNC-reinforced PA1010 is larger than that of CNC-reinforced PA610 at low strain rates. The results indicate that PA1010 composites are more suitable to application as energy-absorbing material for their lower stiffness and stress compared to PA610 composites.

As shown in Figure 3.11, minor improvement of stiffness occurs with the addition of cellulose to PP. Similar to the case of cellulose-reinforced PA610 composites, CNC softens the response at strains beyond 0.03. Some stiffening effect can be seen in 4 μm- and 100 μm-sized cellulose/PP composites. This trend corresponds to Figure 3.11, in which a larger sized particle produces better improvement in the stiffness of the composites. This indicates that the size of the filler particles has significant effect on stiffening the matrix material.

3.5 Results for Cellulose/PP Composites

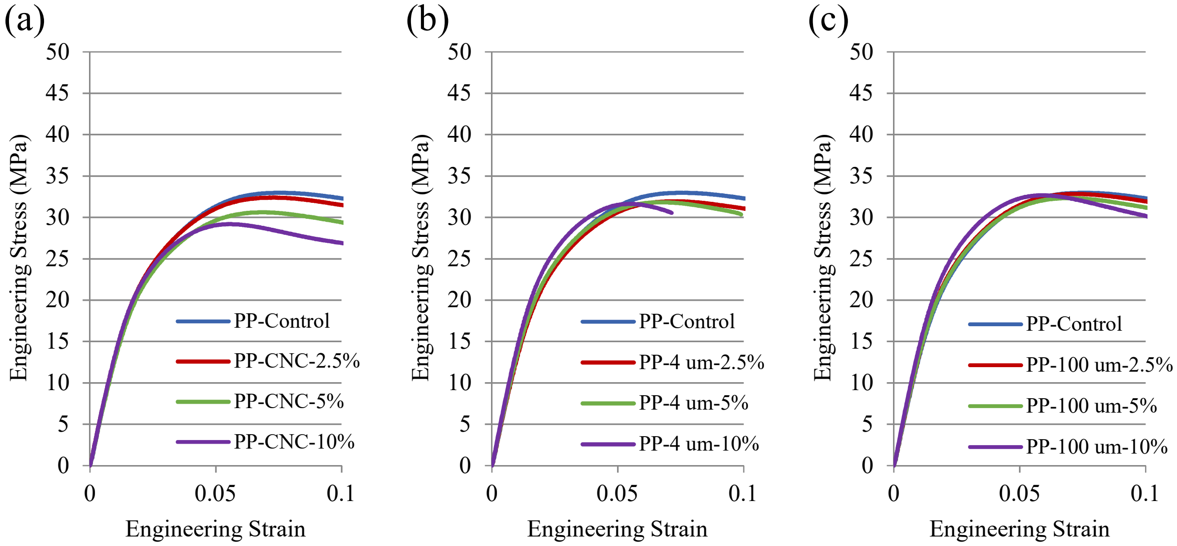

Figure 3.11. Stress-strain curves of cellulose reinforced PP at 3 weight ratios of filler (2.5%, 5%, 10%) and 3 filler sizes (a) CNC, (b) 4 µm, (c) 100 µm. Tests conducted at strain rate of 0.0005/s at room temperature (23°C).

Table 3.2. Mechanical properties of PP/cellulose composites

Composites	Filler Mass Ratio	Young's Modulus (MPa)	Peak Stress (MPa)	Failure Strain (“-” means no break)
Control PP	0	1302.2	33.0	-
CNC/ PP	2.5%	1328.3	32.4	-
	5%	1278.5	30.6	0.1668
	10%	1339.6	29.2	0.1436
4 µm cellulose/ PP	2.5%	1297.0	31.9	0.1572
	5%	1332.6	31.8	0.0990
	10%	1423.0	31.6	0.0710

100 μm cellulose/ PP	2.5%	1324.7	32.8	0.1496
	5%	1330.0	32.3	0.1692
	10%	1427.1	32.7	0.1024

In Table 3.2, similar to the case of cellulose-reinforced PA610, a softening response is seen in CNC-reinforced PP, and the Young's modulus increases with the mass ratio of the filler. As the particle size increases, the filler starts to stiffen the matrix material. The peak stress decreases with addition of cellulose in all sizes, and it also tends to decease when the mass ratio of the filler increases. However, it is different from the case of cellulose/PA610 composites in that CNC-reinforced PP has the largest failure strain compared to larger-size fillers. This indicates good adhesion at the interface between CNC and PP. It is believed that the coupling agent used in compounding accounts for the good bonding. In addition, PP/CNC composites are processed at 190 ˚C, which is lower than that of PA610/CNC composites (230 ˚C). Degradation of CNC is less at lower temperature. Thus, fewer flaws at the interface of CNC and PP are expected compared to that of PA 610 and CNC.

Chapter 4 Damping Testing

4.1 Damping Testing System Overview

The damping test apparatus is shown in Figure 4.1. A test sample is clamped in a cantilever arrangement. The displacement measurement of the free end is made by a fiber optic displacement sensor (Philtec Model RC63+LQ) that is attached to an adjustable support and aimed at a small piece of aluminum tape attached to the free end of the sample. The distance between the tape and sensor is adjusted to 5mm, which is in the center of the optimal range for this sensor. The cantilevered length of the sample is 95 mm (see Figure 4.1, and its thickness is about 3.14 mm ± 0.01 mm. Data is collected using a four-channel OROS data acquisition system (OR34).

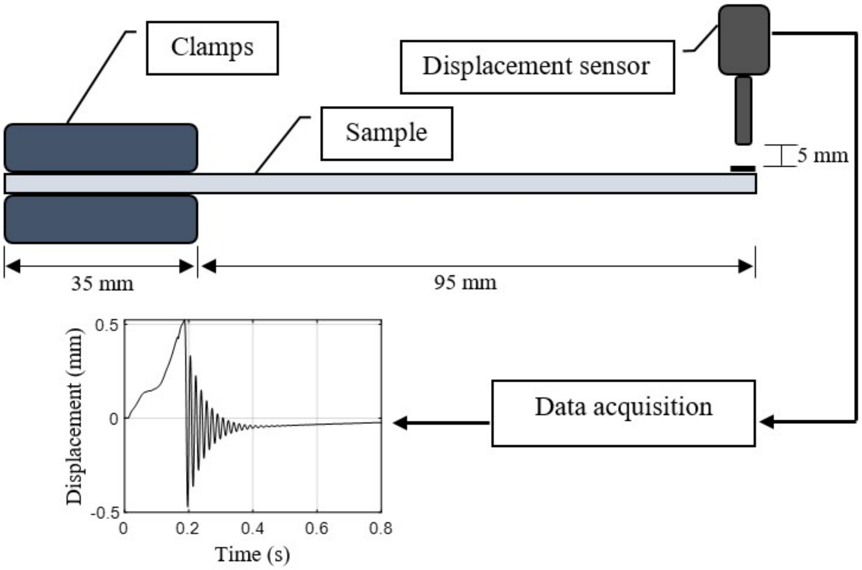

Figure 4.1. Schematic of the damping testing system.

4.2 Damping Testing Procedures

Free vibrations are excited in the sample by deflecting its tip about 0.5 mm and releasing it from rest. The decay of vibration from the tip of the sample is measured and collected by the sensor. The rate of the vibration decay δ, which is defined as:

$$\delta = \frac{1}{w} \ln \frac{X_{u+w}}{X_u} \tag{4.1}$$

w, u are the number of the peak displacement during the vibration. x is the peak displacement. The decay of the vibration is shown in Figure 4.2.

The dimensionless damping ratio ζ that characterizes the energy dissipation capability of the material is calculated by the rate of the vibration decay. It is given as:

$$\zeta = \frac{\delta}{2\pi} \tag{4.2}$$

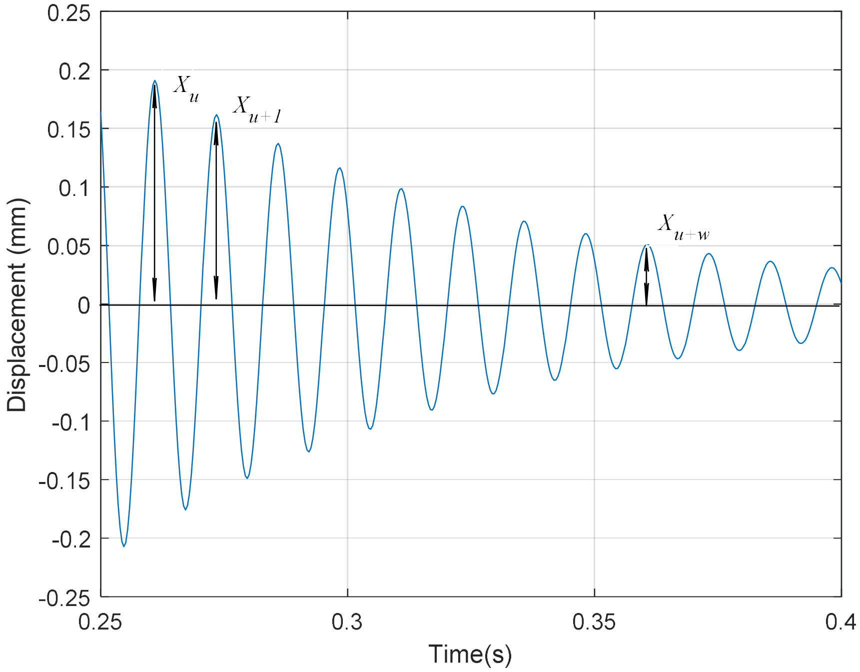

Figure 4.2. Response of the free vibration test.

For damping tests at different temperatures, a heating chamber and a refrigerator are used to provide the desired environmental temperature. The heating chamber is made of transparent plastic plates in a thickness of 1 cm. The temperature in the chamber is controlled by a heating coil connected to a PID controller. Ventilation is achieved by a computer fan mounted in the chamber. The cold test is conducted in a lab refrigerator, which can easily maintain the desired temperature for a long time.

To assess the temperature of the samples without using an attached sensor, which would disrupt the damping measurement, a pre-test calibration procedure using a dummy, surrogate sample is used. This procedure assures the actual test sample's internal temperature is at the desired value by relating the sample's internal temperature to its surface temperature and the heating time. In the calibration process, thermocouples are mounted in three small, sealed holes at both ends and the midpoint of the dummy sample to monitor its internal temperature along its length. Another thermocouple is mounted on the surface of the dummy sample and another in the open space of the chamber. As the chamber is heated, the temperatures of the surface and interior of the dummy sample coalesce and approach the target temperature. Specifically, in the heating case, after the chamber temperature reaches 3°C above the target value and is maintained for 3 minutes, the temperatures on the surface and inside the sample reach the target value. In the actual damping test, a thermocouple is mounted to the surface of the actual test sample (no holes in the sample are needed) and in the air of the chamber. The test is initiated three minutes after the set-point surface temperature occurs by removing the thermocouple and then exciting the sample using small access holes in the wall of the chamber. Cold tests are conducted similarly.

4.3 Results for Cellulose/PA610 Composites

4.3.1 Dry samples

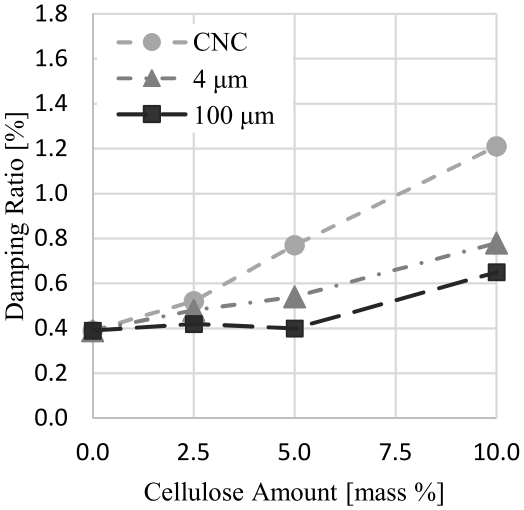

Figure 4.3. Damping tests on cellulose reinforced PA610 dry samples immediately after manufacture.

Figure 4.3 presents damping test results of dry PA610/cellulose samples at 23 ˚C as functions of fiber mass percentage. Each damping ratio value is averaged by the data of 3 samples. PA610/cellulose composites are seen to have increased damping ratio relative to control PA610 in all cases.

In the damping tests of dry samples, Figure 4.3, the presence of cellulose in the composite is seen to increase the damping ratio compared to unreinforced PA610. Also, the damping improvement increases with reduction in the size of cellulose, with the CNC composite giving a 210% increase in the 10% mass fraction case.

The strong damping elicited by CNC in these composites is in line with dramatic increases in damping observed in nanoscale materials such as carbon nanotube systems [201, 264, 265], attributed to large interfacial surface area between the filler and matrix. However, a recent study found a decrease in damping by the addition of nano-sisal whiskers to polylactic acid [266]. Furthermore, the damping increase in the polypropylene/CNC composites shown in Figure 4.7 is not as pronounced as in the PA610/CNC case. These studies indicate that the damping properties of composites may depend on the energy dissipation mechanism at the interface of the filler and the matrix materials, and the chemical properties of the materials may play a role in the behavior. In PA610/cellulose composites, the adhesion between cellulose and PA610 is primarily caused by the Van der Waals force and intermolecular hydrogen bonds. Depending on the relative magnitude of these adhesive forces compared to the elastic forces, sudden intermolecular distance changes can occur [255] resulting in sudden increase in molecular kinetic energy that is subsequently dissipated as heat. This intermolecular phenomenon has been demonstrated in atomic force microscopy experiments [223]. In the present case of PA610/cellulose composites, modeling shows that hydrogen bonding is critical for the phenomenon to occur and is predicted to be largest for CNC since it has larger interfacial surface contact area with PA610 than do the larger fiber cases[267] . This is thought to be the key source of the large increase in damping observed in Figure 4.3.

4.3.2 Effects of Moisture and the Drying Process

Because PA610 is hydrophilic, composites containing the polymer tend to absorb moisture under ambient conditions. After the tests in Figure 4.3 were conducted, the samples were permitted to absorb moisture for 4 months under nominal conditions in the laboratory. This time period was used because it resulted in moderate moisture absorption as gauged by the mass increase in the samples which is about 0.9%. Figure 4.4 shows damping ratios of the same samples in Figure 4.3 after this moisture absorption. Damping is seen to increase to nearly the same value in all cases, eliminating the effect of the filler on damping. It is noted that the damping properties of the composites are assumed to be the same after repeated tests because the input of the vibration very small (0.5mm). The effects of the moisture on the mechanical properties of the matrix material in the successive damping tests are ignored.

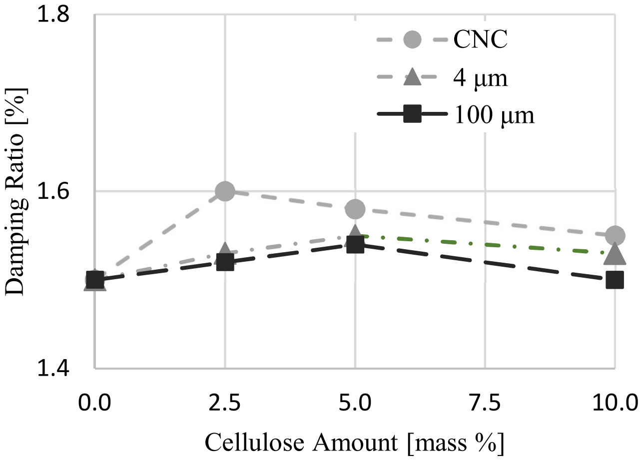

Figure 4.4. Damping tests on the same samples in Fig 4.3 after absorbing moisture for 4 months.

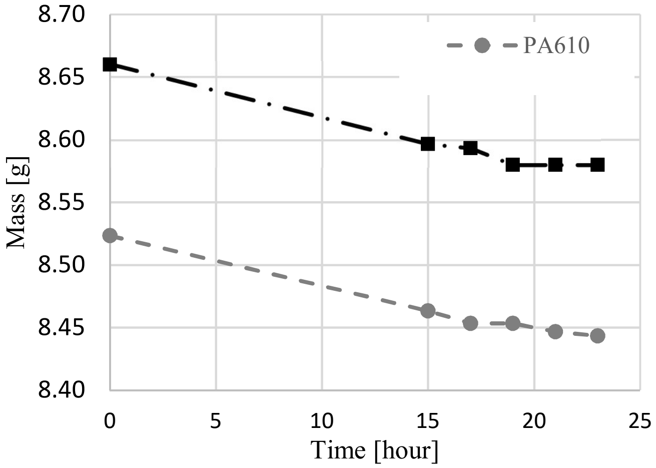

Figure 4.5. Mass loss curves of control PA610 and CNC reinforced PA610 samples.

The effect on damping of successive re-drying was studied using the samples tested in Figures 4.3 and 4.4. Figure 4.5 shows representative drying graphs for control and 5% CNC. After 23 hours, the mass of both samples has decreased by about 0.9%. Over the last 1 hour of the test, the mass of each sample has decreased by an amount less than 0.1% of the starting mass indicating that nearly all moisture has been removed from the sample. Results of damping tests on samples after the first and the second drying/moisture absorption period are shown in Figure 4.6. Drying is seen to progressively decrease the damping capacity of the composites. For example, in the 10% CNC case, the 210% damping increase over the control observed in Figure 4.3 decreases to 44% after 2 successive moisture absorptions/dryings. It should be noted that the damping of unfilled PA610 is essentially unaffected by drying, suggesting that the process of removing moisture by drying effects the interaction of the filler and the matrix carrier.

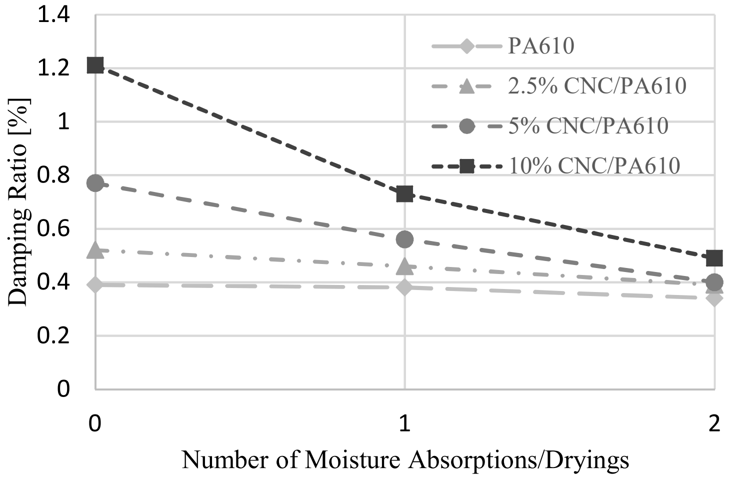

Figure 4.6. Damping ratios of CNC reinforced PA610 samples after successive moisture absorption and drying. On the abscissa axis, 0 denotes samples that have not absorbed moisture; 1 denotes the same samples after absorbing moisture and then undergoing drying; 2 denotes the same samples after absorbing moisture for a second time and then undergoing a second drying.

In the moisture study of Figure 4.4, absorbed moisture is seen to increase the damping of the PA610 control, but further increase in damping beyond this by the fillers is minor for all the composite cases. The filler size effect is diminished. In other polymer composites [111], moisture absorbed by the polymer was found to increase free volume inside the composites, which increases the mobility of the polymer chains, and encourages internal friction between the polymer chains which can increase damping in the moisture containing composites. Additionally, micro-channels form at the interface between the filler and matrix materials when moisture is absorbed [92], disrupting the adhesion of the materials, which may decrease the influence of the fillers by discouraging the intermolecular phenomenon described above.

In the re-drying study of Figure 4.6, damping improvement over the control caused by the fillers diminishes when the samples are dried after moisture absorption. The most pronounced case is that of 10% CNC in which the damping ratio is seen to decrease by over 50% after 2 re-drying processes, while the damping ratio of the control PA610 decreases by less than 13%. Interfacial friction [268] and adhesion can be strongly related to hydrogen bonding between the contacting surfaces [267] and may play a role in energy dissipation, as described above. Interfacial separation distance between filler and matrix increases when the composite absorbs moisture and is dried [92]. A possible result of increased interfacial distance in the present study is weakening of the hydrogen bonding at the interface between PA610 and cellulose, which could lead to reduced damping effect induced by the PA610/CNC interaction.

4.3.3 Effects of Temperature

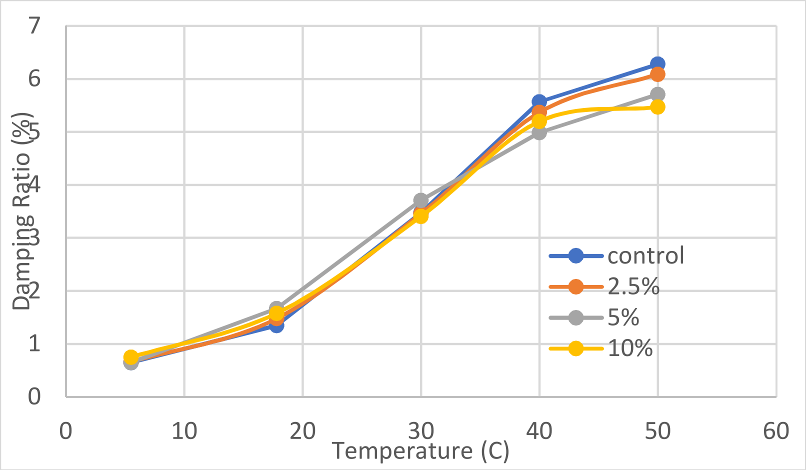

Figure 4.7. Damping ratios of CNC reinforced PA610 samples at different temperatures. The samples are the same samples in Fig 4.3 after absorbing moisture for 4 months.

In Figure 4.7, CNC-reinforced PA610 shows an increasing trend of damping ratio with the increase in temperature. When the temperature is lower than 30 ˚C, the damping ratio difference between the three mass fractions of CNC-filled PA610 is minor, especially at 5.5 ˚C. Even though the damping increase is negligible in this range, 5% CNC still exhibits the greatest damping improvement among all three mass fractions of the filler. However, there is a transient point at 34 ˚C at which control PA610 starts to prevail. It also shows that the addition of CNC filler decreases the damping ratio of the composites when the temperature is higher than 40 ˚C. The reason for these behaviors is believed to be that viscoelastic properties are significantly influenced by the matrix material when it approaches the glass transition temperature of PA610 (44 ˚C) [269].

4.4 Results for Cellulose/PP Composites

4.4.1 Dry Samples

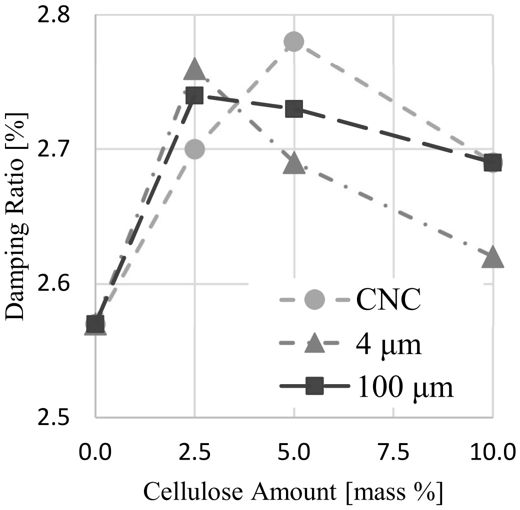

Figure 4.8. Damping tests on cellulose reinforced polypropylene composites.

Figure 4.8 shows damping test results for polypropylene reinforced by micro- and nanocellulose. Because PP is a hydrophobic material, samples will remain in dry condition, so no comparisons are made of moisture-containing versus dry samples. Here, the filler is seen to have minor effect on the damping of PP.

In Figure 4.8, the addition of cellulose to polypropylene increases the damping ratio, though the effect is minor compared to the PA610/cellulose cases (Figure 4.3). This is due to two factors. Firstly, the base damping of polypropylene is 6.6 times greater than PA610, offering less opportunity for damping improvement by the filler. Secondly, though interfacial hydrogen bonds in these PP/cellulose composites do occur (due to the coupling agent), their number is very low compared to PA610/cellulose, reducing the dissipative effect due to sudden intermolecular distance changes.

4.4.2 Effects of Temperature

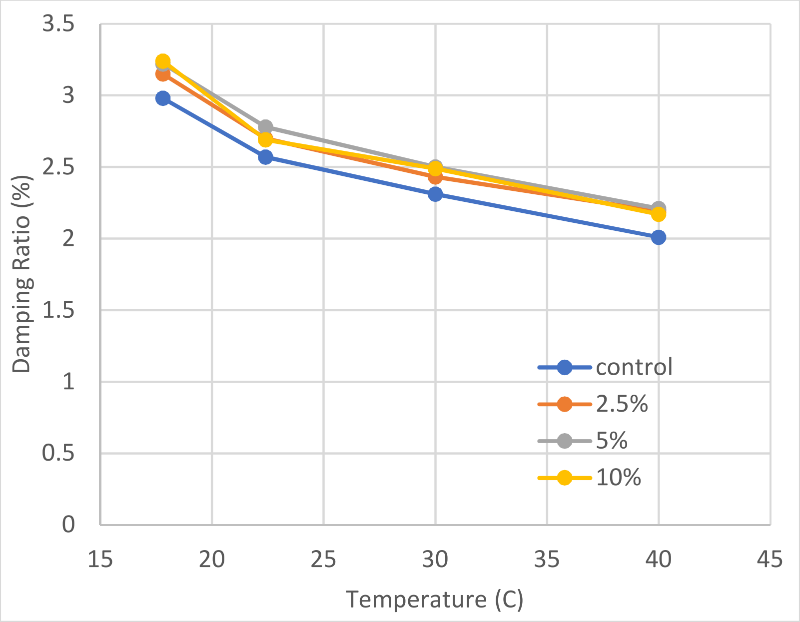

Figure 4.9. Damping ratios of CNC reinforced PA610 samples at different temperatures.

Figure 4.9 presents the decreasing trend in the damping ratios of CNC-reinforced PP composites when the temperature increases from 17.8 ˚C to 40 ˚C. This decreasing trend comes from the damping ratio of PP peaking at its glass transition temperature, which is around -10 ˚C [270]. It can be seen that the addition of CNC improves the damping of PP at every temperature point in the graph. Meanwhile, the mass fraction of the filler negligibly affects the damping ratio of the composites as the temperature increases.

4.5 Conclusion

Overall, CNC was found to produce only a 3.6% increase in modulus of PA610, while micro-scale cellulose increases the modulus by up to 22%, in the composites created in this study. However, CNC substantially increases the damping (by 210%) of PA610, a polymer possessing low native damping. Larger cellulose fillers also increase damping, but to a lesser extent than does CNC (by 100% in the 4 μm case and 67% in the 100 μm case). Factors influencing damping in these composites appear to be high specific surface area and the presence of substantial hydrogen bonding between the filler and the matrix material at their interface. The features resulting in high damping in these composites offer promising options for introducing damping into other low-damping polymers. Moisture absorption of PA610/cellulose composites increases the base damping of the matrix material and diminishes the effect of the cellulose fillers on damping. After moisture is driven from the composites, the high measured damping produced by the cellulose fillers in the initially dry case was found to not be recoverable.

Chapter 5 Microscopic Observations and Analysis

Ms. Elise Kowalski conducted the microscopy reported in this section. The main purpose of the microscopy is studying the morphology of the filler particles. In addition. The status of the bonding between the filler and matrix materials can be investigated. Scanning electron microscopy (SEM) is used in this study.

5.1 Microscopy Experiment Setting up

A Raman imaging and scanning electron (TESCAN RISE) microscope is used to analyze the tensile fracture surfaces of all three types of PA610/micro- and nanocellulose composites. To increase topographical contrast, each specimen is individually mounted on an SEM stub with conductive copper tape nearly touching the fracture surface and then gold-coated with a sputter coater. Images are acquired at multiple magnifications using secondary electron detection with an accelerating voltage of 5.0 kilovolts and a beam intensity of 5.00.

5.2 Results and Discussions

Figure 5.1 shows two types of fracture surfaces. The majority of the area on the left is a honeycomb-shaped surface that is stretched under a tensile load, indicating ductile behavior. The surface area in the right side of the image is flat and smoother, indicating brittle behavior. The brittle fracture surface suggests that cracks formed and propagated in this region. The distribution of CNC particles is uniform across the majority of the ductile fracture area. However, the particles are not clearly observed in the brittle fracture region.

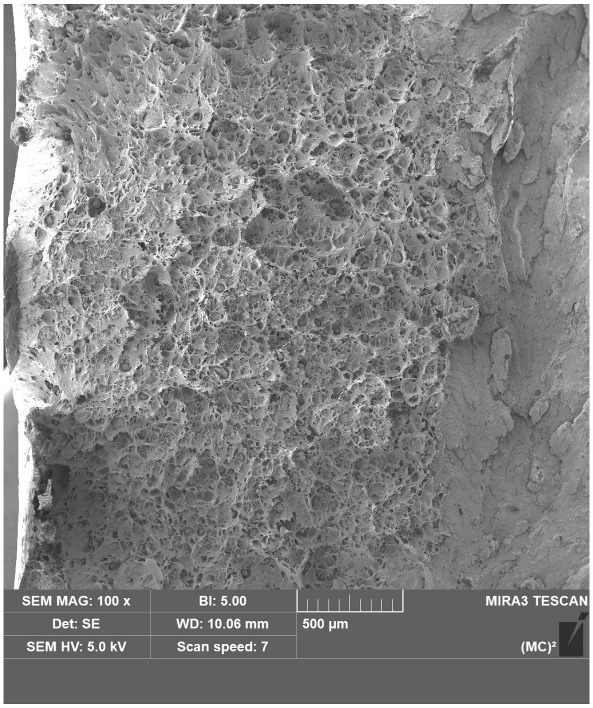

Figure 5.1. Fracture surface of 2.5% CNC-reinforced PA610 at magnification 100 x.

As shown in figure 5.2, there is a debonding surface between the CNC particles and PA610 located in the bottom of the cavity. In contrast with the smooth wall of the cavity, the thin fin-shaped residue at the bottom surface indicates that the interfacial region of the filler and matrix material experienced a strong tensile load and failed. Meanwhile, the deformed residue of PA610 on the failure surface shows that there is good bonding between the CNC particles and the PA610.

Figure 5.3 shows a CNC particle attached to the fracture surface. A black mark appears on the particle surface. It is believed that the mark is created by the inconsistent thickness of the gold coating during surface treatment before SEM. Plastic deformation of the matrix material can be seen at the bonding area underneath the particle, which indicates good bonding between the filler and matrix material under substantial tensile loading.

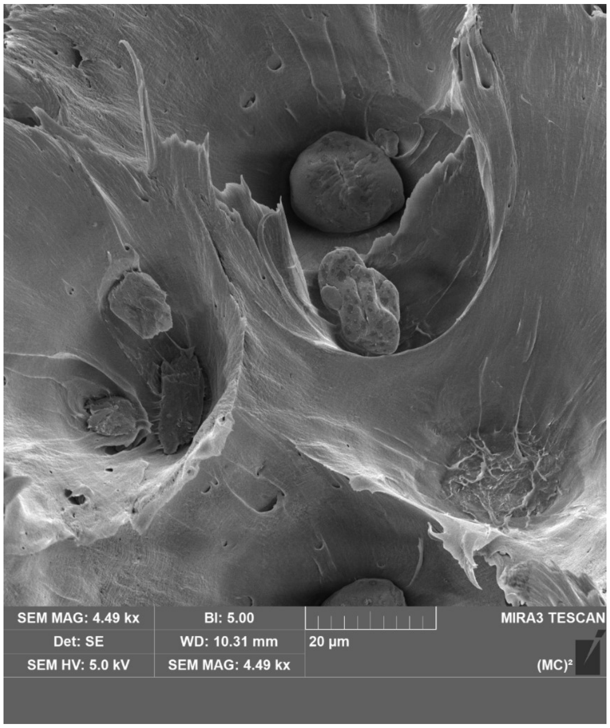

Figure 5.2. Fracture surface of 2.5% CNC-reinforced PA610 at magnification 4.49 kx.

Figure 5.3. Fracture surface of 5% CNC-reinforced PA610 at magnification 23.3 x.

Figure 5.4 shows that a CNC particle is still attached with the matrix PA610 after the failure in the tensile tests. Due to the longest dimension of the particle not being along the direction of the loading, the tensile force does not transfer from the matrix material to the particle efficiently. This results in stress concentration in the matrix material and could lead to debonding issues. In addition, the small particles distributed on the surface are thought to be the residue of the fractured matrix material.

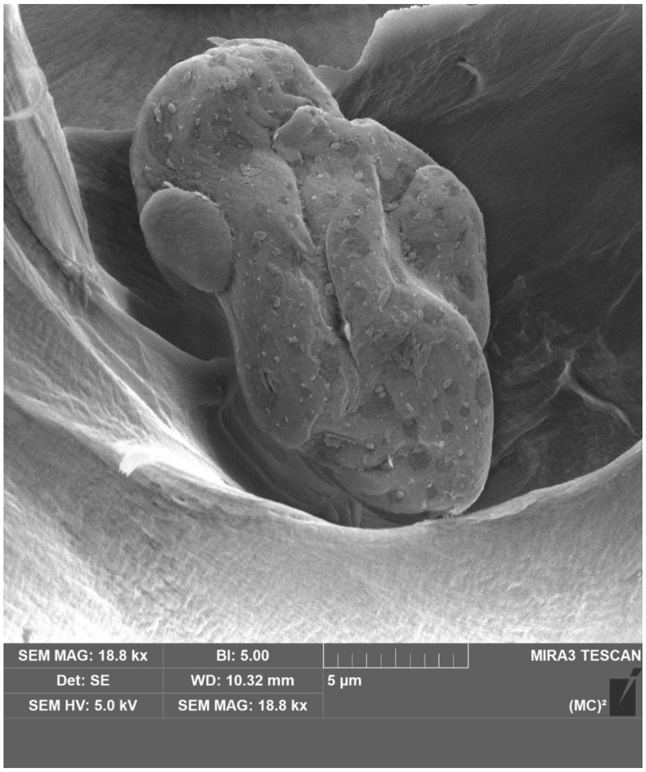

Figure 5.4. Fracture surface of 2.5% CNC-reinforced PA610 at magnification 18.8 x.

The morphologies of three different sizes of micro- and nanocellulose-reinforced PA610 are shown in Figure 5.5. All three images are at the same magnification. Cellulose in these images appears as small particles embedded in cavities. The protruded striations of PA610 in all three images are indicative of ductile behavior of the polymer. Similar low strain-rate behavior was observed in [271] for polypropylene natural fiber composites. In Figure 5.5(a), the largest particle is approximately 40 μm, indicating that some agglomeration has taken place either before or during the manufacturing. Additionally, the CNC particles are seen to be uniformly distributed over the fracture area, indicating a well-manufactured sample. As in the CNC case, the 4 µm case in Figure 5.5(b) shows some agglomeration, with sizes ranging from about 10 to 100 µm. The longer striations of PA610 around the cavities containing the agglomerated fibers in Figure 5.5(b) compared to Figure 5.5(a) indicate that the material experienced increased tensile stress around the agglomerations. Figure 5.5(c) shows good distribution of the particles. The average particle size is within the manufacturer's specified size range for this fiber case, 100 µm; thus, the fibers did not significantly agglomerate. The lack of substantial agglomeration in the 100 µm case is due to its small surface area per unit mass and weak attractive interaction between particles, which inhibit agglomeration [272, 273].

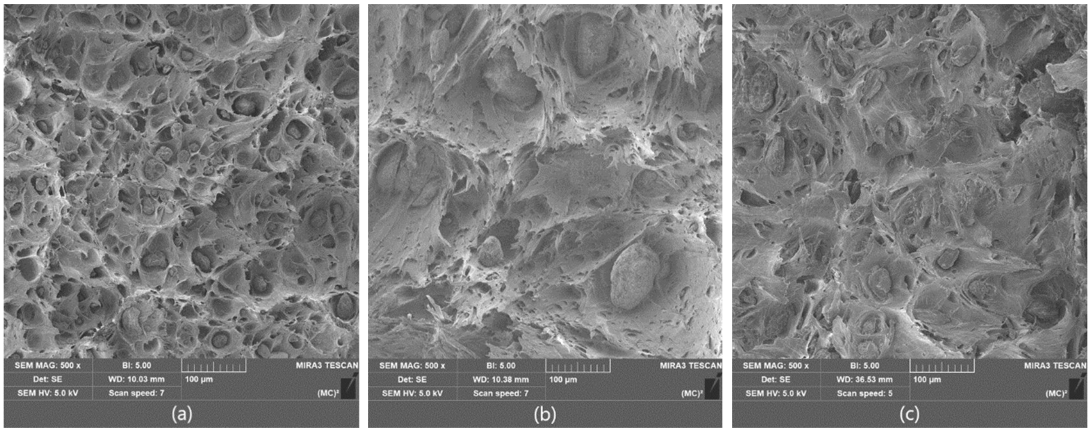

Figure 5.5. SEM images of tensile test fracture surfaces of PA610 reinforced with 5% mass ratio of: (a) CNC, (b) 4 µm cellulose fiber, (c) 100 µm cellulose fiber.

Chapter 6 Modeling

The modeling section presents the models developed for studying the potential mechanisms of damping increase in CNC/PA610 composites. Interfacial interaction at nano scale is believed to be the cause of the damping improvement. Therefore, the models focus more on intermolecular forces at the interfaces between fillers and matrix materials.

6.1 Two-masses Model

6.1.1 Overview

This model is proposed to investigate the interaction between two particles at the molecular level. This is an essential step for studying the potential behavior of intermolecular interaction in the composites. It may help to explain the origin of the great damping improvement in PA610/CNC composites, as shown in the graph 6.1. Two masses represent two particles at the molecular level. An intermolecular force called the Van der Waals force [274], which is widely known as a common intermolecular force, is exerted between the masses. The motion of the masses is constrained in one dimension, and there is no friction or viscous environment applied to the model. The system is excited by a small input applied to one of the masses. The motion of the system is simulated in MATLAB.

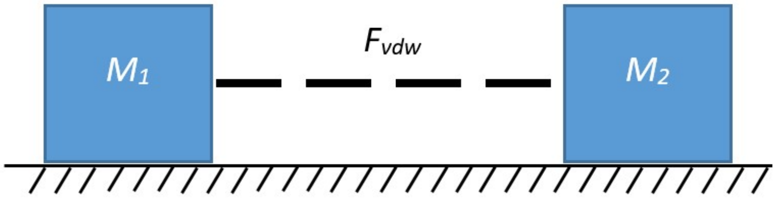

Figure 6.1. Schematic of the two masses model.

The Van der Waals force in the model uses the famous Lennard Jones potential [275], as shown in the equation below.

$$P_{vdw}(r) = 4\varepsilon[\left(\frac{\sigma}{r}\right)^{12} - \left(\frac{\sigma}{r}\right)^{6}] \tag{6.1}$$

P_{vdw} is the Lennard Jones potential between the particles. r is the distance between two interacting particles. ε is the depth of the potential well. It refers to the minimum potential energy. σ is the intermolecular distance when the potential energy is zero. The force function can be derived from the equation (6.1).

$$F_{vdw}(r) = -\frac{\partial P_{vdw}}{\partial r} = \frac{4\varepsilon}{\sigma}[-12\left(\frac{\sigma}{r}\right)^{13} + 6\left(\frac{\sigma}{r}\right)^{7}] \tag{6.2}$$

Assuming that the positions of the first and second mass are x_1, x_2, the governing equation of motion is given as:

$$M_1\ddot{x}_1 - \frac{4\varepsilon}{\sigma}\left[12\left(\frac{\sigma}{r}\right)^{13} - 6\left(\frac{\sigma}{r}\right)^{7}\right] = 0 \tag{6.3}$$

$$M_2\ddot{x}_2 + \frac{4\varepsilon}{\sigma}\left[12\left(\frac{\sigma}{r}\right)^{13} - 6\left(\frac{\sigma}{r}\right)^{7}\right] = 0 \tag{6.4}$$

$$r = x_2 - x_1 \tag{6.5}$$

M_1 and M_2 are the mass of the particles. The values of the constants used in the model are presented in the following Table 6.1.

Table 6.1. Parameters of the Two-masses Model

Constant	M_1	M_2	ε	σ
Value	1.6 e^{-11} kg	1.6 e^{-11} kg	0.29288 ev	0.35636 nm

6.1.2 Results and Discussions

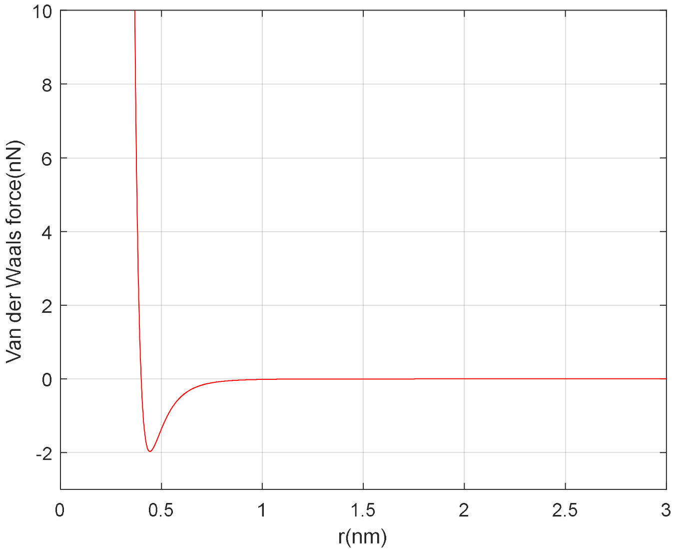

Figure 6.2. Curve of Lennard Jones force vs intermolecular distance.

The relationship of the Lennard Jones force and the intermolecular force is shown in Figure 6.2. The force curve has a portion where the gradient is high. This part starts from 0 and ends at the point of the minimum value, which is approximately at 0.4 nm in the graph. Because of the high slope of the curve, it shows a great repelling force increase exerted to each interacting particle in a very short distance. Note that the repelling force shows positive value in the graph. In this portion of the curve, there is a point where the force is zero. The distance of this point is the equilibrium distance between the particles. When the intermolecular distance is larger than that of the point of the minimum force, the attraction force between particles begins to dominate the behavior of the curve. The force in this part remains attractive. However, it be seen that the magnitude of the force gradually approaches zero as the intermolecular distance increases. This phenomenon is common at the molecular level. The intermolecular force can be viewed as a "bond" break after the molecules depart from each other at a certain distance.

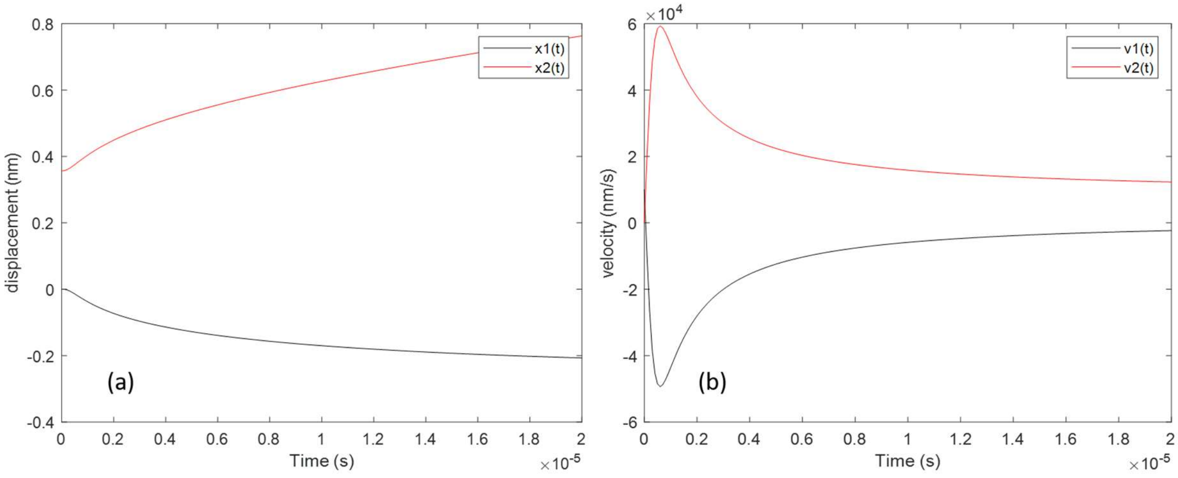

Figure 6.3. (a) Displacement and (b) velocity of the two masses vs time. An initial velocity is given to one of the masses.

The initial distance between the masses is 0.35636 nm. This is the value when the intermolecular force is zero. The initial velocities of the first mass and the second mass are 10000 nm/s and 0 nm/s. The displacement and velocity of the masses are presented in the Figure 6.3 above. The masses are approaching because of the initial velocity of the first mass. However, a strong repelling force begins to dominate the motion in this process, and this occurs very quickly right after the simulation starts. It can be seen that the masses start to depart from each other. Meanwhile, the displacement of the second mass is larger than that of the first one. The velocity graph of the masses shows the interesting result that each velocity has a maximum peak and they both occur at the same time. The peak and final velocities of the first mass are lower than those of the second mass. This also explains why the displacement of the second mass is larger. The majority of the initial kinetic energy of the first mass transfers to the second mass. Due to the intermolecular distance increase to approximately 1 nm at the end of the simulation, the attraction force is too small to affect the motion. It can be seen that the slope of the velocity becomes flat, which indicates that the interaction of the particle vanishes in the end.

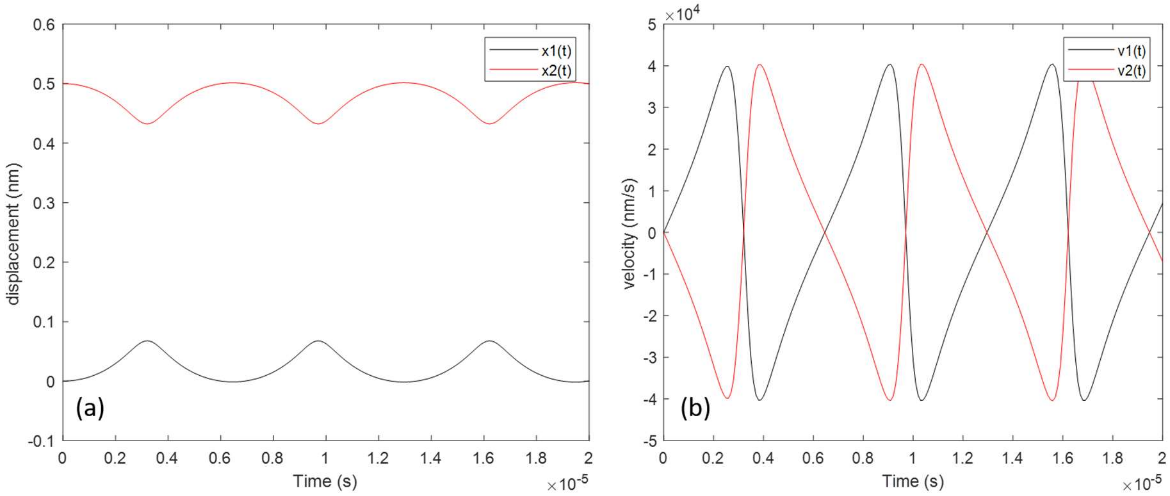

Figure 6.4. Displacement and velocity of the two masses. An initial displacement is given to one of the masses.

The Figure 6.4 presents the displacement and velocity of the mass under the condition of the given initial displacement. The distance between the two masses changes from 0.35636 nm to 0.5 nm. The initial velocity of the masses is set to zero. The displacement and velocity curves show periodic patterns. In the displacement graph, the amplitude of the curves of the masses is the same. The first mass reaches the maximum displacement when the second mass becomes minimum and vice versa. This is very similar to the behavior of a simple mass-spring system. However, the intermolecular force is highly nonlinear. The curve is no longer sinusoidal. The velocity graph illustrates similar periodic behavior. It can be seen that there is one maximum and minimum point in each cycle and that their amplitudes are the same. Meanwhile. The first mass accelerates the same amount as the second mass accelerates in the opposite direction.

6.1.3 Conclusion

The two-masses model is a simplified molecular model. By introducing Lennard Jones potential, the intermolecular interaction between particles is investigated from the motion of the masses. It clearly shows how energy is transferred between particles. Lennard Jones potential gives interesting motion of the mass, especially in the case of the given initial velocity of the first mass. The masses depart from each other in the end rather than moving in a periodic pattern. This potentially provides explanation of debonding or crack formation between the fiber and matrix material in composites. In addition to the difference that is made by Lennard Jones potential, similarities to common mass-spring systems can also be seen in this model. The masses move periodically when one of the masses is loaded by the given initial displacement, although this model is coarse. Only two particles are considered and heat transfer is neglected. It is worthy to be a first step to study the intermolecular interaction. Besides, the two-masses model is a conservative system. Studying the hidden mechanism of the great damping improvement in the CNC/PA610 composites requires means of energy dissipation. More effort needs to be taken to implement energy dissipation in the model.

6.2 Friction Model

6.2.1 Friction Model Overview

The damping improvement of PA610 matrix material in addition to CNC indicates the importance of the filler effect. The interaction between the filler and matrix may play an essential role in damping enhancement at the contacting surfaces. Friction provides a potential source of energy dissipation at the molecular level. Frictional sliding may occur at the interfacial area between the filler and matrix material under loading. Therefore, a model based on the interfacial frictional sliding [248] is built to study the mechanism of the damping increase.

This friction model is proposed based the study [251]. In Figure 6.5, the model is composed of two contacting surfaces at a certain distance. They can be viewed as the interfaces of the filler and matrix material. The bottom surface is fixed while the top one is pulled by a spring in a horizontal direction. This structure is similar to a probe that measures the friction when the top surface slides [276]. There are many intermolecular bonds connected between the contacting surfaces. As the top surface moves, the intermolecular bonds form and rupture spontaneously. The frictional force can be calculated in the equation (6.6). MATLAB is used to conduct the simulation.

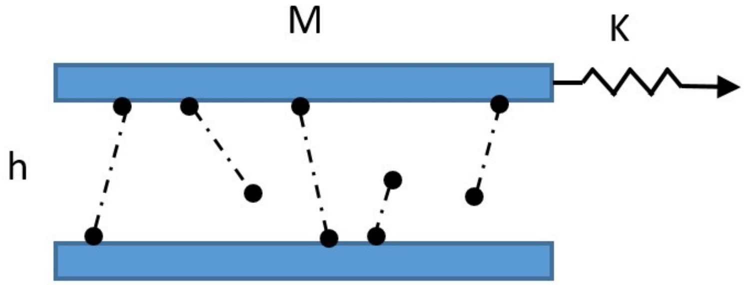

Figure 6.5. Schematic of the friction model.

The equation of motion of the model is given as:

$$M\ddot{X} + \eta\dot{X} + F_b + K(X - Vt) = 0 \tag{6.6}$$

M is the mass of the top plate. X is the coordinate of the center of the mass. η is the damping coefficient of the system. F_b is the total force of the intermolecular bonding between the surfaces. K is the spring constant of the linear spring that is connected to the top plate. V is the velocity of the one end of the spring that is pulled by a loading. The elongation of the spring is calculated by $X - Vt$. The friction force is the sum of damping force $\eta\dot{X}$ and intermolecular force F_b. The intermolecular force F_b is shown as the equation below:

$$F_b = \sum_{i=1}^{N} q_i f_i^{(x)} \tag{6.7}$$

q_i represents the state of the bonds. The bonds are intact when $q_i = 1$. When the bonds break during the top plate sliding, $q_i = 0$. $f_i^{(x)}$ is the projection of the intermolecular force to the horizontal direction, which is explained in the following equations:

$$f_i^{(x)} = f_i x_i / l_i \tag{6.8}$$

$$f_i = k(l_i - l_0) \tag{6.9}$$

$$l_i = (x_i^2 + h^2)^{1/2} \tag{6.10}$$

x_i is the projection of the bond length in horizontal direction. l_i is the length of the intermolecular bond. For simplicity, the intermolecular force f_i is modeled as a linear spring with a spring constant k. The elongation of the bond is calculated by $l_i - l_0$, where l_0 is the initial length of the intermolecular bond. The current bond length is calculated by equation (6.10), in which h is the distance between the top and bottom surfaces. The two different states of bonds determine the dynamics of the model. For the bonds connected to both surfaces, the velocity of the moving end of the bonds equals the velocity of the top plate. So $\dot{x} = \dot{X}$. The bonds that are ruptured during the top plate movement take some time to relax and be restored to their original length. Thus, the relation between the velocity of the top plate and the connecting points of the bonds is:

$$\dot{x}_i = q_i \dot{X}_i - \lambda(1 - q_i)x_i \tag{6.11}$$

λ is the relaxation constant characterizing the rate of the ruptured bonds' return to the original length. To determine the state of each intermolecular bond, an equation defines the time dependence of the state of each bond, shown as:

$$q_i(t+\mathit{\Delta} t) = q_i(t) - q_i(t)\theta\left(\xi_i - \Delta t k_{off}\right) + [1-q_i(t)]\theta(\xi_i - \Delta t k_{on}) \tag{6.12}$$

$\mathit{\Delta} t$ is the time step of the model. ξ_i is a random variable, which is selected from 0 to 1. $\theta(z)$ is Heaviside step function, which determines the stochastic reforming and rupture process of the bonds. The rates of bond reforming and rupture are dependent on k_{on} and k_{off}. The equation for the rates of bond dissociation has two forms, for strong and weak bonds. For the weak bonds [223] whose energy is less than K_bT, it is written as:

$$k_{off}(l_i) = k_0\exp(\beta f_i \Delta x) \tag{6.13}$$

For the strong bonds[277], the equation is given as:

$$k_{off}(l_i) = k_0\left(1-\frac{f_i}{f_c}\right)^{\frac{1}{2}} \exp[-\beta\left[U_0\left(1-\frac{f_i}{f_c}\right)^{\frac{3}{2}} - U_0\right]] \tag{6.14}$$

k_0 is the rate of bond spontaneous dissociation without external load. Δx is the distance at the interval of the maximum and minimum reaction potential. f_c is the force when the unbinding occurs without thermal fluctuation. U_0 is the depth of potential. β represents $1/k_BT$ in both equations.

The bond reforming rate is considered to be associated with the bond age [278] rather than the load or the elongation. The bond age is defined as the time starting from the exposure of the free ends of the bonds to the environment after the bonds ruptured.

$$k_{on} = k_{on}^0\, \mathrm{g}[(\tau - \tau_0)/\Delta t] \tag{6.15}$$

$$\mathrm{g} = \begin{cases} 0\ (\tau \ll \tau_0) \\ 1\ (\tau > \tau_0) \end{cases} \tag{6.16}$$

$$\tau = a/\dot{X} \tag{6.17}$$

$$V_0 = a/\tau_0 \tag{6.18}$$

k_{on}^0 is the reforming rate for the bonds when the top surface is fixed. In equation (6.14), g is a “smeared” step function. a is a typical length scale of surface contact. V_0 is the critical velocity of the moving surface. The reforming rate will be unstable when the velocity is above V_0.

The values for the parameters in the simulation are shown in the following table.

Table 6.2. Parameters for the friction model

parameters	value	unit
$\boldsymbol{M}$	1	$10^{-22}kg$
$\boldsymbol{\eta}$	0.25	$10^{-22}kg/s$
$\boldsymbol{K}$	10	$10^{-22}kg/s^2$
$\boldsymbol{V}$	2	nm/s
$\boldsymbol{h}$	1	nm
$\boldsymbol{\lambda}$	2	s^{-1}
$\boldsymbol{l_0}$	1	nm
$\boldsymbol{k}$	10	$10^{-22}kg/s^2$
$\boldsymbol{T}$	293	K
$\boldsymbol{k_b}$	1.38×10^{17}	$10^{-40}J/K$
$\boldsymbol{\Delta x}$	1	nm
$\boldsymbol{k_o}$	10	s^{-1}
$\boldsymbol{k_{on}^0}$	100	s^{-1}
$\boldsymbol{a}$	1.5	nm
$\boldsymbol{V_o}$	0.5	nm/s
$\boldsymbol{\Delta t}$	0.01	s
Note that the values are based on the study [251].		

6.2.2 Results and Discussions

It can be seen from the Figure 6.6 that the top plate is moving approximately 2 m/s at the end of the simulation, which corresponds to the velocity of the pulling spring. This also shows that the forces exerted on the top plate are almost balanced. However, there is some oscillation of the velocity curve in the beginning. The reason for this oscillation is believed to be the instability of the bonds' dissociation and reforming. For the displacement of the bonds, it can be seen that the displacement of two typical bonds increases from zero to 0.5 nm and becomes steady after 5 seconds. This corresponds to the oscillation of the velocity of the top plate as well. The shape of the curves indicates that frequent bond rupture and reforming occurs during the simulation.

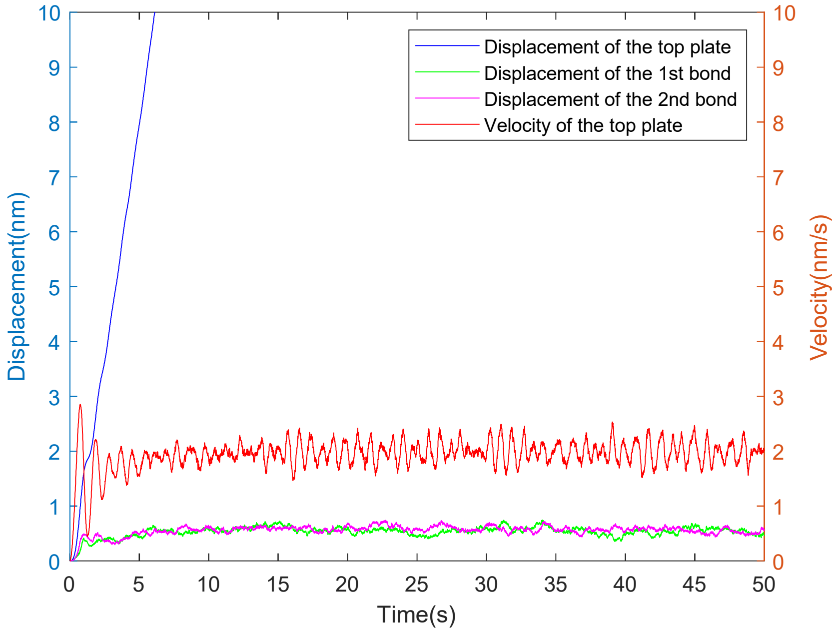

Figure 6.6. Displacement and velocity of the top plate and the displacement of the ends of the first, second bond over time.

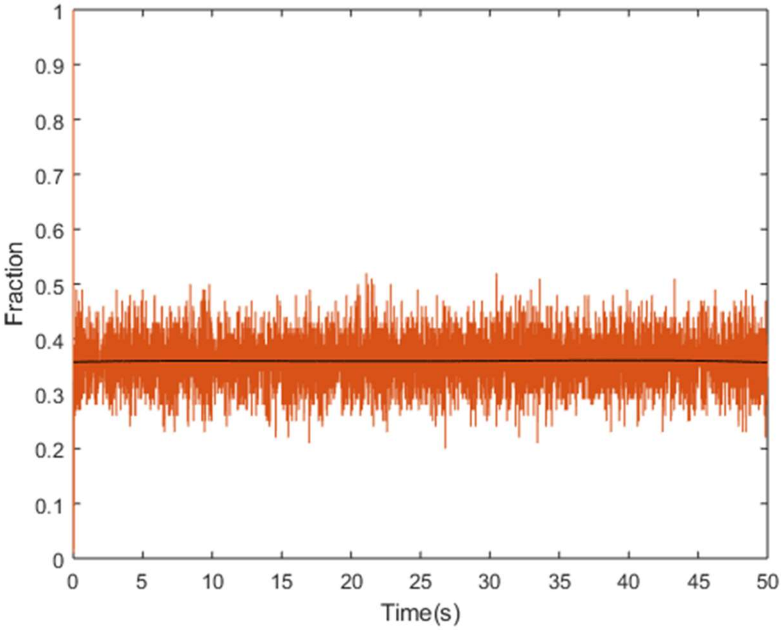

Figure 6.7. Fraction of the intact bonds over the total bonds. Note that the black line represents the average values of the red curve.

Figure 6.7 shows the trend of the status change of the bonds. It can be seen that the bonds are all intact initially. At the beginning of the top plate's movement, most of the bonds break suddenly because of excessive stretch. Then some of the bonds reform over time. The continuous bond dissociation and reforming reach a balanced state until the end of the simulation. The fraction of the intact bonds over the total bonds becomes steady at around 0.36.

Figure 6.8 shows the change of spring force and friction force. These two forces are critical in determining the behavior of the top plate. The two curves present similar trends in that they both start from zero, increase, and become steady after 10 seconds. The average values of both forces are at approximately the same level. This means that the majority of the spring force is balanced by the friction force. The minority is balanced by the damping force. It can also be seen that the amplitude of the oscillation in the friction force curve is much larger than that of the spring force. Because of the inertia of the top plate, frequent change of the friction force has minor influence on the displacement of the plate. The spring force related to the displacement of the plate and the pulling end is slightly affected by the friction force.

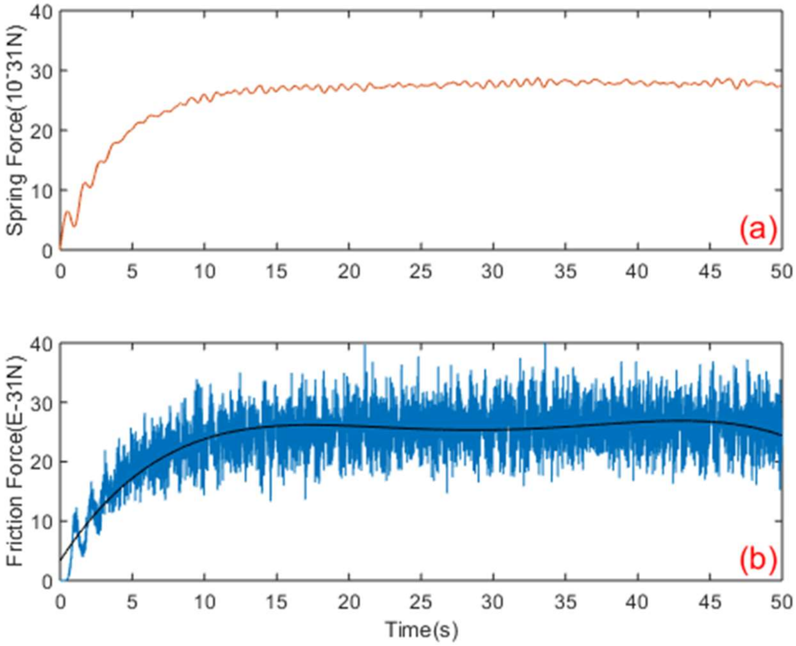

Figure 6.8. (a) Spring force and (b) friction force vs time. Note that the black line represents the average values of the blue curve.

6.2.3 Effects of the Mass of the Contacting Surface

Some parameters of the model are changed to study their effect. As shown in Figure 6.9, the mass of the top plate is doubled. Compared to the case in Figure 6.6, the velocity of the top plate does not converge in the end. Meanwhile, the amplitude of the oscillation is much greater than that in Figure 6.6. The stretch of the first and second bonds increases with time. In Figure 6.7, the fraction of the intact bonds maintains the same trend as in the first 10 seconds. However, it keeps decreasing after 10 seconds, which indicates the imbalance of the bond rupture and reforming related to excessive stretch of the bonds. It is believed that the frequent change of the top plate velocity is the reason for this phenomenon. Contrary to the case in Figure 6.8, the spring force in Figure 6.11 increases with time. This indicates that the velocity of the top plate is decreasing, which results in the stretch of the spring. The trend of the friction force is similar to that of the fraction of the intact bonds.

The results show that the model is highly sensitive to the mass of the top plate. Due to the damping coefficient of the system being small, the main contribution of the energy dissipation is the friction force. The decreasing trend of the friction force indicates that the energy dissipation in the system decreases over time. When the energy dissipation per unit mass is considered, it can be seen that less energy dissipates from the system with larger mass. Note that this is the case of the same displacement of the top plate. This result may help to explain the nano effect aspect of energy dissipation. It corresponds to the results in the damping tests of cellulose-reinforced PA610. CNC has highest damping improvement compared with larger-sized cellulose.

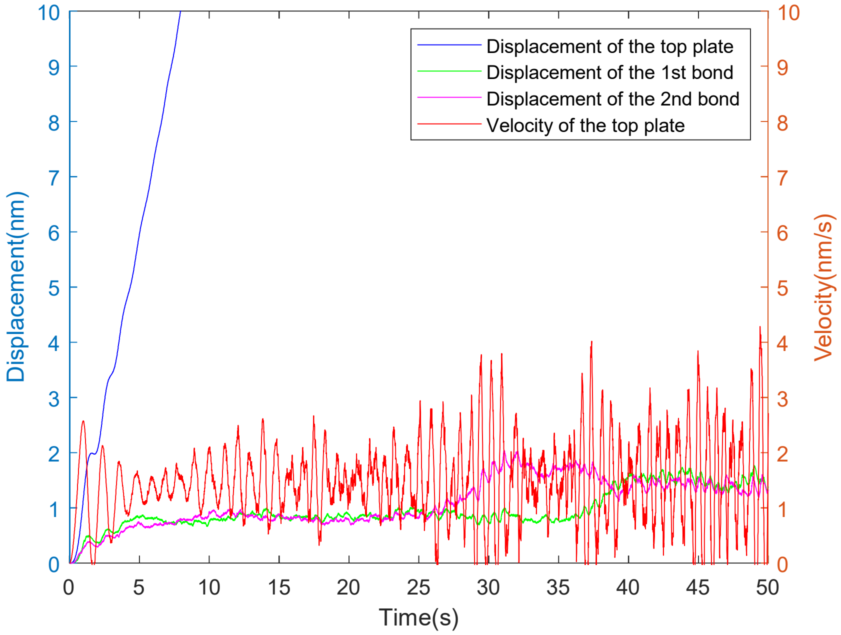

Figure 6.9. Displacement and velocity of the top plate and the displacement of the ends of the first, second bond over time (The mass of the top plate is doubled).

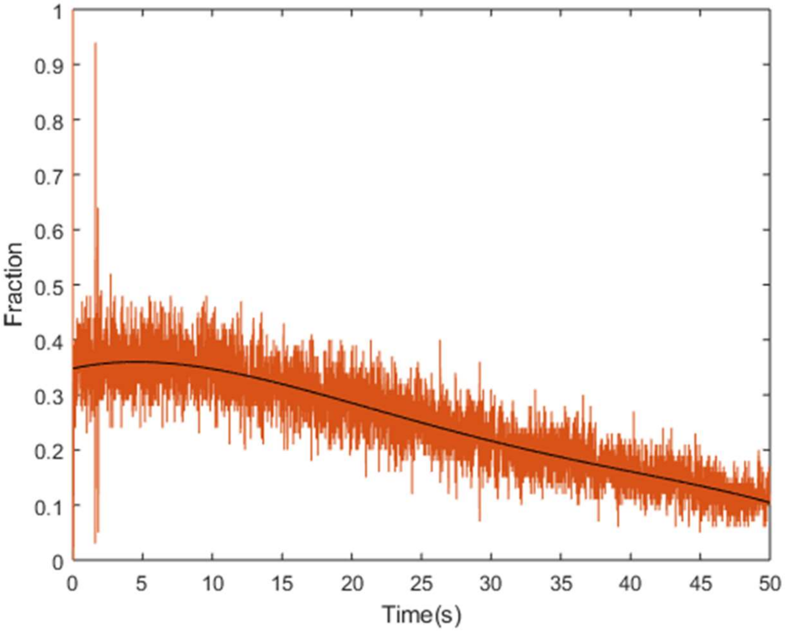

Figure 6.10. Fraction of the intact bonds over the total bonds (The mass of the top plate is doubled). Note that the black line represents the average values of the red curve.

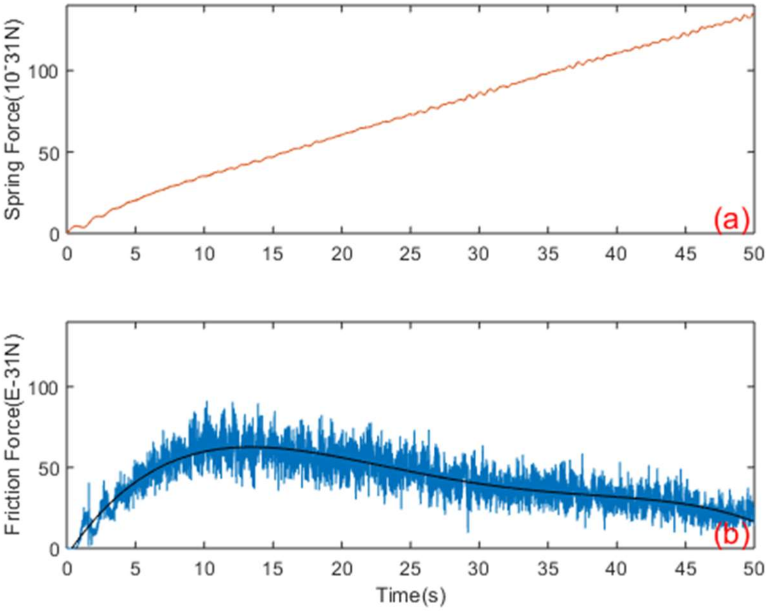

Figure 6.11. (a) Spring force and (b) friction force vs time (The mass of the top plate is doubled). Note that the black line represents the average values of the blue curve.

6.2.4 Effects of the Sliding Velocity

The sliding velocity of the top plate is found to have great influence on the friction force [268]. The velocity of the pulling end of the spring is set to 0.5 nm/s to study the behavior of the model.

As shown in Figure 6.12, the velocity of the top plate becomes steady at 0.5 nm/s, which is approximately same as the velocity of the pulling end of the spring. The displacement of the plate and the ends of the bonds is smaller due to the decrease of the velocity, compared to the control case in Figure 6.6. However, the fraction of the intact bonds remains the same as that in Figure 6.7. This indicates that the velocity of the top plate does not affect the dissociation and reforming status of the bonds. The value of the spring force in the steady state is 47 times smaller than that in Figure 6.8. It is also interesting that the spring force takes a longer time to reach steady state than the control case.

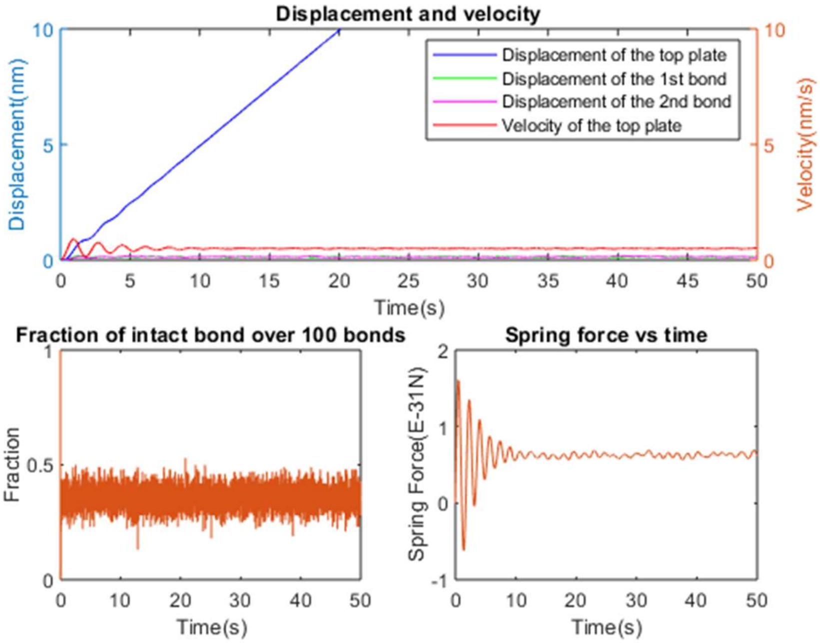

Figure 6.12. Displacement and velocity of the top plate and the displacement of the ends of first, second bond over time (Top figure). Fraction of the intact bonds over the total bonds (bottom left figure). Spring force (bottom left figure). (V = 0.5 nm/s)

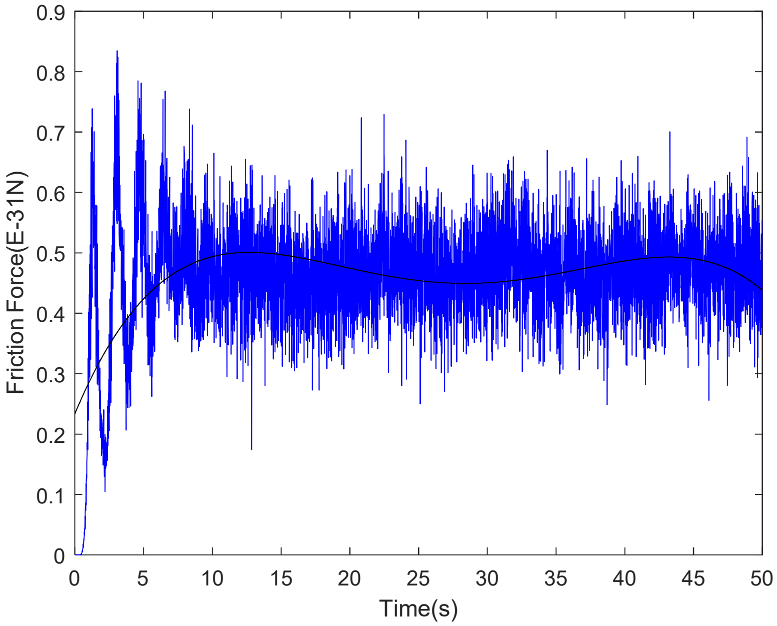

Figure 6.13. Friction force vs time (V = 0.5 nm/s). Note that the black line represents the average values of the blue curve.

In Figure 6.13, due to the oscillation of the top plate velocity, the friction force has a period of oscillation at the beginning. Then it becomes steady at approximately $0.48 \times 10^{-31} N$. This value is about 60 times smaller than that of the control case (V = 2 nm/s). Therefore, the energy dissipation from the system dramatically decreases as the velocity of the top plate changes from 2 nm/s to 0.5 nm/s.

Knowing the case of low pulling velocity, it is necessary to investigate the behavior of the model at a higher velocity. When the velocity of the top plate increases from 2 nm/s to 4 nm/s, the details of the system are shown in the following figures.

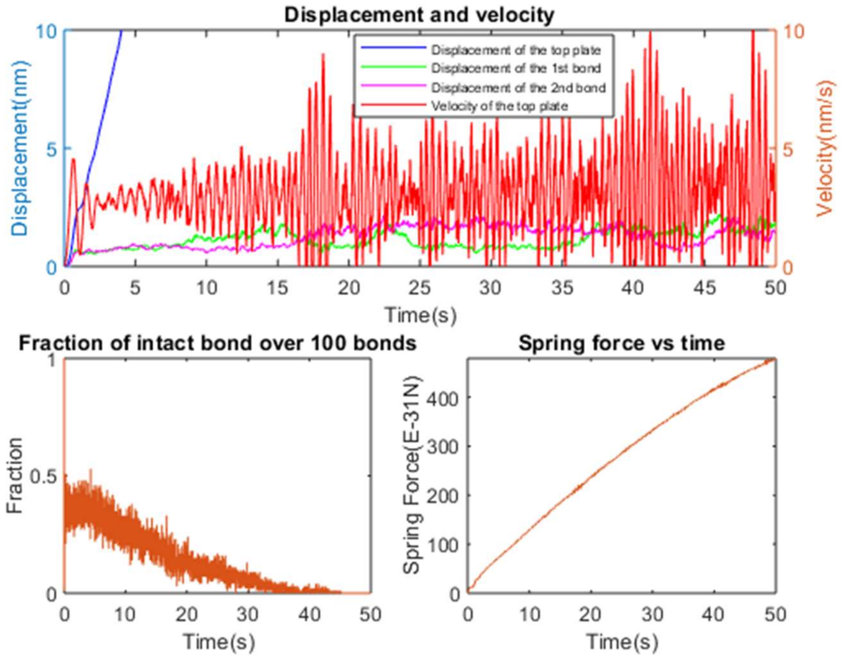

Figure 6.14. Displacement and velocity of the top plate and the displacement of the ends of first, second bond over time (Top figure). Fraction of the intact bonds over the total bonds (bottom left figure). Spring force (bottom left figure). (V = 4 nm/s)

It can be seen in Figure 6.14 that the velocity of the top plate does not converge in the simulation. The displacement of the free end of the bonds increases over time. The fraction curve shows that the bonds continuously break and the rate of bond dissociation is faster than the rate of reforming. Instead of staying at a constant value in Figure 6.8, the spring force increases dramatically. This situation is similar to that in Figure 6.11(a). The frequent change of the velocity causes the imbalance of the bond breakage and reformation.

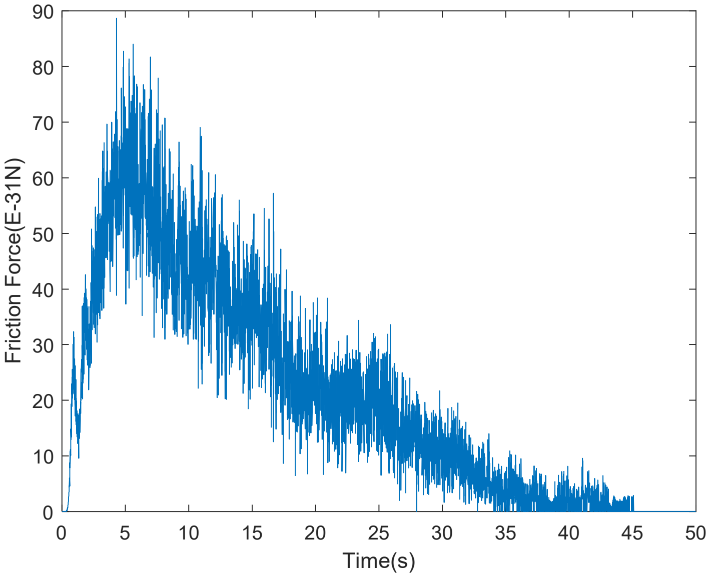

Figure 6.15. Friction force vs time (V = 4 nm/s).

Figure 6.15 shows that the friction force increases with time in the first 5 seconds, when nearly 38% of the bonds are intact. Then it decreases because of continuous fracture of the bonds. These results indicate that the energy dissipation from the friction force is unstable in this system.

Comparing the cases of the three velocities 0.5 nm/s (low), 2 nm/s (medium), and 4 nm/s (high), the friction force in cases of low and medium velocities become stable until the end of the simulation. However, the magnitude of the friction force in the low velocity case is 60 times smaller than the friction force in the high velocity case. The case of high velocity has the highest peak friction force among the three cases, but the friction force gradually decreases to zero over time. It is believed that there is an optimal pulling velocity at which the system obtains maximum energy dissipation. The existence of the optimal pulling velocity can potentially help with the design of materials with good damping properties. It may also inspire people to use the material with proper loading conditions to fulfil the highest damping properties.

6.2.5 Effects of the Bond Dissociation Rate

k_0 is the parameter associated with the bond dissociation rate. This parameter is important in that it influences the number of the contacting bonds between the surfaces. In the following simulations, the value of k_0 increases from 10 to 50 and 80. The results are shown below.

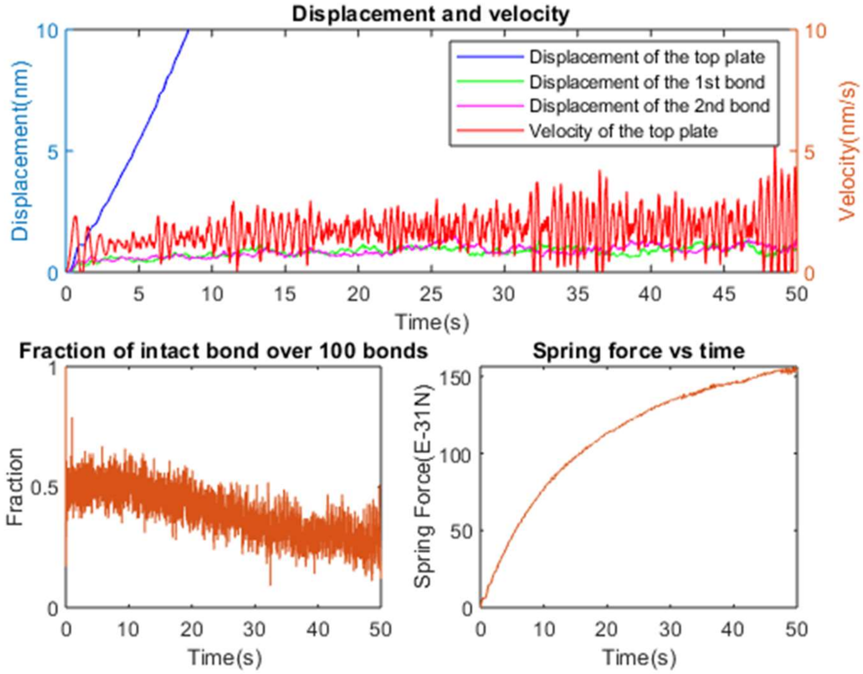

Figure 6.16. Displacement and velocity of the top plate and the displacement of the ends of first, second bond over time (Top figure). Fraction of the intact bonds over the total bonds (bottom left figure). Spring force (bottom left figure). ($k_0 = 50$)

It can be seen from the Figure 6.16 that there is increasing amplitude of oscillation in the velocity of the top plate. The displacement of the ends of the bonds increases from zero and becomes stable at 1 nm. The fraction of the intact bonds shows a decreasing trend from 0.5 to 0.3. Compared to the case in Figure 6.8(a), the spring force continuously increases where the slope of the curve has a decreasing trend. In Figure 6.17, the friction force peaks at 17 seconds.

The maximum value is $82 \times 10^{-31} N$. It can be seen that the friction force at the end of the simulation is nearly 3 times that in Figure 6.8(b).

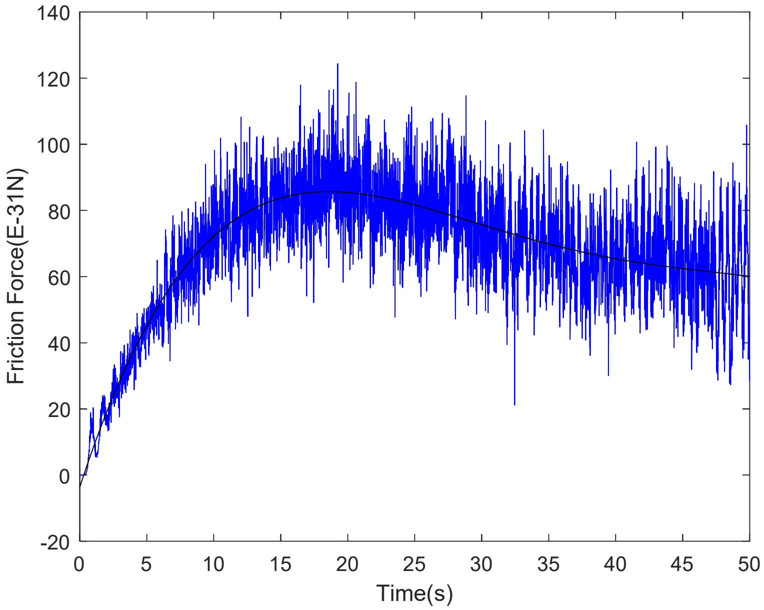

Figure 6.17. Friction force vs time ($k_0 = 50$). Note that the black line represents the average values of the blue curve.

As for the case of $k_0 = 80$, the velocity of the top plate and the displacement of the ends of the bonds are similar to those in Figure 6.18. In the aspect of the fraction of intact bonds, it remains stable at 0.7 in the first 10 seconds. It then dramatically decreases to 0.1 and maintains at the same level until the end of the simulation. The spring force also levels off after a short increase in the first 10 seconds due to the rupture of the majority of the bonds. Figure 6.19 shows that there is a sharp decrease of the friction force occurring after 10 seconds, when the force peaks at $82 \times 10^{-31} N$. The value of the friction force oscillates at approximately $20 \times 10^{-31} N$, which is much smaller than that in Figure 6.17.

The results above shows that k_0 has great effect on the behavior of the bonds. The bonds are broken during the top plate sliding when k_0 increases. The friction force is influenced by the status of the bonds. The maximum value of the friction force increases as k_0 increases. However, the average friction force in the time period of the simulation is the highest in the case of $k_0 = 50$, compared to the cases of $k_0 = 10$ and $k_0 = 80$. This indicates that k_0 can be adjusted to maximize the energy dissipation of the system.

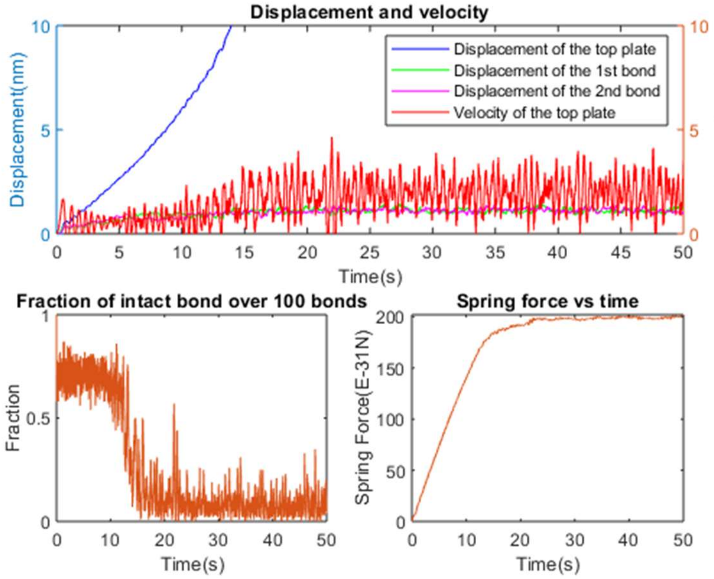

Figure 6.18. Displacement and velocity of the top plate and the displacement of the ends of first, second bond over time (Top figure). Fraction of the intact bonds over the total bonds (bottom left figure). Spring force (bottom left figure). ($k_0 = 80$)

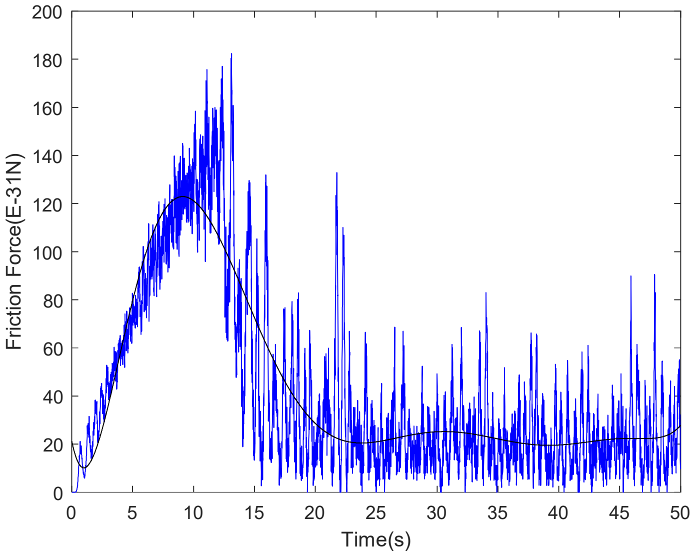

Figure 6.19. Friction force vs time ($k_0 = 80$). Note that the black line represents the average values of the blue curve.

6.2.6 Effects of Bond Reforming Rate

Similar to k_0, k_{on}^0 is associated with the reforming of the bonds. Two additional values of k_{on}^0 (50 and 150) are used to investigate the effects of this parameter.

Figure 6.20 shows that the oscillation of the velocity of the top plate increases after 10 seconds. The displacement of the ends of the bonds is maintained at about 1 nm. The fraction of the intact bonds stays at approximately 0.5, which is higher than that in the case of $k_{on}^0 = 50$. It is found that there is a linear increase of the spring force after 32 seconds. This could be related to the change of the friction force in Figure 6.21. It can be seen that the friction force has a short decrease from 25 to 40 seconds after it peaks.

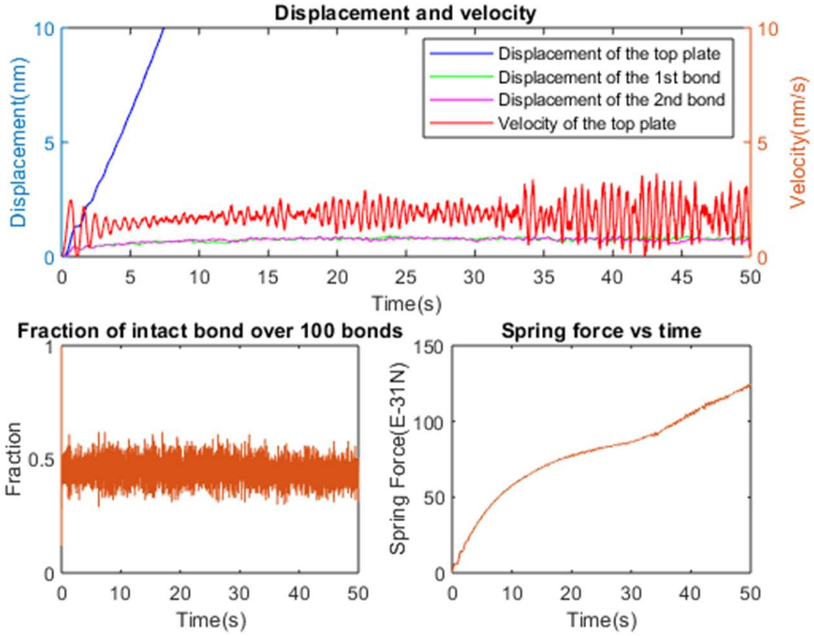

Figure 6.20. Displacement and velocity of the top plate and the displacement of the ends of first, second bond over time (Top figure). Fraction of the intact bonds over the total bonds (bottom left figure). Spring force (bottom left figure). ($k_{on}^0 = 50$)

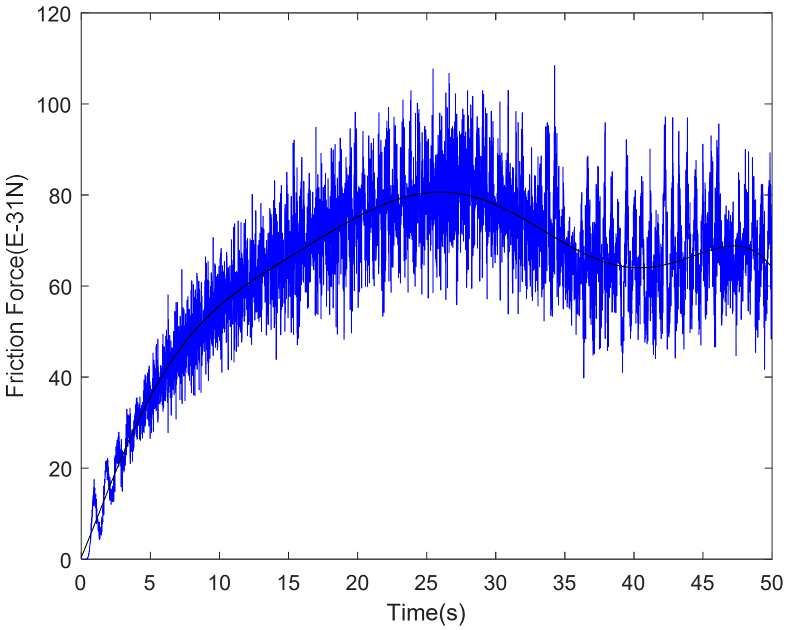

Figure 6.21. Friction force vs time ($k_{on}^{0} = 50$). Note that the black line represents the average values of the blue curve.

It is shown in Figure 6.22 that the oscillation of the velocity of the top plate is much smaller than that in cases $k_{on}^{0} = 50$ and $k_{on}^{0} = 150$. The displacement of the ends of the bonds is maintained at approximately at 0.2 nm, which is also the smallest among all the cases. The fraction of the intact bonds is 0.22 and is maintained at about the same level throughout the simulation. It can also be seen that the spring force is about $3.5 \times 10^{-3}\ N$ after the initial oscillation. The friction force levels off at about $2.8 \times 10^{-3}\ N$. Compared to the case of $k_{on}^{0} = 100$ in Figure 6.8(b), the friction force is 9 times smaller. It is believed that k_{on}^{0} affects the fraction of the intact bonds in the system. There are fewer bonds connecting between the surfaces in case $k_{on}^{0} = 150$, compared to the cases $k_{on}^{0} = 50$ and $k_{on}^{0} = 150$. The friction force therefore decreases.

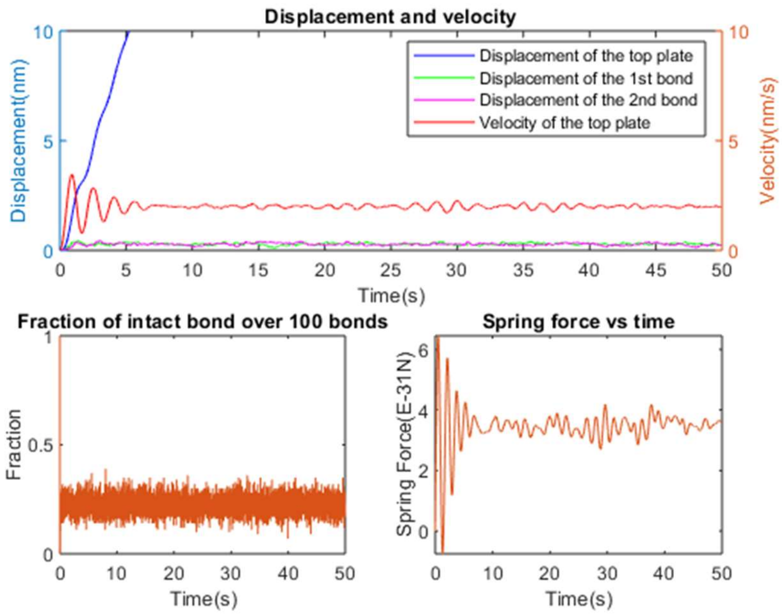

Figure 6.22. Displacement and velocity of the top plate and the displacement of the ends of first, second bond over time (Top figure). Fraction of the intact bonds over the total bonds (bottom left figure). Spring force (bottom left figure). ($k_{on}^{0} = 150$)

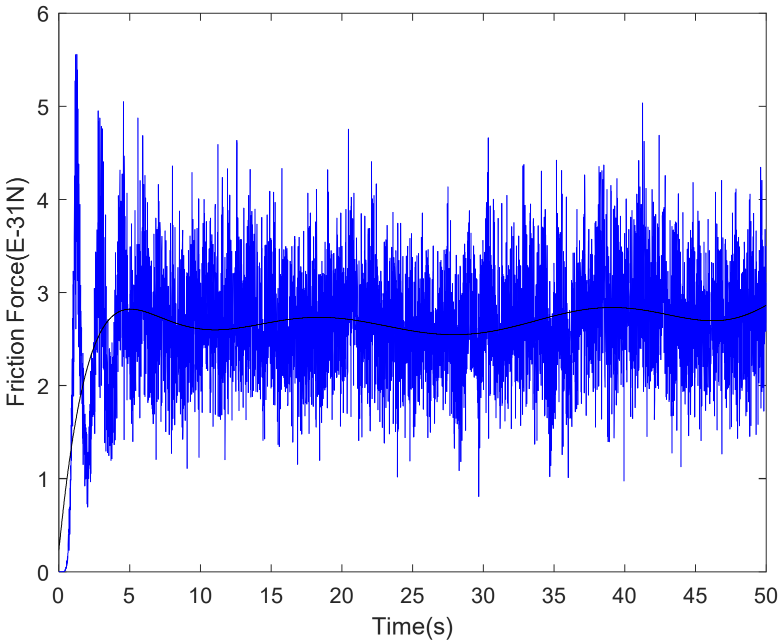

Figure 6.23. Friction force vs time ($k_{on}^{0} = 150$). Note that the black line represents the average values of the blue curve.

6.2.7 Conclusion

In summary, the friction model is a simplified one-dimensional intermolecular contact model. The friction forces existing between the two sliding surfaces originate from the spontaneous dissociation and reformation of the intermolecular bonds. By conducting the parameter studies, the model is shown to be significantly affected by the mass of the sliding surfaces, the sliding velocity [268], and the rates of the bonding dissociation and reformation. The effect of the size of the particles on energy dissipation can be studied by varying the mass of the sliding surfaces. The energy dissipation affected by the initial input (displacement or velocity) to the samples can be investigated by changing the sliding velocity of the plate. For more potential fillers that can be used as reinforcement in PA610, the rate of the bonding dissociation and reformation varies with the filler material. The results of the simulation can be worked as a reference to guide the design of the new composites in improving the energy dissipation capability. However, in the system of CNC-reinforced PA610 composites, the bonding between the filler and the matrix is strong because of the presence of hydrogen bonding [279]. This strong intermolecular force will limit the frictional sliding at the interfaces between the filler and the matrix. Thus, the friction force cannot fully account for the great energy dissipation in CNC-reinforced PA610 composites. Meanwhile, the intermolecular force is modeled as a linear spring for simplicity. It crudely shows the behaviors of the intermolecular bonds. A more precise intermolecular force equation such as the Lennard Jones force [275] is needed to substitute for the linear spring intermolecular force in the model.

6.3 Massless Adhesion Model

6.3.1 Massless Adhesion Model Overview

In addition of friction model, A potential energy dissipation mechanism is found in adhesion. In [255], the interaction of a pair of massless materials in adhesive, elastic contact is modelled. Irreversible jumps in force state in this massless model during changes in position are described as potentially leading to energy dissipation. In [280], internal friction is shown to be mainly controlled by adhesion, suggesting that the "intermolecular jump" in adhesive contact is a factor in energy dissipation, and hence damping, under low load. Adhesion hysteresis is shown [256] to be related to surface roughness and chemical heterogeneity. The deformable surface plays a role in accounting for adhesion hysteresis when the intermolecular force is conservative. In the case of CNC and PA610 composites, as studied in the dissertation, interfacial friction requires normal contact loading and interfacial sliding which is believed less likely to occur at low amplitude vibrations, compared to adhesion hysteresis produced by molecular bonding. Therefore, a crude massless adhesion model is built based on the study [255].

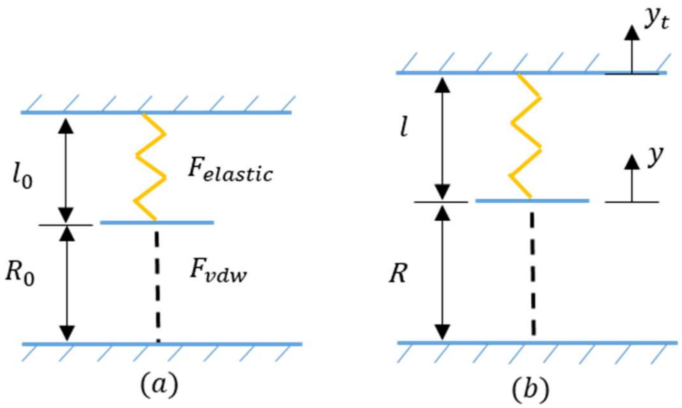

Figure 6.24. (a) Schematic of the two masses model (at initial position). (b) Schematic of the model with the direction of the moving boundaries (after movement).

In Figure 6.24, there are two surfaces interacting with each other. A surface is modeled as a rigid wall at the bottom. The top surface is elastic, consisting of a rigid boundary at the top, a linear spring in yellow that represents the elastic force when the surface deforms, and a contacting surface located in the middle of the graph. Intermolecular forces (Van der Waals force) exist between the two contacting surfaces (shown in dashed lines). The intermolecular distance between the contacting surfaces changes when the surfaces approach or depart. The bottom surface is fixed in the simulation for simplicity while the top boundary moves up and down.

The intermolecular force is modeled using Lennard Jones potential [275]. This equation is converted from equation (6.2).

$$F_{vdw}(R) = \frac{4\varepsilon}{\sigma}\left[-12\left(\frac{\sigma}{R}\right)^{13} + 6\left(\frac{\sigma}{R}\right)^{7}\right] = 6\left(\frac{A_{att}}{R}\right)^{7} - 12\left(\frac{B_{rep}}{R}\right)^{12} \tag{6.19}$$

A_{att} and B_{rep} are the constants for the attractive and repulsive components of Lennard Jones force. R is the intermolecular distance between the two contacting surfaces.

The elastic force is modeled as a linear spring. it is given as:

$$F_{elastic}(l) = k(l - l_0) \tag{6.20}$$

$$R = l_0 + R_0 + y_t - l \tag{6.21}$$

l_0 is the initial length of the elastic element of the top surface. l is the length of the elastic element. k is the spring constant of the elastic force. y_t is the displacement of the top boundary. y is the displacement of the top contacting surface. The elastic force equals the intermolecular force in the model.

$$F_{vdw}(R) = F_{elastic}(l) \tag{6.22}$$

It is noted that the initial intermolecular length is R_0.

In the simulation, the values of the parameters are shown in the table below:

Table 6.3. Parameters for massless adhesion model

parameters	value	unit
$\boldsymbol{A_{att}}$	10^{-5}	$nN \cdot nm^{7}$
$\boldsymbol{B_{rep}}$	10^{-8}	$nN \cdot nm^{13}$
$\boldsymbol{R_0}$	0.7	nm
$\boldsymbol{k}$	0.1	nN/nm
$\boldsymbol{l_0}$	0.0072	nm

6.3.2 Results and Discussions

The top boundary connected to the top contacting surface is moving down and up at a constant speed. In Figure 6.25, the intermolecular distance decreases as the top rigid wall moves down. It can be seen that the intermolecular distance suddenly changes from 0.5 nm to 0.37 nm at 0.17 ns. It can be called a "jump in." The decreasing rate of the intermolecular distance is lower than that before the jump because it is affected by the strong repulsive intermolecular force. When the top plate moves up, another change of the intermolecular distance occurs at 0.46 ns. This "jump out" starts from 0.4 nm to 0.55 nm. In one contacting cycle in which the two surfaces approach and depart from each other, two "jumps" occur in the process.

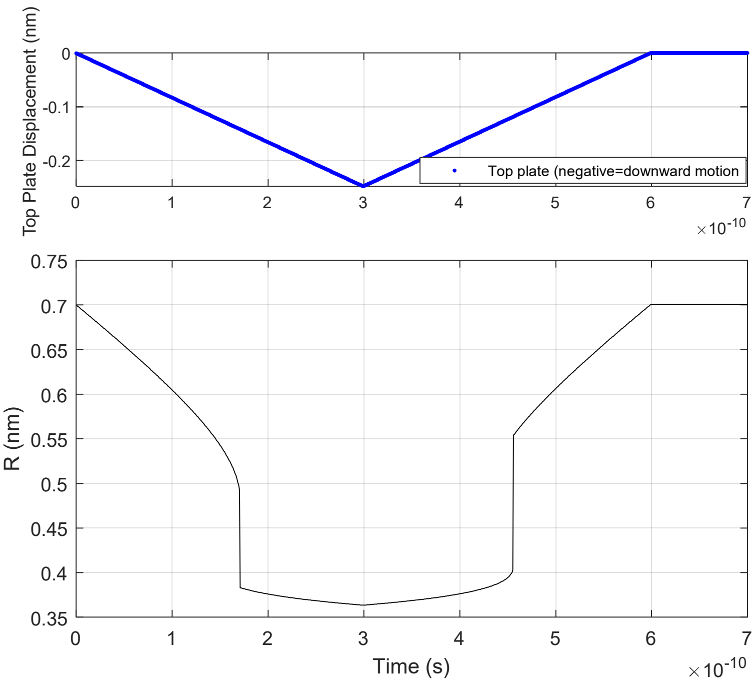

Figure 6.25. The displacement of top boundary (top), the intermolecular distance (bottom) vs time.

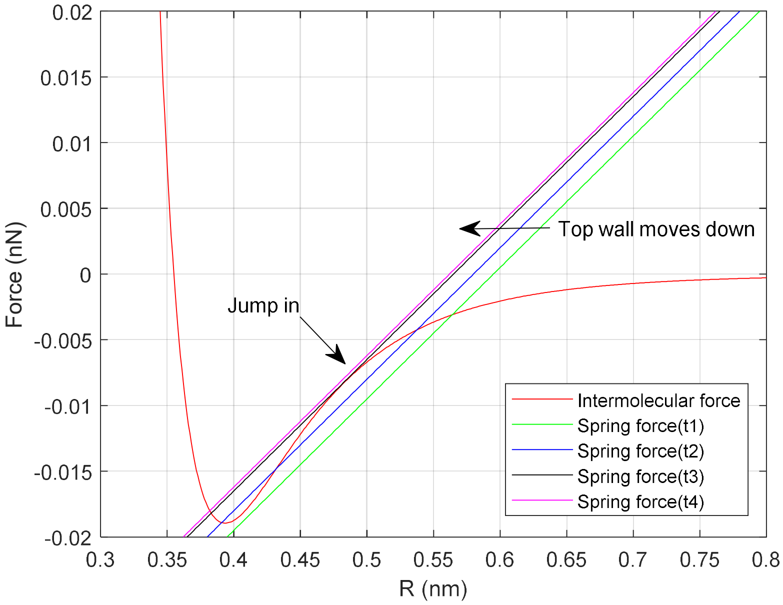

Figure 6.26. Intermolecular force and spring force vs the intermolecular distance. Different spring force curves are shown at four time points when the top boundary moves down.

Figure 6.26 shows the process of the intermolecular jump. Because the spring force equals the intermolecular force during the simulation, the intersection points (roots calculated from equation (6.22)) of the intermolecular force curve and the spring force curves represent the current status of the forces in the model. As the top wall moves down, four spring force curves at different time points are shown from the right side to the left. There is one intersection point for the green spring force and intermolecular force curves when the simulation runs to the first time point (t1). It can be seen that the intermolecular distance is 0.565 nm at this time point. Then the top wall moves further, and the spring force changes to the blue curve at the time point (t2). Three intersection points are made by the intermolecular force and spring force curves. Even though three possible roots can be found for equation (6.22), only one root (R = 0.54 nm) was used in the simulation as this root moves along the intermolecular force curve from t1 to t2. When the time goes to t3, a "jump in" point at R = 0.49 nm can be seen between the two intersection points. At this point, the gradient of the spring force (the spring constant) equals that of the intermolecular force. When the intermolecular distance decreases from the jump in point, the gradient of the intermolecular force will exceed that of the spring force. Then the top contacting surface will accelerate because of the imbalance of the forces. After the time changes from t3 to t4, there is only one intersection between the spring force and the intermolecular force curves. The jump in point disappears and the intermolecular distance decreases from 0.49 nm at t3 to 0.37 nm at t4. This significant intermolecular distance decrease is intermolecular jump, and it occurs spontaneously due to the disappearance of the root and the acceleration of the contacting surface.

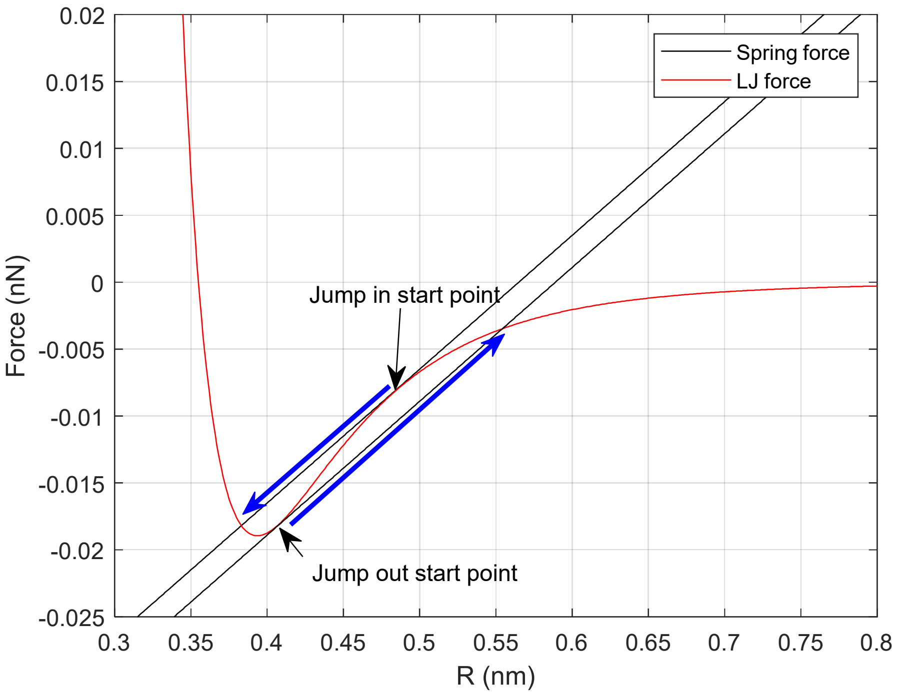

Figure 6.27. The process of jump in and out in the intermolecular and the spring force plot.

In the discussion of Figure 6.26, intermolecular jump in occurs from the jump in start point and stops at the other intersection point shown in Figure 6.27 above. Similarly, when the top wall begins departing from the bottom surface, jump out will also occur during the process. The jump out start point in this case is R = 0.41 nm. It jumps to R = 0.55 nm. It accounts for the two intermolecular jumps in Figure 6.25 when the top wall approaches and departs from the bottom wall. It can be viewed as one bonding and debonding cycle.

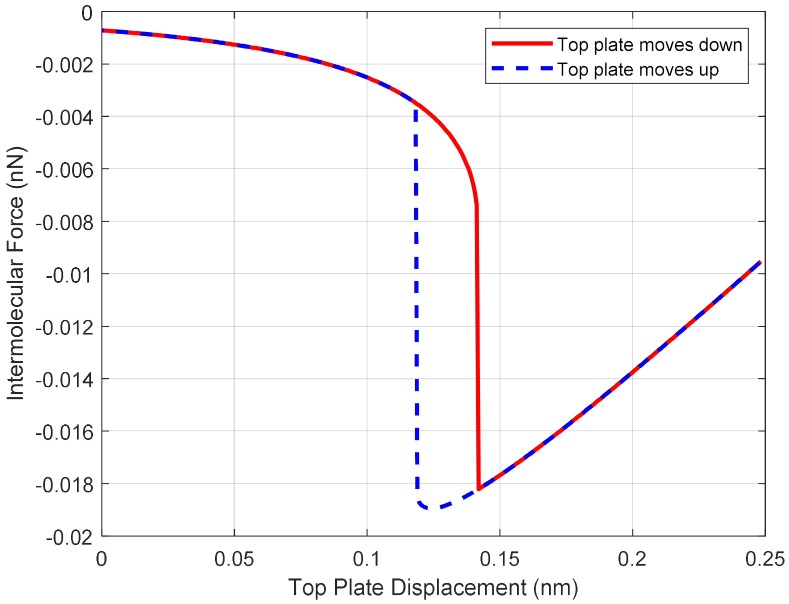

Figure 6.28. The intermolecular force vs the displacement of the top boundary in a bonding and debonding cycle.

In a bonding and debonding cycle, energy dissipates from the system due to the intermolecular jumps. As shown in Figure 6.28, a hysteresis loop is formed by the intermolecular force after one cycle of the top plate's movement. The area enclosed by the blue and red curves represents the energy dissipating from the system.

6.3.3 Conclusion

In summary, this model shows the intermolecular jump phenomenon between the surfaces in the cycle of approaching and departing. It requires an elastic force from the deformation of the surfaces during contacting. Because of the instability of the elastic force and the intermolecular force at jump points, the intermolecular jump occurs spontaneously and the kinetic energy gained during the jump dissipates as heat. Because of the intermolecular force and distance changes after the jump, the intermolecular jump is then called intermolecular change in state in this dissertation for the following sections.

However, this adhesion model ignores the mass of the contacting surface. It results in instant energy dissipation after intermolecular jump. A more realistic model is needed to study details of energy transfer and dissipation.

6.4 Adhesion Model with a Mass

Mass is added to the contacting surface based on the previous massless model. The value of the mass is $2 \times 10^{-25} kg$. The other parameters use the same values in the Table 6.3.

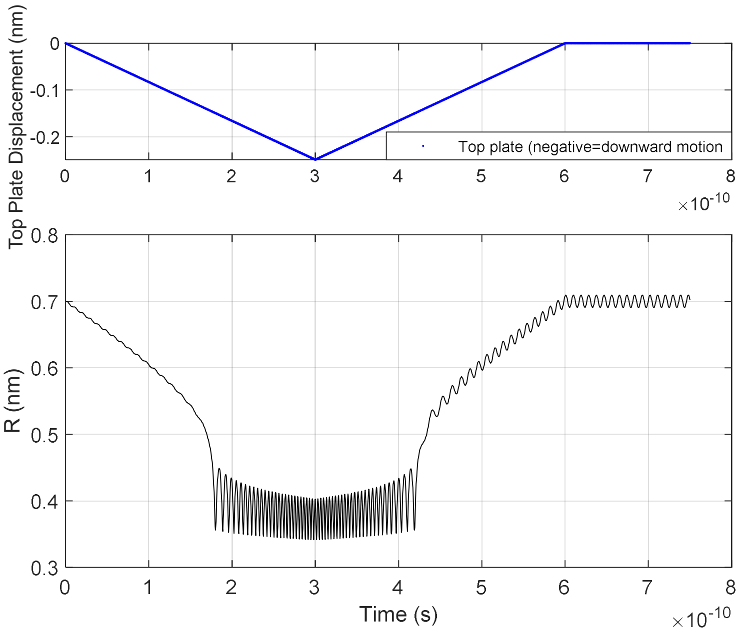

Figure 6.29. The displacement of top boundary (top), the intermolecular distance (bottom) vs time. (mass is added to the contacting surface).

As shown in Figure 6.29, intermolecular changes in state occur during one bonding and debonding cycle. It can be seen that the change in state is not a "teleport" from one point to the destination point. The top contacting surface is accelerating after the jump. Due to the repelling force, the contacting surface starts to vibrate in the amplitude of 0.8 nm after the first jump. As the top wall moves down further, the amplitude of the vibration decreases while the frequency increases. Then the second intermolecular change in state occurs as the top boundary moves up.

It is interesting that the jump occurs at the same intermolecular distance as the first jump. This indicates that the mass of the contacting mass changes the behavior of the intermolecular jump. There is a small vibration in the amplitude of 0.2 nm after the second jump. Compared to the amplitude of the vibration when the top wall moves down, it shows there is some kinetic energy transferred to the mass after one bonding and debonding cycle.

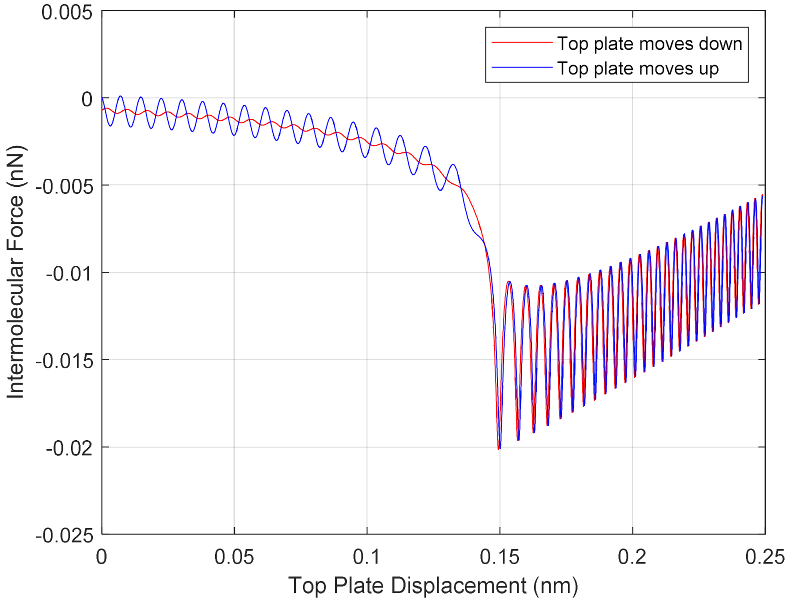

Figure 6.30. The intermolecular force vs the displacement of the top boundary in a bonding and debonding cycle (mass is added to the contacting surface).

Figure 6.30 shows that the jump in and out occur in the same intermolecular distance. The intermolecular force curves are approximately the same when the top plate displacement is larger than 0.15 nm. It is believed that the oscillation of the mass makes the intermolecular distance reach the jump out length in advance. The potential change of the intermolecular force transfers to the kinetic energy of the contacting surface during the jump. However, the kinetic energy does not transfer to heat due to lacking means of energy dissipation.

Here a damper accounting for the energy dissipation by heat at the molecular level is proposed. This damper is added between the top contacting surface and the bottom material.

More details of the damper will be discussed in the improved adhesion model. The damping force is given as:

$$F_d(y) = C\dot{y} \tag{6.23}$$

$$C = 2\sqrt{mk}\xi \tag{6.24}$$

ξ is the damping ratio in the value of 0.1. After the damper is introduced in the model, the simulation results are shown below.

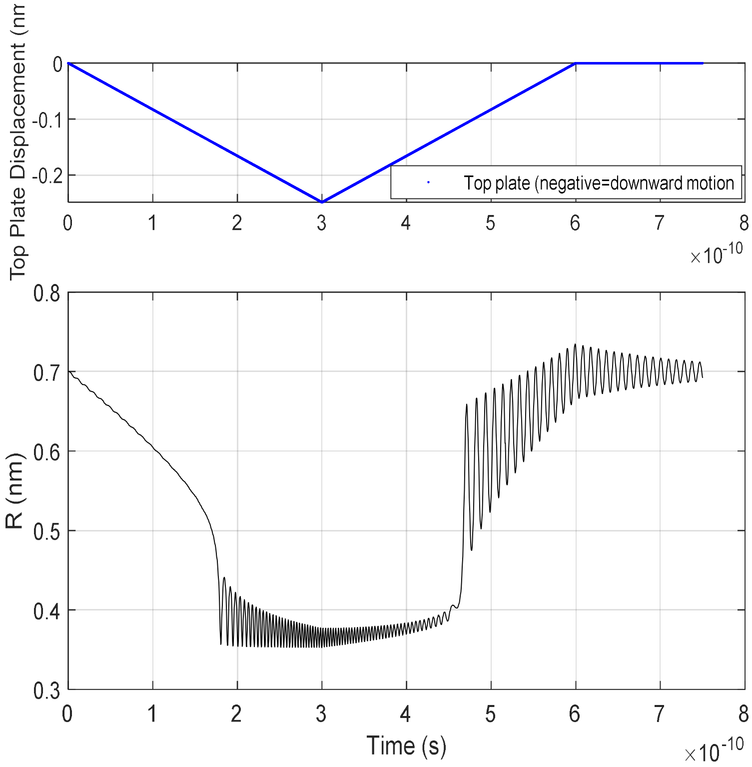

Figure 6.31. The displacement of top boundary (top), the intermolecular distance (bottom) vs time. (mass and a damper are added to the contacting surface).

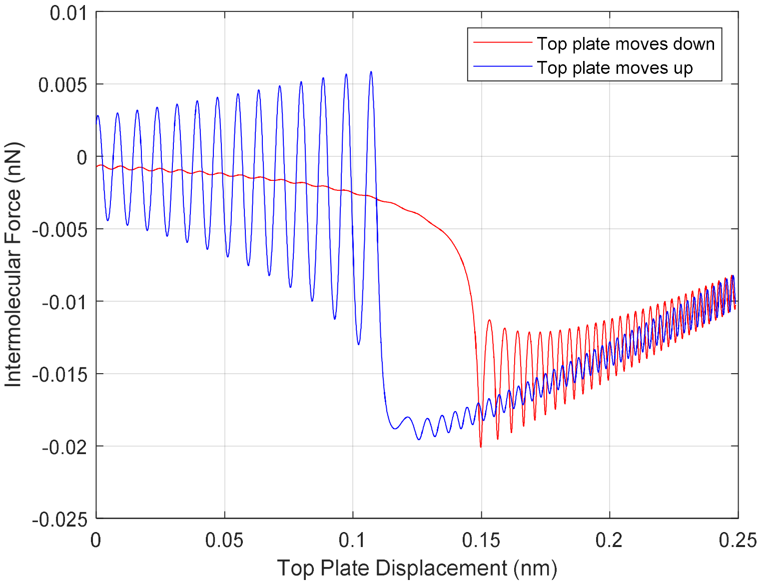

Figure 6.32. The intermolecular force vs the displacement of the top boundary in a bonding and debonding cycle (mass and a damper are added to the contacting surface).

After the damper is added to the model, it can be seen in Figure 6.31 that the amplitude of the vibration decreases. The kinetic energy in the mass dissipates into heat through the damper. In Figure 6.32, similar hysteresis curve is shown as in the massless case. Due to the decrease in the vibration, the jumping out does not occur in advance. The jumping out starting distance shifts from 0.15 nm in Figure 6.30 to 0.12 nm. The area enclosed by the red and blue curve is the energy dissipated from the system.

6.4.1 Conclusion

The model with mass and damper presents the intermolecular jump and energy transfer process more clearly. The intermolecular potential energy dramatically transfers to the kinetic energy of the mass by the intermolecular jump. The kinetic energy will gradually dissipate by intermolecular collision as heat. It is worth noting that the kinetic energy gained after the jump is significantly greater than that the case without intermolecular jump. Thus, the intermolecular jump dramatically enhances the energy dissipation in the system.

In the aspect of the great damping improvement in cellulose-reinforced PA610 composites, the intermolecular change in state can play an important role in the energy dissipation mechanism. However, the current model still cannot be specifically applied to cellulose/P610 composites. The hydrogen bonding existing between cellulose and PA610 is much stronger than Van der Waals force. In addition, the elastic force originating from the elastic deformation of the contacting surfaces needs to be modeled with more details. A model based on the cellulose-reinforced PA610 is needed to investigate the high damping improvement.

6.5 Improved Adhesion Model

In this section, an intermolecular adhesive contact model is developed for the interaction of nano-fillers and a polymer carrier, including hydrogen bonding and Van der Wall forces acting between the interacting materials. The equations for the model are derived and the case of composites consisting of PA610 polyamide matrix filled by cellulose fibers are treated numerically. Factors studied related to the energy dissipation in the composites are particle size, hydrogen bonding density, elastic modulus of the materials, and height of the surface asperities.

6.5.1 Improved Adhesion Model Overview

In this section, an intermolecular contact model is developed (Figure 6.33(a)) with a view toward studying the interaction of a particle embedded in a polymer matrix material, such as what commonly occurs in nano-reinforced composite materials. The mass of the filler, as well as the elasticity of filler and matrix, are included in the model.

The specific case treated is that of a nanocellulose particle embedded in PA610 polymer, but the model is applicable to any pair of materials. The top and bottom boundaries in Figure 6.33(a) represent the positions of the PA610 polymer surfaces, and the mass in the middle represents that of the CNC particle. The blue and purple springs represent the elastic stiffnesses of the PA610 matrix (k_m) and the CNC particle (k_p), respectively. The green and red dashed arrows are the hydrogen bond forces (F_H^t and F_H^b) and Van der Waals forces (F_{vdw}^t and F_{vdw}^b), respectively, per unit area acting between CNC and PA610. The superscripts t and b denote top and bottom elements, respectively. Because F_{vdw} and F_H are independent and both exist between the two contacting surfaces, they are modeled to be parallel, and the combination of the forces becomes the total intermolecular force which will be described in detail in the following intermolecular force section 6.5.2. A linear viscous damper is commonly used in the interaction between surfaces at atomic scale, such as the friction study in [248]. In the current model, the damper acts as the means to characterize the amount of kinetic energy dissipated from the system. This dissipation mechanism is explained using the many-body model in [235].

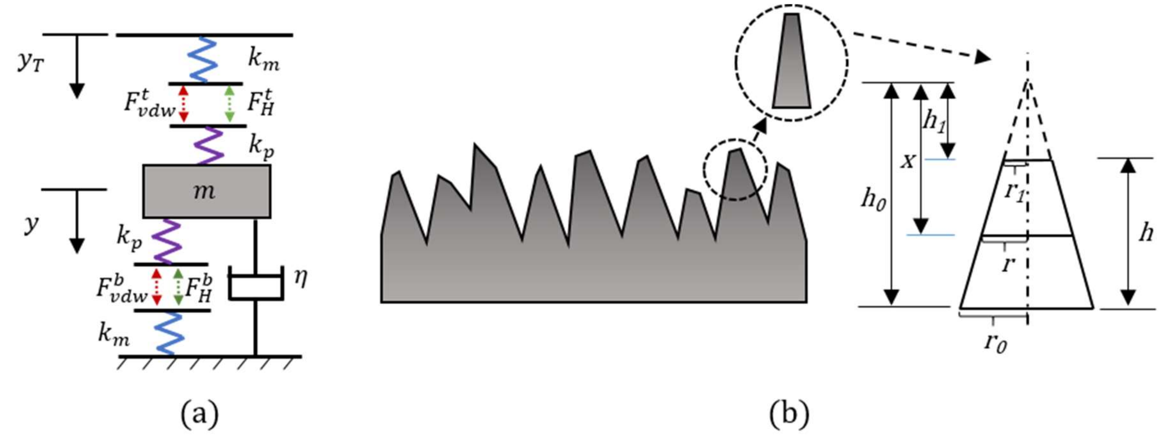

Figure 6.33. (a) Schematic graph of the model. (b) Schematic of the geometry of an asperity.

The model describes the intermolecular contact in a unit area. Thus, the constants in the equation below represent quantities per unit area. The governing equation of the model is:

$$m\ddot{y} + \eta\dot{y} - (F_{vdw}^t + F_H^t) + (F_{vdw}^b + F_H^b) = 0 \tag{6.25}$$

where an overdot denotes time derivative, y is the displacement of the CNC particle, y_T is the input to the system representing the motion of the bulk matrix material, m is the mass of the particle per unit area, and η is the damping constant per unit area which is given in terms of the mass m, the dimensionless damping ratio ζ, and the equivalent spring constant k_0:

$$\eta = 2\zeta\sqrt{k_0 m} \tag{6.26}$$

$$k_0 = \frac{1}{\frac{1}{k_p} + \frac{1}{k_m}} \tag{6.27}$$

In (6.25), k_p and k_m are related to the roughness of the contacting material surfaces and Young's moduli of the particle and matrix, as described in the following elastic force section 6.5.3. The elastic and intermolecular forces are related by:

$$F_{vdw}^{t} + F_{H}^{t} = F_{p}^{t} = F_{m}^{t} \tag{6.28}$$

$$F_{vdw}^{b} + F_{H}^{b} = F_{p}^{b} = F_{m}^{b} \tag{6.29}$$

where F_p^t and F_p^b are the forces per unit area in the top and bottom elastic elements of the CNC particle, respectively, and F_m^t and F_m^b are the forces per unit area in the elastic elements of the top and bottom matrix material, respectively. Note, in Figure 6.33(a) and equation (6.26), the top intermolecular forces are related to y_T and y. In the calculation of the bottom intermolecular forces, the bottom surface of the matrix is fixed, without loss of generality. Note also that all elastic elements are stretched in the initial balanced position due to the intermolecular forces.

6.5.2 Intermolecular Force

The intermolecular forces considered in this model are the Van der Waals force and the hydrogen bonding force. Here, the Van der Waals force is modeled using the Lennard-Jones adhesion potential [281]:

$$F_{vdw}(R) = \frac{A}{6\pi z_0^3}[\left(\frac{z_0}{R}\right)^3 - \left(\frac{z_0}{R}\right)^9] \tag{6.30}$$

where A is the Hamaker constant [282] and z_0 is the equilibrium distance of the force. These two constants are specified for the specific materials. Note that $F_{vdw}(R)$ in (6.28) is per unit area. Here, and in subsequent equations, the intermolecular distance R represents R_t or R_b for the top or bottom interacting surfaces, respectively. Expressions for R_t and R_b are given in Appendix A.

The Dreiding force field is commonly used for hydrogen bonding, and has potential energy given by [283]:

$$P_{Hs}(R) = D_H[5\left(\frac{R_H}{R}\right)^{12} - 6\left(\frac{R_H}{R}\right)^{10}]cos^4(\theta_{DHA}) \tag{6.31}$$

Here, θ_{DHA} (see Appendix C) which is a function of R, is the angle between the donor of the hydrogen atom, the hydrogen atom, and the acceptor of the hydrogen atom. D_H is the minimum potential energy of the force, and R_H is the equilibrium distance between the donor and acceptor atoms. The Dreiding force, $F_{Hs}(R)$, is:

$$\begin{aligned} F_{Hs}(R) &= -\frac{\partial P_{Hs}}{\partial R} \\ &= \frac{60D_H}{R_H}\left[\left(\frac{R_H}{R}\right)^{13} - \left(\frac{R_H}{R}\right)^{11}\right]cos^4(\theta_{DHA}) \\ &+ D_H\left[5\left(\frac{R_H}{R}\right)^{12} - 6\left(\frac{R_H}{R}\right)^{10}\right]\frac{d[cos^4(\theta_{DHA})]}{dR} \end{aligned} \tag{6.32}$$

This equation is for a single hydrogen bond. For generality, the model here is developed per unit area. The number of hydrogen bonds in a unit area is defined as n_H, so that (6.30) can be re-expressed per unit area as:

$$F_H(R) = n_H F_{Hs}(R) \tag{6.33}$$

It is noted that the intermolecular forces are dependent on the dependent variable y(t) because of the dependence of the intermolecular distances on y, as described in Appendix A.

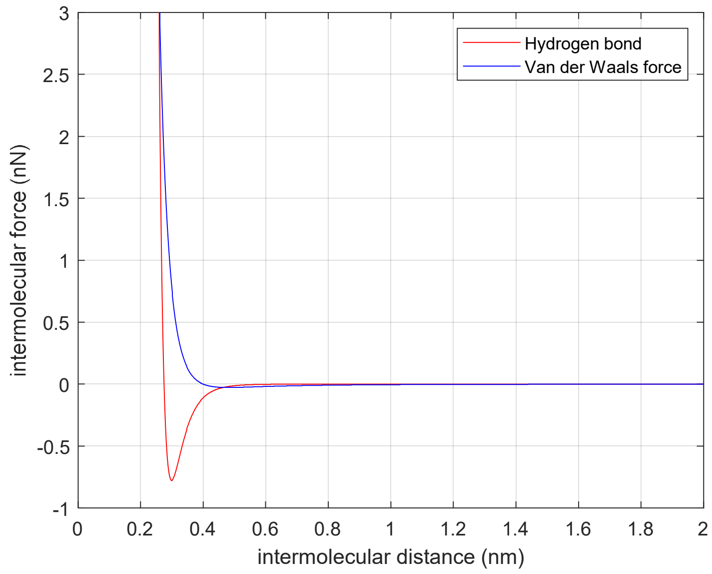

Figure 6.34. Comparison between hydrogen bonding and Van der Waals force vs intermolecular distance.

It can be seen from the figure 6.34 that the maximum attractive force (negative value) of hydrogen bonding is much larger than that of the Van der Waals force. Meanwhile, the blue and red curves peak at different intermolecular distances. Thus, the presence of hydrogen bonding has more potential effect on the adhesion behavior of the surface contact between cellulose and PA610 than Van der Waals force.

6.5.3 Elastic Force

When surfaces make contact, asperities deform significantly more than the bulk material. Thus, for the nanoscale of the present model, the elastic elements are modeled based on the surface asperities. Here, surface asperities are modeled as a truncated cone-shape (Figure 6.33(b)), adapted from that in [284].

In Figure 6.33(b), r_0 and r_1 are the radii of the bottom and top circular surfaces, respectively, h_0 and h_1 are the heights of the whole cone-shaped asperity and the truncated part of the cone, respectively, and h is the height of the asperity. The variable x is the distance to a cross section of the asperity from the tip of the same whole cone, and r is the radius of this cross section.

The deformation of the asperity can be obtained by

$$\Delta h = \int_{h_1}^{h_0} \varepsilon \, dx = \frac{f}{E} \int_{h_1}^{h_0} \frac{1}{A_s} dx \tag{6.34}$$

where ε is the axial normal strain of the asperity under the applied force, f, E is Young's modulus of the material, and A_s is the area of the cross-section given by $A_s = \pi(r_0/h_0)^2 x^2$.

Then, the relationship between the deformation Δh and the elastic force per unit area, F_a, is

$$F_a = \frac{f}{\pi r_0^2} = \frac{E\Delta h}{h\dfrac{h_0}{h_1}} \tag{6.35}$$

From equation (6.33) the equivalent stiffness per unit area of an asperity of height h is

$$k = \frac{f}{\Delta h \pi r_0^2} = \frac{E}{L} \tag{6.36}$$

where $L = h(h_0/h_1)$.

Similarly, the equivalent stiffnesses of the matrix and particle in the developed model are

$$k_p = \frac{E_p}{h_p \dfrac{h_{\mathrm{p0}}}{h_{\mathrm{p1}}}} = \frac{E_p}{L_p} \tag{6.37}$$

$$k_m = \frac{E_m}{h_m \dfrac{h_{\mathrm{m0}}}{h_{\mathrm{m1}}}} = \frac{E_m}{L_m} \tag{6.38}$$

The elastic forces of the particle and matrix for the top and bottom parts are given as:

$$\begin{aligned} F_p^t &= k_p \Delta h_1 \\ F_m^t &= k_m \Delta h_3 \end{aligned} \tag{6.39}$$

$$\begin{aligned} F_p^b &= k_p \Delta h_2 \\ F_m^b &= k_m \Delta h_4 \end{aligned} \tag{6.40}$$

Δh_1, Δh_2, Δh_3, and Δh_4 are shown in Appendix A.

6.5.4 Parameters

The parameters used in the model, and their corresponding sources, are summarized in Table 6.4.

Table 6.4. Parameters for the improved adhesion model

Parameters	Reference
m = 1.5 e-22 kg/nm^2	*
E_m = 1.4 nN/ nm^2	**
E_p = 145 nN/ nm^2	[60]
h_m = 0.5 nm	[285, 286]
h_p = 0.5 nm	[285-287]
A = 8.45 e-20 J	[288, 289]
Z_0 = 0.343 nm	[275, 283]
D_H = 9.5 kcal/mol	[283]
R_H = 0.276 nm	[283]
n_H = 2 nm^{-2}	[290]
θ = 165°	[279]
L_{ab} = 0.95 nm	[283]
ζ = 0.3	[248, 291]

* Calculated from company specifications [267]. ** Experimentally measured by the author.

The values in the model are for the case of CNC reinforced PA610. The mass m of the CNC particles derived from the density and size of the spherical particle (Diameter, D = 100 nm) from manufacturer's material specification literature. The elastic modulus E_m are based on tensile test results in [267]. The ratio of $h_{p0}/h_{p1}$and h_{m0}/h_{m1} are set as 3, based on transmission electron microscopy of similar materials in [292]. Note that results will be given for a range of parameter values.

6.5.5 Numerical Solution

The governing equations for the model are (6.23), (6.26-6.28), (6.30), (6.31), (6.37), (6.38), (A.2) and (A.3). These form a system of 17 coupled, nonlinear differential equations (note that equations (6.26-6.28), (6.30), (6.31), (6.37), (6.38) each represent one equation for the top and one for the bottom segments of the model) for F_{vdw}^{t}, F_{H}^{t}, F_{p}^{t}, F_{m}^{t}, F_{vdw}^{b}, F_{H}^{b}, F_{p}^{b}, F_{m}^{b}, F_{Hs}^{t}, F_{Hs}^{b}, R_t, R_b, Δh_1, Δh_2, Δh_3, Δh_4, y. Solving these directly using a common numerical technique such as the Runge–Kutta method is computationally prohibitive. Here, a predictor-corrector-method, called "velocity Verlet," widely used in molecular dynamic simulations, is applied for the calculation [293]. The solution procedure is as follows. The first step is setting $y = 0$ and giving an initial input to y_T in the initial time step. Then, Δh_1 is substituted from equation (A.2) into both of (6.37). These expressions, along with (6.28), (6.30), (6.31) (for the top segment), are substituted into equation (6.26), giving two coupled equations for R_t and Δh_3 from which R_t and Δh_3 are determined at this instant. Simultaneously, R_b and Δh_4 are determined in the same way using equations (A.3), (6.38), (6.28), (6.30), (6.31) and (6.27). Note that a final graph of R_b vs y is shown in Figure B.1 in Appendix B. This so called "root graph" is used to determine the roots at each instant. With R_t, R_b, Δh_3, Δh_4, Δh_1 and Δh_2 determined at this instant, "velocity Verlet" is applied to solve the equation of motion. The algorithm has predictor and corrector stages. For the predictor stage, the displacement of the particle $y(t)$ and its velocity $v(t)$ are predicted as:

$$y^p(t+\delta t) = y(t) + \delta t v(t) + \frac{1}{2}\delta t^2 a(t) \tag{6.41}$$

$$v^p\left(t+\frac{1}{2}\delta t\right) = v(t) + \frac{1}{2}\delta t a(t) \tag{6.42}$$

where δt is the time step of the simulation and a superscript p denotes the predictor stage. For the corrector stage, the acceleration $a(t)$ or $\ddot{y}(\mathrm{t})$ of the particle is calculated using (6.23) in the form:

$$ma(t+\delta t) = \ F(y^p, v^p) \tag{6.43}$$

where $F(y^p, v^p)$ is the force exerted on the particle. The velocity is then corrected (v^c) based on the predicted velocity and acceleration.

$$v^c(t+\delta t) = \ v^p\left(t+\frac{1}{2}\delta t\right)+\frac{1}{2}\delta t a(t+\delta t) \tag{6.44}$$

The corrected velocity and acceleration are used to predict the displacement of the particle y in the next time step, and y is used in equations (A.2) and (A.3) in the first step of the solving procedure, which is iteratively repeated. Note that the calculation (6.41) requires roots R_t and R_b. These are taken from the root graph (e.g. Figure B.1) at each instant.

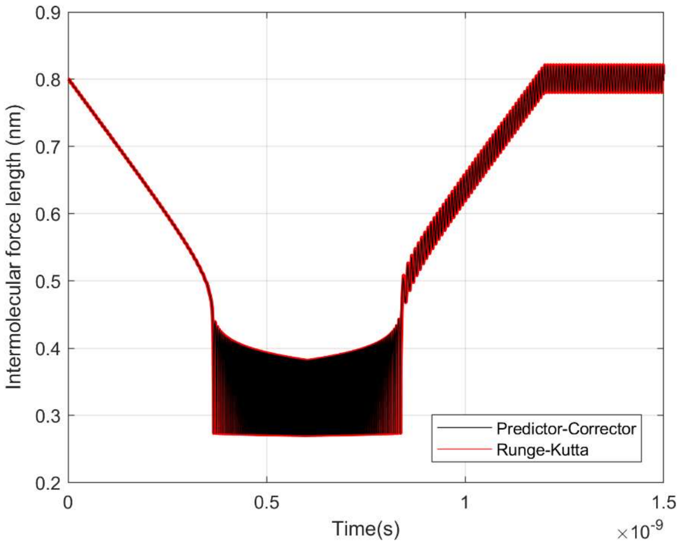

Figure 6.35. Comparison between predictor-corrector and Runge Kutta methods on a simple model.

In Figure 6.35, predictor-corrector and Runge Kutta methods are used to calculate the intermolecular force for a simplified version of the model in Figure 1in which only one set of intermolecular and elastic forces act on the particle. Minor deviation between the curves can be seen, which indicated predictor-corrector method is accurate to be applied to the more complex models.

6.5.6 Results and Discussion

The simulations are conducted on the model with the bottom support (bottom matrix material) fixed. The response of the system is driven by various cases of prescribed motion of the top support (top matrix material). To create a similar dynamic condition as the damping tests in [267], Figure 2(a) treats sinusoidal vibration of the top surface at a frequency of 80 Hz, which is selected from the average natural frequency of the CNC/PA610 samples in [267].

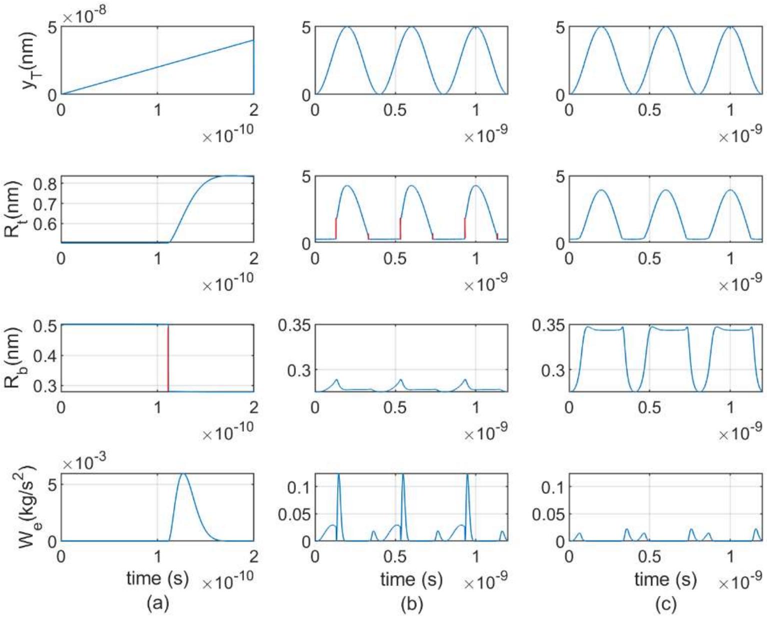

Figure 6.36. Displacement input y_T and resulting response R_t and R_b, and kinetic energy W_e of the model. (a) Sinusoidal input displacement at 80 Hz (appears linear over this very short time); (b) sinusoidal input at 2.5 GHz; (c) sinusoidal input at 2.5 GHz with hydrogen bonding omitted from the model.

Plots in Figure 6.36(a) show a sudden and rapid change in intermolecular distance R_b (shown in red) of the bottom contacting surfaces, as well as an attendant increase in kinetic energy and intermolecular distance change R_t. The increase of the kinetic energy is due to increase in velocity of the mass brought upon by the imbalance of the forces exerted on its top and the bottom surfaces. The viscous damper in the model dissipates kinetic energy gained during the sudden intermolecular change in state, which is shown by the decrease of the maximum kinetic energy.

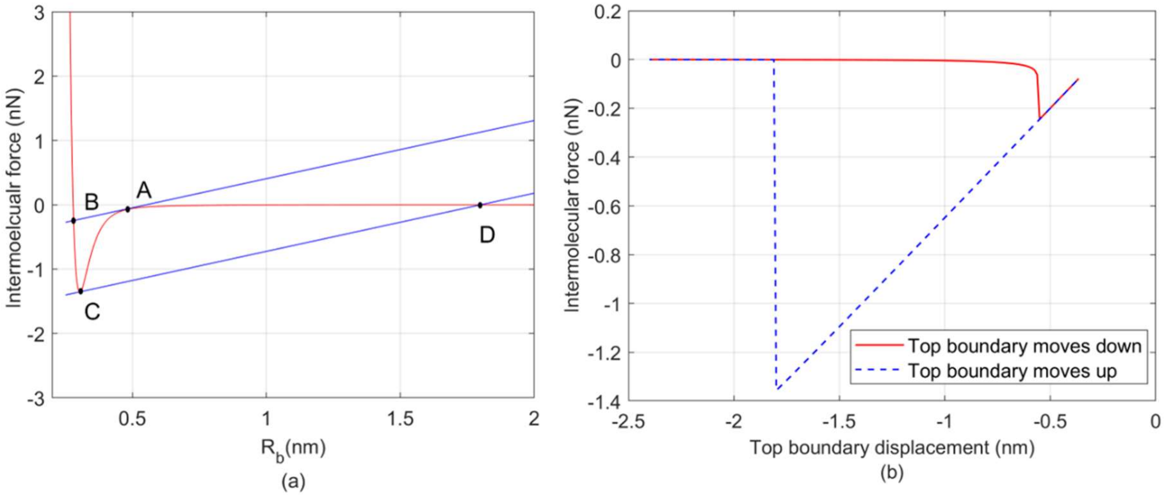

Figure 6.37. (a) Total bottom intermolecular force (red curve) vs intermolecular distance graph. The total elastic force in two instances are given by the blue curves. (b) Intermolecular force vs top boundary displacement graph.

Similar to the massless adhesion model, Figure 6.37(a) presents the mechanism of the sudden intermolecular change in state in the case of Figure 6.36(a) in presence of hydrogen bonding and Van der Waals force. When the top surface moves down, the intermolecular distances decrease. For a massless system in [255], it is shown that sudden intermolecular change in state can occur when the slope of the total elastic force equals the slope, with, respect to R_b, of total intermolecular force. In Figure 6.37(a), this is possible at Points A and C and would result in sudden change of states from A to B and C to D. For example, as y_T increases, R_b decreases from its initial value of 2 nm and moves towards point A where the intermolecular state "jumps" to point B. Similar behavior can occur from C to D if R_b later increases.

It can be seen in Figure 6.37(b) that the sudden intermolecular changes in state are irreversible and produce hysteresis in the system. In the figure, the simulation is conducted for the case of zero mass and no damper. The hysteresis loop is therefore entirely due to the "jumps" in state. Deng also showed hysteresis loops due to this phenomena for Maugis–Dugdale model [284].

To demonstrate the effect of hydrogen bonding and multiple intermolecular changes of state on the interaction of these materials, results for the case of an input sinusoidal vibration of y_T at 2.5 GHz for three cycles of the vibration are given in Figures 6.36(b), which includes hydrogen bonding, and Figure 6.36 (c) in which hydrogen bonding is omitted. This frequency is selected for convenience since it allows the model to run in a reasonable amount of computational time. As the input displacement y_T cycles up and down, Figure 6.36 (b) shows sudden increases of intermolecular distance R_t each cycle (shown in red), whereas these changes of states do not occur in the case of Figure 6.36 (c). This is due to hydrogen bonding in Figure 6.36 (b) increasing the intermolecular force and shifting it into a range where sudden intermolecular changes in state must occur for the elastic forces to balance the intermolecular forces. The sudden intermolecular changes in state in Figure 6.36 (b) produce sudden increases of the kinetic energy, and the peak kinetic energy of the particle in Figure 6.36 (b) is seen to be 455% greater than that in Figure 6.36 (c).

The work done by the damping force in the cases with and without hydrogen bonding is shown in Figure 4 as the process progresses. The Figure shows that the transfer of the potential energy to kinetic energy in Figure 6.36(b) results in an increase in energy dissipation by viscous damping, compared to Figure 6.36(c). Specifically, the work done by the damping force is 360% greater in the hydrogen bonding case compared to 6.36(c) where hydrogen bonding is omitted.

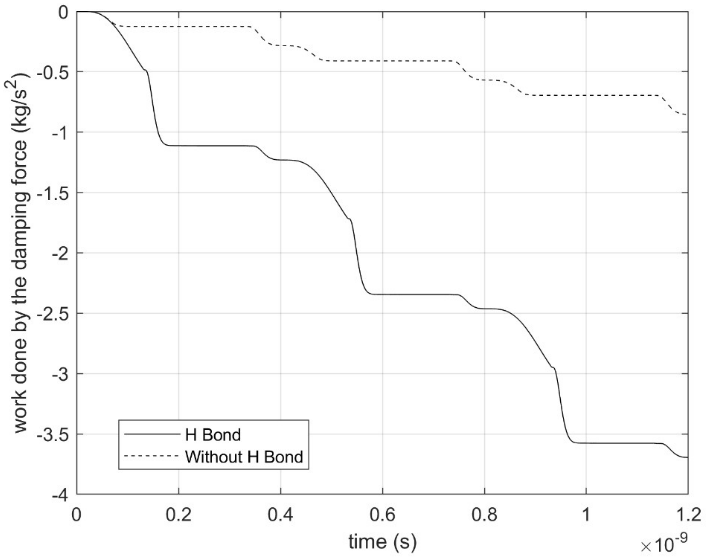

Figure 6.38. The work done by the damping force (per unit area) with and without hydrogen bonding participating in the simulations in Figures 6.36(b) and 6.36(c).

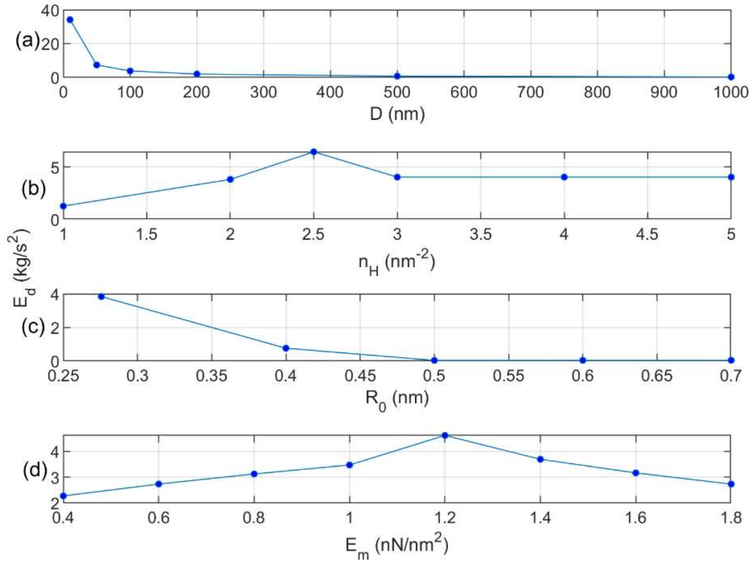

Figure 6.39. The energy dissipation after 3 cycles of the top material displacement (same input as in Figure 6.36(b)) in terms of (a) size of the particles for n_H= 2 nm^{-2}, R_0= 0.276 nm, E_m = 1.4 nN/nm^2; (b) hydrogen bonding density for D = 100 nm, R_0= 0.276 nm, E_m = 1.4 nN/nm^2; (c) initial intermolecular distance for D = 100 nm, n_H= 2 nm^{-2}, E_m = 1.4 nN/nm^2; (d) elastic modulus of matrix material for D = 100 nm, n_H= 2 nm^{-2}, R_0= 0.276 nm.

Figure 6.39 shows the energy dissipated from the system as function of the size of the particle, the hydrogen bond density, the initial intermolecular distance, R_0, and the elastic modulus of the matrix material. In Figure 6.39(a), the volume of the particles is set as 100 nm^3. The number of the particles is inversely proportional to the particle size D. When the size of the particle increases, the energy dissipation significantly decreases. This trend corresponds to results from damping measurements of CNC reinforced PA610 [267] (see Figure 6.40) which show a strong increase in damping ratio of the composite as cellulose filler size decreases, and is due to the increase of the surface area of the interacting surfaces of the filler and the matrix.

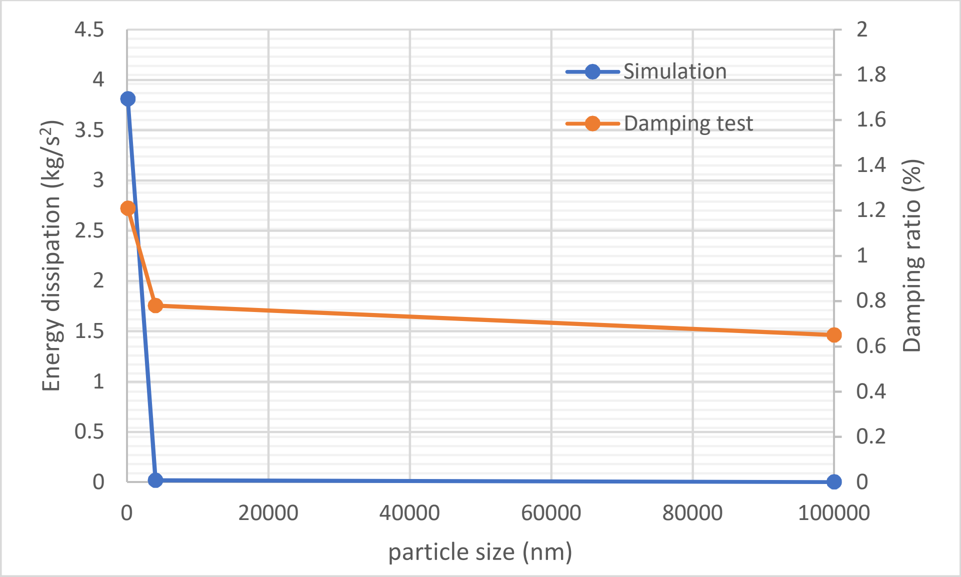

Figure 6.40. Energy dissipation in the simulation (blue curve) and damping ratios from the damping tests (orange curve) vs. particle sizes.

Figure 6.39(b) shows that energy dissipation of the system peaks when H bond density is 2.5 nm^{-2}, and then plateaus as density is increased further. When the hydrogen bonding density is bottom than 2.5 nm^{-2}, there are two general reasons that the energy dissipation is constrained. First, the intermolecular change in state may not occur when the hydrogen bonding density is too low because the condition described in relation to Figure 6.37(a) may not be met. Second, the total kinetic energy of the particle gained during the change in state may be small due to the weak hydrogen bonding strength. As for hydrogen bond density larger than 2.5 nm^{-2}, Figure 6.41 shows two intermolecular force curves at different hydrogen bond densities for the case where the top input amplitude y_T is set to be the same (5 nm) in both cases. It is clear that a smaller hydrogen bond density can result in a smaller intermolecular change in state (from R_b = 0.27 to 1.79 nm) than would a larger density (from R_b = 0.27 to 4.38 nm). However, because of the strength of the intermolecular bonds in the larger density case, the maximum top and bottom intermolecular distance that occurs is 0.282 nm, so the intermolecular change in state at 0.3 nm does not occur. Therefore, energy dissipation is not necessarily maximum for higher bond densities, but rather occurs over an intermediate range for this composite.

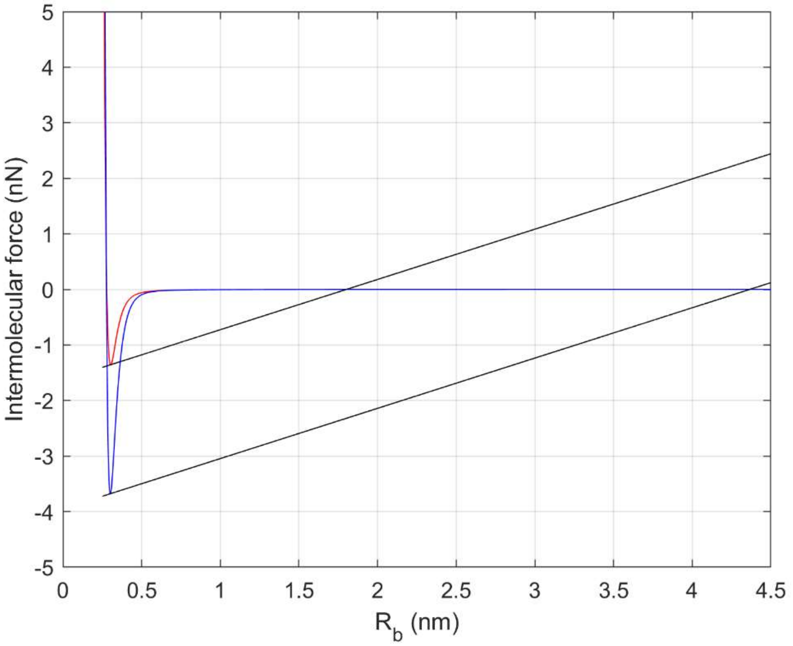

Figure 6.41. Intermolecular forces-distance graph. Two intermolecular forces at hydrogen bonding density: 2 nm^{-2} (red) and 5 nm^{-2} (blue).

Figure 6.39(c) shows the energy loss is significantly bottom for larger initial intermolecular distance R_0, the first point of which in the figure is R_H, the equilibrium distance given in Table 6.4. The decreasing trend of the energy loss is associated with the intermolecular change in state. In case of the same input amplitude of the displacement y_T, the points where intermolecular changes in state can occur are not reached in the case of large initial R_0. Note that they could be reached if the range of y_T were very large. This corresponds with the damping test results in [267], which shows the damping ratio of the composites decreases after moisture in the composites is driven off. The process of drying will increase the free volume between the filler and matrix material [92] so that the intermolecular distance will increase.

To study the effect of relative stiffness of the contacting surfaces on the energy dissipation, the elastic modulus of the matrix material is varied from 0.4 to 1.8 nN/nm^2 in Figure 6.39(d). E_m is varied here for expediency. The range of E_m selected represents E_p/E_m from 81 to 362, which covers a reasonable range of filler/matrix combinations. Energy loss in the system peaks at E_m= 1.2 nN/nm^2 and decreases when the material is either too soft or too stiff. For intermolecular change in state to occur, the total stiffness of the materials (i.e. the k_0 value given in (6.25)) must equal the slope of the total intermolecular force, as depicted in Figure 6.37(a). Thus, the result shows that the blue curve will only intersect the red curve at two points in a specific range of stiffness.

Four parameter studies were conducted in Figure 6.39. A semi-quantitative comparison between the model and the experiment can be made for one of these parameter studies, particle size (Figure 6.39(a)), as was described in Figure 6.40. No comparison can be made with the experiments in this work for the bond density (Figure 6.39(b)) and the matrix material property (Figure 6.39(d)) parameter studies. For the initial intermolecular distance study (Figure 6.39(c)), only qualitative comparison can be made between the simulation and the experiment because it is not possible to measure the intermolecular distance in the actual samples. To show the effect of initial intermolecular distance in the model, the value of R_0 was varied in the simulation, which showed decreasing energy dissipation with increasing R_0. Figure 6.42 gives a depiction of the qualitative relationship between intermolecular distance and experimental results in samples after drying.

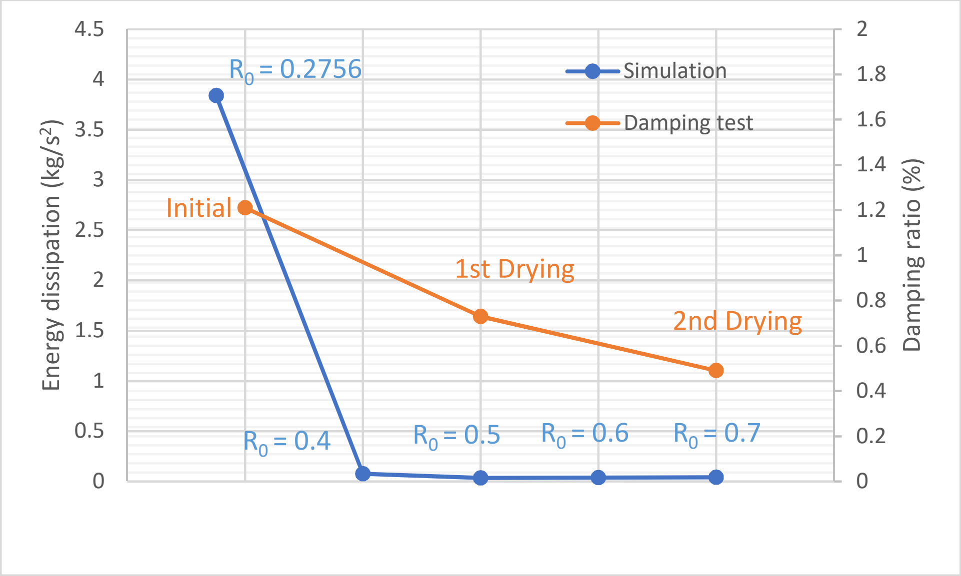

Figure 6.42. Blue curve: energy dissipation in the simulation vs. initial intermolecular distance (nm). Orange curve: damping ratios from the damping tests vs. number of dryings.

The focus of this model is the interfacial interaction of a nanoscale particle filler interacting with a polymer matrix material. It includes the elasticity of the materials based on their measured properties and the interfacial interaction includes Van der Waal and Hydrogen bonding forces. In particular, the focus on hydrogen bonding is based on the known effect of this force to produce large damping [294]. The model is one dimensional, so more complex 3-D effects are neglected. Since the focus of the model is to study the effects of adhesion hysteresis, interfacial slip is assumed to be negligible and so interfacial friction [268] is not included. (This would also extend the model to two-dimensions.)

Compared to other similar adhesion model, the improved model introduced in this paper have several advantages. In [255, 257], both models are based on a massless contacting system with Van der Waals force and a simple elastic force. In contrast, the improved model includes the mass of the particle and hydrogen bonding between the surfaces. In [256], the author shows a model with an elastic force based on the deformation of the smooth contacting surfaces. The improved model in this paper relates the elastic forces to the asperities on the surfaces, which is more close to the AFM experiment results [295].

6.5.7 Conclusion

An improved adhesion model for the filler and matrix contacting surfaces of a particle reinforced composite is proposed. In the case of cellulose reinforced PA610 composites, the elastic force from asperities of the contacting surfaces and intermolecular hydrogen bonding encourage sudden intermolecular change in state. The simulation results show strong relationship between the hydrogen bonding at the interface and increase of energy dissipation that qualitatively corresponds to previously measured damping test results[267]. The energy loss is in negative proportion with the particle size and initial intermolecular distance. Additionally, there are optimal values of the hydrogen bonding density and elastic modulus ratio of the materials that increase the energy loss. The model can be used to design composites that maximize the potential energy loss.

The focus of the present model is to study the effects of adhesion hysteresis and this is conducted using a one-dimensional model. This necessarily neglects the effects of more complex deformations on the damping. Additionally, the contacting materials are assumed to be well-bonded, so interfacial slip [268] is not included. Multiple bonds are included through the effect of bond density per unit area which is not as general as a full molecular dynamics simulation. Nevertheless, despite these limitations, the model captures the interrelated effects of hydrogen bonding and sudden intermolecular changes in state on energy dissipation in a straightforward context, and forms the basis for more general multi-dimensional studies.

Chapter 7 Future Work and Published Work

This chapter covers the description of possible future studies of cellulose reinforced PA610, including testing and modeling.

In chapter 3, tensile test were conducted on cellulose reinforced PA610, PA1010 and PP composites at different rates and temperature. However, the temperature tests were not completely done for the cellulose/PA610 and cellulose/PP composites. In addition, rate tests are needed for cellulose/PP composites. In relation to moisture effects, additional mechanical tests beyond the results given in Figure 3.7, at different temperatures and rates are required to study the behaviors of the materials after moisture absorption.

For the damping testing in chapter 4, damping tests at room temperature were done for the cellulose reinforced PA610 and PP composites. Due to a lack of samples, temperature tests were only conducted for cellulose filled PP and PA610 containing moisture. More temperature tests are need to study the damping properties of cellulose/PA610 in dry condition.

For the final adhesion model (see Figure 6.33(a)), several potential advancements can be made. Firstly, the mass of the surface asperities can be added to the model, which would show the influence of the asperities' dynamics on the intermolecular changes in state. Secondly, the model can be extended into a 2-dimentional model. In this case, the shape of the particles can be implemented so the model can be used to determine the effects such as aspect ratio, which influence stress concentrations [271]. Thirdly, the models were built for cellulose and PA610 without the presence of water molecules, as would occur after moisture absorption. The influence of water molecules on the intermolecular changes in state could be studied in a model including absorbed H_2O which will likely bond to both PA610 and cellulose thereby altering the intermolecular force and elasticity of PA610.

As the current study is done mainly for the cellulose/PA610 composites, more systematic study can be done for other similar material such as cellulose reinforced PA46 composites, which have higher hydrogen bonding density at the interface. Changing different cellulose fillers is also needed to study the filler effects. For example, the CNC filler used in this dissertation was manufactured by spray dried process. Freeze dried processed CNC may have different shapes of the particles than those of spray dried CNC [296]. Therefore, it is worth studying the effects of particle shapes on the mechanical and dynamic properties by replacing spray dried CNC with freeze dried ones. In addition, study can also be conducted on the cellulose particles coated by some hydrophobic materials, which reduces the hydrogen bonding at the interfaces and improves the dispersion of the particles.

A List of my presentations and publications is summarized in Table 7.1:

Table 7.1. List of presentations and publications

Work name	Comments
A paper for the damping results has been submitted and under review. Tian Y, Kim W, Elise K, Kiziltas A, Mielewski D, Argento A. Damping of micro- and nanocellulose reinforced PA610 composites and influences of moisture absorption. Materials Today 2022.	The paper is currently under revision and will be resubmitted in about one week.

A paper for the modeling work has been submitted. Tian Y, Kim W, Kiziltas A, Mielewski D, Argento A. Effects of Interfacial Dynamics on the Damping of Biocomposites Scientific Reports 2022.	The paper is under first review
Mechanical and damping test results were presented at SPE Automotive Composites Conference & Exhibition. Tian, Y., Kiziltas, A., Kim, W., Mielewski, D. and Argento, A. Manufacture and Damping of Nanocellulose-Nylon Composites. Society of Plastics Engineers, 18th Annual Conference-Composites: Solutions for a Multi-Material World, Novi Michigan. September 2018.	Podium presentation.
Poster presentations were made in 2017 at at SPE Automotive Composites Conference & Exhibition. Tian, Y., Kiziltas, A., Kim, W., Mielewski, D. and Argento, A. Nanoscale mechanisms of dynamic response in nanocellulose biocomposites. Society of Plastics Engineers, 17th Annual Conference-Composites: Solutions	Poster presentation.

for a Multi-Material World, Novi Michigan. September 6-8, 2017.	
Poster presentations were made in 2022 at SPE Plastics in Electric and Autonomous Vehicles conference. Tian, Y., Kiziltas, A., Mielewski, D., Kim, W. and Argento, A. “CNC reinforced PA610 composites: damping enhancement and modeling.” Plastics in electric and autonomous vehicles, SPE, May 1-4, 2022, Troy, MI.	Poster presentation.

Appendix A

The coordinates and deformations of the springs are related to the intermolecular distance through simple geometry of the model in Figure 6.33(a). For the top part of the model above the mass:

$$y - y_T(t) = (\Delta h_1 - \Delta h_{01}) + (\Delta h_3 - \Delta h_{03}) + (R_t - R_0) \tag{A.1}$$

where R_0, R_t are the initial and current intermolecular distances, respectively, Δh_1 and Δh_3 are the deformations of the elastic elements of the particle and top matrix material, respectively. Δh_{01} and Δh_{03} are the initial deformation of the elastic elements for the particle and top matrix material, respectively. Note that $R_0,\ \Delta h_{01},\ \Delta h_{03}$ are given constants and $y_T(t)$ is a prescribed function. Equation (A.1) can be simplified as:

$$R_t = R_0 + \Delta h_{01} + \Delta h_{03} - \Delta h_1 - \Delta h_3 + y - y_T(t) \tag{A.2}$$

Equation (A.2) relates the current intermolecular distance to the current deformations of the elastic elements. Similarly, for the bottom part of the model, the relationship for the intermolecular distance R_b is:

$$R_b = R_0 + \Delta h_{02} + \Delta h_{04} - \Delta h_2 - \Delta h_4 - y \tag{A.3}$$

Where, Δh_{02} and Δh_{04} are the initial deformation of the elastic elements for the particle and bottom matrix material, respectively. Δh_2 and Δh_4 are the current deformation of the elastic elements of the particle and the bottom matrix material, respectively.

Appendix B

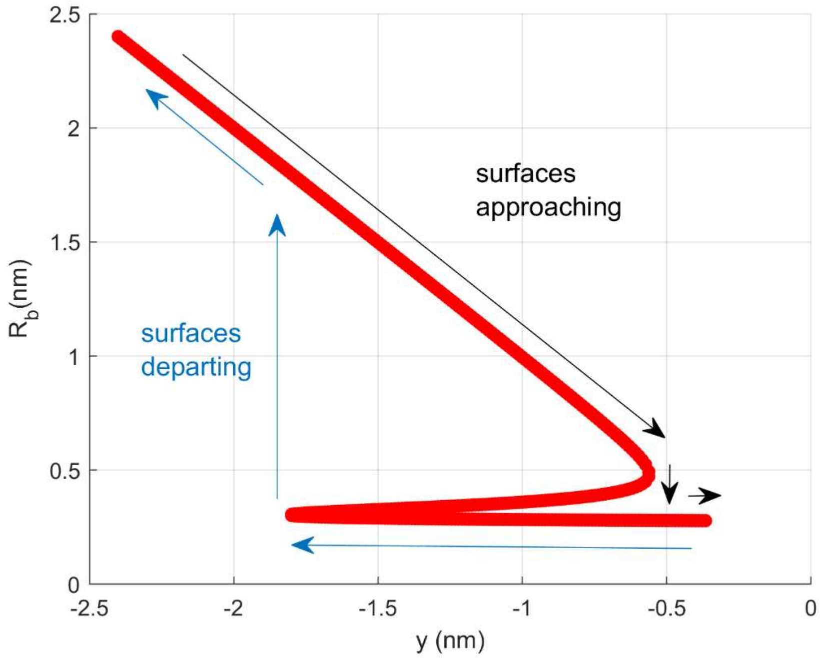

Figure B.1. Intermolecular distance, R_b, of equation (6.27) vs the displacement of the particle y.

Figure B.1 describes the locus of roots R_b of equation (6.27). Since the materials of the top contacting surfaces are the same as the bottom ones, the shape of the root graphs for R_b and R_t are identical. Each point on the curve represents a root of equation (6.27) at a time step. To better explain how the roots are selected, the initial intermolecular distance is set to be 0.276 nm. Note that the positive direction of y is downward. As y deceases from 0, the intermolecular distance R_b follows the root curve until y reaches -1.79 nm, where R_b=0.3 nm. When y moves further to the left beyond this point -1.79 nm, the continuing root R_b disappears and suddenly changes to 1.8 nm. It then follows the root curve from this point. This process is indicated by the direction of the blue arrows. A similar process occurs when the surfaces approach each other, which is shown in the direction of the black arrows. The root results are used in the model to determine the intermolecular force.

Appendix C

In Figure C.1, the initial positions of the donor of the hydrogen atom, the hydrogen atom, and the acceptor of hydrogen atom are respectively shown as A, B, C, and are connected by solid lines. θ, α, β are the angles between these atoms. L_{ab} and L_{bc} are the initial bond lengths between the atoms at A, B, C, as shown. R_i is the initial hydrogen bonding length. When the hydrogen bond increases to current length R, the atom at C moves to current position D (assuming A is fixed). For the case of adhesion, the lateral movement of atom C as it moves to point D will not be considered.

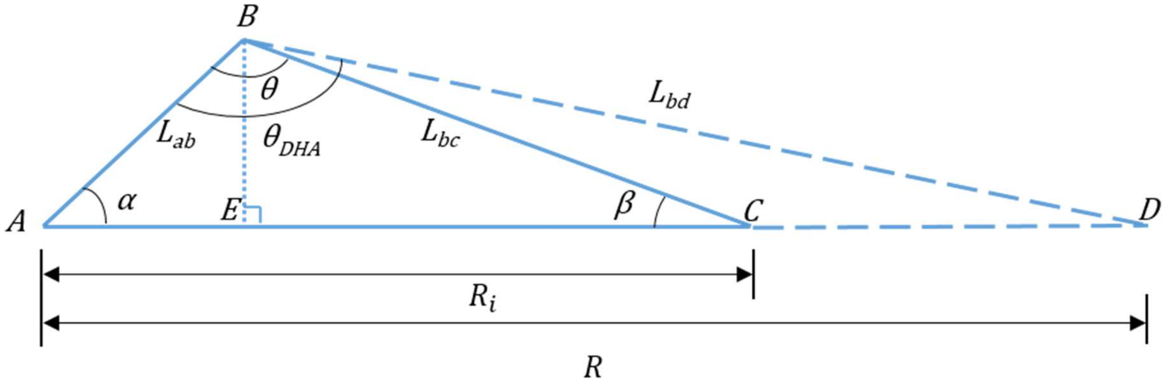

Figure C.1. Schematic for the hydrogen bonding angle, θ_{DHA}.

The relationship between the angles at the initial position is:

$$\frac{R_i}{sin\theta} = \frac{L_{ab}}{sin\beta} = \frac{L_{bc}}{sin\alpha} \tag{C.1}$$

The relationship between the angle θ_{DHA} and side lengths at the current position is:

$$cos\theta_{DHA} = \frac{L_{ab}^2 + L_{bd}^2 - R^2}{2L_{ab}L_{bd}} \tag{C.2}$$

L_{bd} is determined by:

$$L_{bd} = \sqrt{(L_{ab}sin\alpha)^2 + (R - L_{ab}cos\alpha)^2} \tag{C.3}$$

Using equation (C.1)-(C.3), $cos\theta_{DHA}$ can be obtained as:

$$cos\theta_{DHA} = \frac{L_{ab}^2 + (sin\alpha \cdot L_{ab})^2 + (R - cos\alpha \cdot L_{ab})^2 - R^2}{2L_{ab}\sqrt{(sin\alpha \cdot L_{ab})^2 + (R - cos\alpha \cdot L_{ab})^2}} \tag{C.4}$$

Appendix D

Table D.1. List of abbreviations

Abbreviation	**Definition**
CNC	Nanocrystalline cellulose
WF	Wood fiber
PF	Plant fiber
MCC	Microcrystalline cellulose
MFC	Cellulose micro fibrils
NFC	Cellulose nano fibrils
TCNC	Tunicate nanocrystalline cellulose
AC	Algae cellulose particles
BC	Bacterial cellulose particles
MWCNT	Multiwalled carbon nanotube
CTE	Coefficient of thermal expansion
TGA	Thermogravimetric analysis
FEA	Finite element analysis
AFM	Atomic force microscopy
PA	Polyamides
HMDA	Hexamethylene diamine

DMDA	Decamethylene diamine
DMAc	N-dimethylacetamide
PP	Polypropylene
PLA	Polylactic acid
PHB	Poly(3-hydroxylbutyrat)
PBAT	Poly(butylene adipate-co-terephtalate)
PU	Polyurethane
PVA	Polyvinyl alcohol
PAM	Polyacrylamide
EAA	Poly(-ethylene-co-acrylic acid)
DAPA	Dimer fatty acid-based polyamides
SWCNT	Single-walled carbon nanotube
DMA	Dynamic mechanical analysis
PDMS	Poly(dimethylsiloxanes)
PT	Prandtl-Tomlinson
FK	Frenkel-Kontorova
FKT	Frenkel-Kontorova-Tomlinson
SEM	Scanning electron microscopy

Bibliography

[1] J. O. Metzger and A. Hüttermann, "Sustainable global energy supply based on lignocellulosic biomass from afforestation of degraded areas," *Naturwissenschaften,* vol. 96, pp. 279-288, 2009.

[2] G. D. Saratale and S. E. Oh, "Lignocellulosics to ethanol: The future of the chemical and energy industry," *African Journal of Biotechnology,* vol. 11, pp. 1002-1013, 2012.

[3] S. Elazzouzi-Hafraoui, Y. Nishiyama, J.-L. Putaux, L. Heux, F. Dubreuil, and C. Rochas, "The shape and size distribution of crystalline nanoparticles prepared by acid hydrolysis of native cellulose," *Biomacromolecules,* vol. 9, pp. 57-65, 2008.

[4] T. Saito, Y. Nishiyama, J.-L. Putaux, M. Vignon, and A. Isogai, "Homogeneous suspensions of individualized microfibrils from TEMPO-catalyzed oxidation of native cellulose," *Biomacromolecules,* vol. 7, pp. 1687-1691, 2006.

[5] N. L. Garcia de Rodriguez, W. Thielemans, and A. Dufresne, "Sisal cellulose whiskers reinforced polyvinyl acetate nanocomposites," *Cellulose,* vol. 13, pp. 261-270, 2006.

[6] X. Cao, H. Dong, and C. M. Li, "New nanocomposite materials reinforced with flax cellulose nanocrystals in waterborne polyurethane," *Biomacromolecules,* vol. 8, pp. 899-904, 2007.

[7] H. Lee, S. B. A. Hamid, and S. Zain, "Conversion of lignocellulosic biomass to nanocellulose: structure and chemical process," *The Scientific World Journal,* vol. 2014, 2014.

[8] H. Yamamoto and F. Horn, "In Situ crystallization of bacterial cellulose I. Influences of polymeric additives, stirring and temperature on the formation celluloses I α and I β as revealed by cross polarization/magic angle spinning (CP/MAS) 13C NMR spectroscopy," *Cellulose,* vol. 1, pp. 57-66, 1994.

[9] N.-H. Kim, W. Herth, R. Vuong, and H. Chanzy, "The cellulose system in the cell wall ofMicrasterias," *Journal of structural biology,* vol. 117, pp. 195-203, 1996.

[10] S. J. Hanley, J.-F. Revol, L. Godbout, and D. G. Gray, "Atomic force microscopy and transmission electron microscopy of cellulose from Micrasterias denticulata; evidence for a chiral helical microfibril twist," *Cellulose,* vol. 4, pp. 209-220, 1997.

[11] T. Imai and J. Sugiyama, "Nanodomains of Iα and Iβ cellulose in algal microfibrils," *Macromolecules,* vol. 31, pp. 6275-6279, 1998.

[12] S. Kimura and T. Itoh, "Cellulose synthesizing terminal complexes in the ascidians," *Cellulose,* vol. 11, pp. 377-383, 2004.

[13] W. Helbert, Y. Nishiyama, T. Okano, and J. Sugiyama, "Molecular imaging ofhalocynthia papillosacellulose," *Journal of structural biology,* vol. 124, pp. 42-50, 1998.

[14] S. Kimura and T. Itoh, "New cellulose synthesizing complexes (terminal complexes) involved in animal cellulose biosynthesis in the tunicateMetandrocarpa uedai," *Protoplasma,* vol. 194, pp. 151-163, 1996.

[15] R. J. Moon, A. Martini, J. Nairn, J. Simonsen, and J. Youngblood, "Cellulose nanomaterials review: structure, properties and nanocomposites," *Chemical Society Reviews,* vol. 40, pp. 3941-3994, 2011.

[16] E. Sjostrom, *Wood chemistry: fundamentals and applications*: Gulf professional publishing, 1993.

[17] A. C. O'sullivan, "Cellulose: the structure slowly unravels," *Cellulose,* vol. 4, pp. 173-207, 1997.

[18] M. A. S. Azizi Samir, F. Alloin, and A. Dufresne, "Review of recent research into cellulosic whiskers, their properties and their application in nanocomposite field," *Biomacromolecules,* vol. 6, pp. 612-626, 2005.

[19] E. Debzi, H. Chanzy, J. Sugiyama, P. Tekely, and G. Excoffier, "The Iα→ Iβ transformation of highly crystalline cellulose by annealing in various mediums," *Macromolecules,* vol. 24, pp. 6816-6822, 1991.

[20] H. Yamamoto and F. Horii, "CPMAS carbon-13 NMR analysis of the crystal transformation induced for Valonia cellulose by annealing at high temperatures," *Macromolecules,* vol. 26, pp. 1313-1317, 1993.

[21] Y. Nishiyama, P. Langan, and H. Chanzy, "Crystal structure and hydrogen-bonding system in cellulose Iβ from synchrotron X-ray and neutron fiber diffraction," *Journal of the American Chemical Society,* vol. 124, pp. 9074-9082, 2002.

[22] Y. Nishiyama, J. Sugiyama, H. Chanzy, and P. Langan, "Crystal structure and hydrogen bonding system in cellulose Iα from synchrotron X-ray and neutron fiber diffraction," *Journal of the American Chemical Society,* vol. 125, pp. 14300-14306, 2003.

[23] D. Klemm, B. Heublein, H. P. Fink, and A. Bohn, "Cellulose: fascinating biopolymer and sustainable raw material," *Angewandte chemie international edition,* vol. 44, pp. 3358-3393, 2005.

[24] P. Langan, Y. Nishiyama, and H. Chanzy, "X-ray structure of mercerized cellulose II at 1 Å resolution," *Biomacromolecules,* vol. 2, pp. 410-416, 2001.

[25] R. N. Goldberg, J. Schliesser, A. Mittal, S. R. Decker, A. F. L. Santos, V. L. Freitas*, et al.*, "A thermodynamic investigation of the cellulose allomorphs: Cellulose (am), cellulose Iβ (cr), cellulose II (cr), and cellulose III (cr)," *The Journal of Chemical Thermodynamics,* vol. 81, pp. 184-226, 2015.

[26] S. P. Chundawat, G. Bellesia, N. Uppugundla, L. da Costa Sousa, D. Gao, A. M. Cheh*, et al.*, "Restructuring the crystalline cellulose hydrogen bond network enhances its depolymerization rate," *Journal of the American Chemical Society,* vol. 133, pp. 11163-11174, 2011.

[27] L. Loeb and L. Segal, "Preparation of cotton cellulose IV from cotton cellulose III," *Journal of Polymer Science,* vol. 14, pp. 121-123, 1954.

[28] A. Alemdar and M. Sain, "Isolation and characterization of nanofibers from agricultural residues–Wheat straw and soy hulls," *Bioresource technology,* vol. 99, pp. 1664-1671, 2008.

[29] M. A. Hubbe, O. J. Rojas, L. A. Lucia, and M. Sain, "Cellulosic nanocomposites: a review," *BioResources,* vol. 3, pp. 929-980, 2008.

[30] O. Van den Berg, J. R. Capadona, and C. Weder, "Preparation of homogeneous dispersions of tunicate cellulose whiskers in organic solvents," *Biomacromolecules,* vol. 8, pp. 1353-1357, 2007.

[31] M. Iguchi, S. Yamanaka, and A. Budhiono, "Bacterial cellulose—a masterpiece of nature's arts," *Journal of materials science,* vol. 35, pp. 261-270, 2000.

[32] R. K. Johnson, A. Zink-Sharp, S. H. Renneckar, and W. G. Glasser, "A new bio-based nanocomposite: fibrillated TEMPO-oxidized celluloses in hydroxypropylcellulose matrix," *Cellulose,* vol. 16, pp. 227-238, 2009.

[33] Y. Habibi, L. A. Lucia, and O. J. Rojas, "Cellulose nanocrystals: chemistry, self-assembly, and applications," *Chemical reviews,* vol. 110, pp. 3479-3500, 2010.

[34] D. Bondeson, A. Mathew, and K. Oksman, "Optimization of the isolation of nanocrystals from microcrystalline cellulose by acid hydrolysis," *Cellulose,* vol. 13, pp. 171-180, 2006.

[35] S. Levis and P. Deasy, "Production and evaluation of size reduced grades of microcrystalline cellulose," *International journal of pharmaceutics,* vol. 213, pp. 13-24, 2001.

[36] C. Rondeau-Mouro, B. Bouchet, B. Pontoire, P. Robert, J. Mazoyer, and A. Buleon, "Structural features and potential texturising properties of lemon and maize cellulose microfibrils," *Carbohydrate Polymers,* vol. 53, pp. 241-252, 2003.

[37] A. Dufresne, J. Y. Cavaillé, and M. R. Vignon, "Mechanical behavior of sheets prepared from sugar beet cellulose microfibrils," *Journal of applied polymer science,* vol. 64, pp. 1185-1194, 1997.

[38] S. Iwamoto, K. Abe, and H. Yano, "The effect of hemicelluloses on wood pulp nanofibrillation and nanofiber network characteristics," *Biomacromolecules,* vol. 9, pp. 1022-1026, 2008.

[39] T. Saito, M. Hirota, N. Tamura, S. Kimura, H. Fukuzumi, L. Heux*, et al.*, "Individualization of nano-sized plant cellulose fibrils by direct surface carboxylation using TEMPO catalyst under neutral conditions," *Biomacromolecules,* vol. 10, pp. 1992-1996, 2009.

[40] A. Ishikawa, T. Okano, and J. Sugiyama, "Fine structure and tensile properties of ramie fibres in the crystalline form of cellulose I, II, IIII and IVI," *Polymer,* vol. 38, pp. 463-468, 1997.

[41] S. Iwamoto, W. Kai, A. Isogai, and T. Iwata, "Elastic modulus of single cellulose microfibrils from tunicate measured by atomic force microscopy," *Biomacromolecules,* vol. 10, pp. 2571-2576, 2009.

[42] J.-F. Revol, "On the cross-sectional shape of cellulose crystallites in Valonia ventricosa," *Carbohydrate Polymers,* vol. 2, pp. 123-134, 1982.

[43] J. Sugiyama, H. Harada, Y. Fujiyoshi, and N. Uyeda, "Lattice images from ultrathin sections of cellulose microfibrils in the cell wall of Valonia macrophysa Kütz," *Planta,* vol. 166, pp. 161-168, 1985.

[44] C. Tokoh, K. Takabe, M. Fujita, and H. Saiki, "Cellulose synthesized by Acetobacter xylinum in the presence of acetyl glucomannan," *Cellulose,* vol. 5, pp. 249-261, 1998.

[45] D. Batchelder and D. Bloor, "Strain dependence of the vibrational modes of a diacetylene crystal," *Journal of Polymer Science: Polymer Physics Edition,* vol. 17, pp. 569-581, 1979.

[46] R. Young, "Monitoring deformation processes in high-performance fibres using Raman spectroscopy," *Journal of the Textile Institute,* vol. 86, pp. 360-381, 1995.

[47] S. Eichhorn, R. Young, and W.-Y. Yeh, "Deformation processes in regenerated cellulose fibers," *Textile research journal,* vol. 71, pp. 121-129, 2001.

[48] S. Eichhorn, M. Hughes, R. Snell, and L. Mott, "Strain induced shifts in the Raman spectra of natural cellulose fibers," *Journal of materials science letters,* vol. 19, pp. 721-723, 2000.

[49] M. Monclus, T. Young, and D. Di Maio, "AFM indentation method used for elastic modulus characterization of interfaces and thin layers," *Journal of Materials Science,* vol. 45, pp. 3190-3197, 2010.

[50] I. Diddens, B. Murphy, M. Krisch, and M. Müller, "Anisotropic elastic properties of cellulose measured using inelastic X-ray scattering," *Macromolecules,* vol. 41, pp. 9755-9759, 2008.

[51] M. Matsuo, C. Sawatari, Y. Iwai, and F. Ozaki, "Effect of orientation distribution and crystallinity on the measurement by X-ray diffraction of the crystal lattice moduli of cellulose I and II," *Macromolecules,* vol. 23, pp. 3266-3275, 1990.

[52] S. Eichhorn and G. Davies, "Modelling the crystalline deformation of native and regenerated cellulose," *Cellulose,* vol. 13, pp. 291-307, 2006.

[53] S. J. Eichhorn, R. J. Young, and G. R. Davies, "Modeling crystal and molecular deformation in regenerated cellulose fibers," *Biomacromolecules,* vol. 6, pp. 507-513, 2005.

[54] M. Grunert and W. T. Winter, "Nanocomposites of cellulose acetate butyrate reinforced with cellulose nanocrystals," *Journal of Polymers and the Environment,* vol. 10, pp. 27-30, 2002.

[55] S. J. Eichhorn, A. Dufresne, M. Aranguren, N. Marcovich, J. Capadona, S. J. Rowan*, et al.*, "Current international research into cellulose nanofibres and nanocomposites," *Journal of materials science,* vol. 45, pp. 1-33, 2010.

[56] S. Eichhorn, C. Baillie, N. Zafeiropoulos, L. Mwaikambo, M. Ansell, A. Dufresne*, et al.*, "Current international research into cellulosic fibres and composites," *Journal of materials Science,* vol. 36, pp. 2107-2131, 2001.

[57] S. Eichhorn, J. Sirichaisit, and R. Young, "Deformation mechanisms in cellulose fibres, paper and wood," *Journal of Materials Science,* vol. 36, pp. 3129-3135, 2001.

[58] S. Eichhorn and R. Young, "The Young's modulus of a microcrystalline cellulose," *Cellulose,* vol. 8, pp. 197-207, 2001.

[59] R. Rusli and S. J. Eichhorn, "Determination of the stiffness of cellulose nanowhiskers and the fiber-matrix interface in a nanocomposite using Raman spectroscopy," *Applied Physics Letters,* vol. 93, p. 033111, 2008.

[60] R. R. Lahiji, X. Xu, R. Reifenberger, A. Raman, A. Rudie, and R. J. Moon, "Atomic force microscopy characterization of cellulose nanocrystals," *Langmuir,* vol. 26, pp. 4480-4488, 2010.

[61] M. T. Postek, A. Vladár, J. Dagata, N. Farkas, B. Ming, R. Wagner*, et al.*, "Development of the metrology and imaging of cellulose nanocrystals," *Measurement Science and Technology,* vol. 22, p. 024005, 2010.

[62] G. Guhados, W. Wan, and J. L. Hutter, "Measurement of the elastic modulus of single bacterial cellulose fibers using atomic force microscopy," *Langmuir,* vol. 21, pp. 6642-6646, 2005.

[63] Y.-C. Hsieh, H. Yano, M. Nogi, and S. Eichhorn, "An estimation of the Young's modulus of bacterial cellulose filaments," *Cellulose,* vol. 15, pp. 507-513, 2008.

[64] S. Reiling and J. Brickmann, "Theoretical investigations on the structure and physical properties of cellulose," *Macromolecular theory and simulations,* vol. 4, pp. 725-743, 1995.

[65] K. Tashiro and M. Kobayashi, "Theoretical evaluation of three-dimensional elastic constants of native and regenerated celluloses: role of hydrogen bonds," *Polymer,* vol. 32, pp. 1516-1526, 1991.

[66] M. F. Ashby, R. W. Messler, R. Asthana, E. P. Furlani, R. Smallman, A. Ngan*, et al.*, *Engineering materials and processes desk reference*: Butterworth-Heinemann, 2009.

[67] W. D. Callister and D. G. Rethwisch, *Materials science and engineering: an introduction* vol. 9: Wiley New York, 2018.

[68] M.-F. Yu, O. Lourie, M. J. Dyer, K. Moloni, T. F. Kelly, and R. S. Ruoff, "Strength and breaking mechanism of multiwalled carbon nanotubes under tensile load," *Science,* vol. 287, pp. 637-640, 2000.

[69] L. Petersson, I. Kvien, and K. Oksman, "Structure and thermal properties of poly (lactic acid)/cellulose whiskers nanocomposite materials," *Composites Science and Technology,* vol. 67, pp. 2535-2544, 2007.

[70] H. Fukuzumi, T. Saito, T. Iwata, Y. Kumamoto, and A. Isogai, "Transparent and high gas barrier films of cellulose nanofibers prepared by TEMPO-mediated oxidation," *Biomacromolecules,* vol. 10, pp. 162-165, 2009.

[71] K. Das, D. Ray, N. Bandyopadhyay, and S. Sengupta, "Study of the properties of microcrystalline cellulose particles from different renewable resources by XRD, FTIR, nanoindentation, TGA and SEM," *Journal of Polymers and the Environment,* vol. 18, pp. 355-363, 2010.

[72] A. N. Nakagaito, M. Nogi, and H. Yano, "Displays from transparent films of natural nanofibers," *MRS bulletin,* vol. 35, pp. 214-218, 2010.

[73] M. Nogi, S. Ifuku, K. Abe, K. Handa, A. N. Nakagaito, and H. Yano, "Fiber-content dependency of the optical transparency and thermal expansion of bacterial nanofiber reinforced composites," *Applied Physics Letters,* vol. 88, p. 133124, 2006.

[74] K. Syverud and P. Stenius, "Strength and barrier properties of MFC films," *Cellulose,* vol. 16, pp. 75-85, 2009.

[75] S. Kalia, B. Kaith, and I. Kaur, "Pretreatments of natural fibers and their application as reinforcing material in polymer composites—a review," *Polymer Engineering & Science,* vol. 49, pp. 1253-1272, 2009.

[76] R. Agrawal, N. Saxena, K. Sharma, S. Thomas, and M. Sreekala, "Activation energy and crystallization kinetics of untreated and treated oil palm fibre reinforced phenol formaldehyde composites," *Materials Science and Engineering: A,* vol. 277, pp. 77-82, 2000.

[77] I. Van de Weyenberg, J. Ivens, A. De Coster, B. Kino, E. Baetens, and I. Verpoest, "Influence of processing and chemical treatment of flax fibres on their composites," *Composites science and technology,* vol. 63, pp. 1241-1246, 2003.

[78] M. Z. Rong, M. Q. Zhang, Y. Liu, G. C. Yang, and H. M. Zeng, "The effect of fiber treatment on the mechanical properties of unidirectional sisal-reinforced epoxy composites," *Composites Science and technology,* vol. 61, pp. 1437-1447, 2001.

[79] K. Joseph, L. Mattoso, R. Toledo, S. Thomas, L. De Carvalho, L. Pothen*, et al.*, "Natural fiber reinforced thermoplastic composites," *Natural polymers and agrofibers composites,* vol. 159, 2000.

[80] J. Gassan and A. K. Bledzki, "Alkali treatment of jute fibers: relationship between structure and mechanical properties," *Journal of Applied Polymer Science,* vol. 71, pp. 623-629, 1999.

[81] M. Sreekala, M. Kumaran, S. Joseph, M. Jacob, and S. Thomas, "Oil palm fibre reinforced phenol formaldehyde composites: influence of fibre surface modifications on the mechanical performance," *Applied Composite Materials,* vol. 7, pp. 295-329, 2000.

[82] D. Ray, B. K. Sarkar, A. Rana, and N. R. Bose, "Effect of alkali treated jute fibres on composite properties," *Bulletin of materials science,* vol. 24, pp. 129-135, 2001.

[83] D. Dupeyre and M. Vignon, "Fibres from semi-retted hemp bundles by steam explosion treatment," *Biomass and Bioenergy,* vol. 14, pp. 251-260, 1998.

[84] B. Wang, S. Panigrahi, L. Tabil, and W. Crerar, "Pre-treatment of flax fibers for use in rotationally molded biocomposites," *Journal of reinforced plastics and composites,* vol. 26, pp. 447-463, 2007.

[85] S. Kamel, N. Ali, K. Jahangir, S. Shah, and A. El-Gendy, "Pharmaceutical significance of cellulose: A review," *Express Polym Lett,* vol. 2, pp. 758-778, 2008.

[86] J. Megiatto, Jackson D, W. Hoareau, C. Gardrat, E. Frollini, and A. Castellan, "Sisal fibers: surface chemical modification using reagent obtained from a renewable source; characterization of hemicellulose and lignin as model study," *Journal of agricultural and food chemistry,* vol. 55, pp. 8576-8584, 2007.

[87] Z. Dominkovics, L. Dányádi, and B. Pukanszky, "Surface modification of wood flour and its effect on the properties of PP/wood composites," *Composites Part A: Applied Science and Manufacturing,* vol. 38, pp. 1893-1901, 2007.

[88] H. Alamri and I. M. Low, "Mechanical properties and water absorption behaviour of recycled cellulose fibre reinforced epoxy composites," *Polymer testing,* vol. 31, pp. 620-628, 2012.

[89] Y. Wan, H. Luo, F. He, H. Liang, Y. Huang, and X. Li, "Mechanical, moisture absorption, and biodegradation behaviours of bacterial cellulose fibre-reinforced starch biocomposites," *Composites Science and Technology,* vol. 69, pp. 1212-1217, 2009.

[90] P. Penjumras, R. A. Rahman, R. A. Talib, and K. Abdan, "Mechanical properties and water absorption behaviour of durian rind cellulose reinforced poly (lactic acid) biocomposites," *Int J Sci Engg Tech,* vol. 5, pp. 343-349, 2015.

[91] D. Ciolacu, F. Ciolacu, and V. I. Popa, "Amorphous cellulose—structure and characterization," *Cellulose chemistry and technology,* vol. 45, p. 13, 2011.

[92] C. J. Tsenoglou, S. Pavlidou, and C. D. Papaspyrides, "Evaluation of interfacial relaxation due to water absorption in fiber–polymer composites," *Composites Science and Technology,* vol. 66, pp. 2855-2864, 2006/12/01/ 2006.

[93] V. P. Swapna, V. S. Abhisha, and R. Stephen, "Polymer/polyhedral oligomeric silsesquioxane nanocomposite membranes for pervaporation," in *Polymer nanocomposite membranes for pervaporation*, ed: Elsevier, 2020, pp. 201-229.

[94] H. Matsumura, J. Sugiyama, and W. G. Glasser, "Cellulosic nanocomposites. I. Thermally deformable cellulose hexanoates from heterogeneous reaction," *Journal of Applied Polymer Science,* vol. 78, pp. 2242-2253, 2000.

[95] A. Alhuthali, I. M. Low, and C. Dong, "Characterisation of the water absorption, mechanical and thermal properties of recycled cellulose fibre reinforced vinyl-ester eco-nanocomposites," *Composites Part B: Engineering,* vol. 43, pp. 2772-2781, 2012.

[96] Y. Lu, L. Weng, and X. Cao, "Morphological, thermal and mechanical properties of ramie crystallites—reinforced plasticized starch biocomposites," *Carbohydrate polymers,* vol. 63, pp. 198-204, 2006.

[97] Y. Zare, K. Y. Rhee, and D. Hui, "Influences of nanoparticles aggregation/agglomeration on the interfacial/interphase and tensile properties of nanocomposites," *Composites Part B: Engineering,* vol. 122, pp. 41-46, 2017.

[98] R. Rahman, J. Foster, and A. Haque, "Molecular dynamics simulation and characterization of graphene–cellulose nanocomposites," *The Journal of Physical Chemistry A,* vol. 117, pp. 5344-5353, 2013.

[99] F. Narita, Y. Wang, H. Kurita, and M. Suzuki, "Multi-scale analysis and testing of tensile behavior in polymers with randomly oriented and agglomerated cellulose nanofibers," *Nanomaterials,* vol. 10, p. 700, 2020.

[100] V. S. Romanov, S. V. Lomov, I. Verpoest, and L. Gorbatikh, "Modelling evidence of stress concentration mitigation at the micro-scale in polymer composites by the addition of carbon nanotubes," *Carbon,* vol. 82, pp. 184-194, 2015.

[101] W. G. Glasser, R. Taib, R. K. Jain, and R. Kander, "Fiber-reinforced cellulosic thermoplastic composites," *Journal of Applied Polymer Science,* vol. 73, pp. 1329-1340, 1999.

[102] D. E. Brushwood, "Effects of heating on chemical and physical properties and processing quality of cotton," *Textile Research Journal,* vol. 58, pp. 309-317, 1988.

[103] S. Zeronian, "Heat-Induced Changes in the Properties of Cotton Fibers, in “Cellulose Chemistry and Technology," JC Arthur, Jr., Ed., ACS Symposium Series 48, American Chemical Society, Washington, DC," 1977.

[104] J. Gassan and A. K. Bledzki, "Thermal degradation of flax and jute fibers," *Journal of Applied Polymer Science,* vol. 82, pp. 1417-1422, 2001.

[105] B. Herzog, M. I. Kohan, S. A. Mestemacher, R. U. Pagilagan, and K. Redmond, "Polyamides," *Ullmann's Encyclopedia of Industrial Chemistry,* 2000.

[106] W. H. Carothers, "Studies on polymerization and ring formation. I. An introduction to the general theory of condensation polymers," *Journal of the American Chemical Society,* vol. 51, pp. 2548-2559, 1929.

[107] M. Winnacker and B. Rieger, "Biobased polyamides: recent advances in basic and applied research," *Macromolecular rapid communications,* vol. 37, pp. 1391-1413, 2016.

[108] C. V. Stevens, *Bio-based plastics: materials and applications*: John Wiley & Sons, 2013.

[109] J. A. Brydson, *Plastics materials*: Elsevier, 1999.

[110] X. Zhang, X. L. Li, D. Wang, Z. Yin, and J. Yin, "Morphology, thermal behavior, and mechanical properties of PA1010/PP and PA 1010/PP-g-GMA blends," *Journal of applied polymer science,* vol. 64, pp. 1489-1498, 1997.

[111] S. Bandi and D. A. Schiraldi, "Glass Transition Behavior of Clay Aerogel/Poly(vinyl alcohol) Composites," *Macromolecules,* vol. 39, pp. 6537-6545, 2006/09/01 2006.

[112] J. Jackle, "Models of the glass transition," *Reports on Progress in Physics,* vol. 49, p. 171, 1986.

[113] J. Zimmerman and M. I. Kohan, "Nylon–selected topics," *Journal of Polymer Science Part A: Polymer Chemistry,* vol. 39, pp. 2565-2570, 2001.

[114] E. Roerdink and J. Warnier, "Preparation and properties of high molar mass nylon-4, 6: a new development in nylon polymers," *Polymer,* vol. 26, pp. 1582-1588, 1985.

[115] G. Gao, J. Wang, J. Yin, X. Yu, R. Ma, X. Tang*, et al.*, "Rheological, thermal, and morphological properties of ABS–PA1010 blends," *Journal of applied polymer science,* vol. 72, pp. 683-688, 1999.

[116] D. Glasscock, W. Atolino, G. Kozielski, and M. Martens, "High performance polyamides fulfill demanding requirements for automotive thermal management components," *Dupont engineering polymers,* 2008.

[117] J. Wesołowski and K. Płachta, "The polyamide market," *Fibres & textiles in eastern Europe,* 2016.

[118] R. E. Lyon and M. L. Janssens, "Polymer flammability," United States. Federal Aviation Administration. Office of Aviation Research2005.

[119] K. Oksman and M. Sain, *Cellulose nanocomposites: processing, characterization and properties*: American Chemical Society (ACS), 2005.

[120] G. Siqueira, J. Bras, and A. Dufresne, "Cellulosic bionanocomposites: a review of preparation, properties and applications," *Polymers,* vol. 2, pp. 728-765, 2010.

[121] F. D'Acierno, W. Y. Hamad, C. A. Michal, and M. J. MacLachlan, "Thermal degradation of cellulose filaments and nanocrystals," *Biomacromolecules,* vol. 21, pp. 3374-3386, 2020.

[122] K. Oksman, A. P. Mathew, D. Bondeson, and I. Kvien, "Manufacturing process of cellulose whiskers/polylactic acid nanocomposites," *Composites science and technology,* vol. 66, pp. 2776-2784, 2006.

[123] D. Bondeson and K. Oksman, "Dispersion and characteristics of surfactant modified cellulose whiskers nanocomposites," *Composite Interfaces,* vol. 14, pp. 617-630, 2007.

[124] A. J. Svagan, M. A. Azizi Samir, and L. A. Berglund, "Biomimetic polysaccharide nanocomposites of high cellulose content and high toughness," *Biomacromolecules,* vol. 8, pp. 2556-2563, 2007.

[125] A. J. Svagan, M. S. Hedenqvist, and L. Berglund, "Reduced water vapour sorption in cellulose nanocomposites with starch matrix," *Composites Science and Technology,* vol. 69, pp. 500-506, 2009.

[126] A. N. Nakagaito and H. Yano, "The effect of fiber content on the mechanical and thermal expansion properties of biocomposites based on microfibrillated cellulose," *Cellulose,* vol. 15, pp. 555-559, 2008.

[127] W. I. Park, M. Kang, H. S. Kim, and H. J. Jin, "Electrospinning of poly (ethylene oxide) with bacterial cellulose whiskers," in *Macromolecular symposia*, 2007, pp. 289-294.

[128] W. L. E. Magalhaes, X. Cao, and L. A. Lucia, "Cellulose nanocrystals/cellulose core-in-shell nanocomposite assemblies," *Langmuir,* vol. 25, pp. 13250-13257, 2009.

[129] P. Lu and Y.-L. Hsieh, "Cellulose nanocrystal-filled poly (acrylic acid) nanocomposite fibrous membranes," *Nanotechnology,* vol. 20, p. 415604, 2009.

[130] W. Gindl and J. Keckes, "Drawing of self-reinforced cellulose films," *Journal of applied polymer science,* vol. 103, pp. 2703-2708, 2007.

[131] B. Madsen and H. Lilholt, "Physical and mechanical properties of unidirectional plant fibre composites—an evaluation of the influence of porosity," *Composites Science and Technology,* vol. 63, pp. 1265-1272, 2003.

[132] H. Bos, *The potential of flax fibres as reinforcement for composite materials*: Wageningen University and Research, 2004.

[133] O. Khondker, U. Ishiaku, A. Nakai, and H. Hamada, "A novel processing technique for thermoplastic manufacturing of unidirectional composites reinforced with jute yarns," *Composites Part A: Applied Science and Manufacturing,* vol. 37, pp. 2274-2284, 2006.

[134] K. Oksman, L. Wallström, L. A. Berglund, and R. D. T. Filho, "Morphology and mechanical properties of unidirectional sisal–epoxy composites," *Journal of Applied Polymer Science,* vol. 84, pp. 2358-2365, 2002.

[135] G. Romhány, J. Karger-Kocsis, and T. Czigány, "Tensile fracture and failure behavior of thermoplastic starch with unidirectional and cross-ply flax fiber reinforcements," *Macromolecular Materials and Engineering,* vol. 288, pp. 699-707, 2003.

[136] S. Ochi, "Mechanical properties of kenaf fibers and kenaf/PLA composites," *Mechanics of materials,* vol. 40, pp. 446-452, 2008.

[137] E. Bodros, I. Pillin, N. Montrelay, and C. Baley, "Could biopolymers reinforced by randomly scattered flax fibre be used in structural applications?," *Composites Science and Technology,* vol. 67, pp. 462-470, 2007.

[138] P. Sreekumar, P. Albert, G. Unnikrishnan, K. Joseph, and S. Thomas, "Mechanical and water sorption studies of ecofriendly banana fiber-reinforced polyester composites fabricated by rtm," *Journal of Applied Polymer Science,* vol. 109, pp. 1547-1555, 2008.

[139] M. Sain, B. Kokta, and C. Imbert, "Structure-property relationships of wood fiber-filled polypropylene composite," *Polymer-plastics technology and engineering,* vol. 33, pp. 89-104, 1994.

[140] R. Raj, B. V. Kokta, D. Maldas, and C. Daneault, "Use of wood fibers in thermoplastics. VII. The effect of coupling agents in polyethylene–wood fiber composites," *Journal of applied polymer science,* vol. 37, pp. 1089-1103, 1989.

[141] A. R. Sanadi, D. F. Caulfield, R. E. Jacobson, and R. M. Rowell, "Renewable agricultural fibers as reinforcing fillers in plastics: Mechanical properties of kenaf fiber-polypropylene composites," *Industrial & Engineering Chemistry Research,* vol. 34, pp. 1889-1896, 1995.

[142] J. Wright and L. J. Mathias, "New lightweight materials: Balsa wood-polymer composites based on ethyl α-(hydroxymethyl) acrylate," *Journal of applied polymer science,* vol. 48, pp. 2241-2247, 1993.

[143] M. Sain and B. Kokta, "Polyolefin–wood filler composite. I. Performance of m-phenylene bismaleimide-modified wood fiber in polypropylene composite," *Journal of applied polymer science,* vol. 54, pp. 1545-1559, 1994.

[144] H. Dalväg, C. Klason, and H.-E. Strömvall, "The efficiency of cellulosic fillers in common thermoplastics. Part II. Filling with processing aids and coupling agents," *International Journal of Polymeric Materials,* vol. 11, pp. 9-38, 1985.

[145] J. Borges, M. Godinho, A. Martins, D. Stamatialis, M. De Pinho, and M. Belgacem, "Tensile properties of cellulose fiber reinforced hydroxypropylcellulose films," *Polymer composites,* vol. 25, pp. 102-110, 2004.

[146] Q. Wu, M. Henriksson, X. Liu, and L. A. Berglund, "A high strength nanocomposite based on microcrystalline cellulose and polyurethane," *Biomacromolecules,* vol. 8, pp. 3687-3692, 2007.

[147] Z. Xiuju, S. Juncai, Y. Huajun, L. Zhidan, and T. Shaozao, "Mechanical properties, morphology, thermal performance, crystallization behavior, and kinetics of PP/microcrystal cellulose composites compatibilized by two different compatibilizers," *Journal of Thermoplastic Composite Materials,* vol. 24, pp. 735-754, 2011.

[148] A. P. Mathew, K. Oksman, and M. Sain, "Mechanical properties of biodegradable composites from poly lactic acid (PLA) and microcrystalline cellulose (MCC)," *Journal of applied polymer science,* vol. 97, pp. 2014-2025, 2005.

[149] A. Iwatake, M. Nogi, and H. Yano, "Cellulose nanofiber-reinforced polylactic acid," *Composites Science and Technology,* vol. 68, pp. 2103-2106, 2008.

[150] A. P. Mathew, A. Chakraborty, K. Oksman, and M. Sain, "The structure and mechanical properties of cellulose nanocomposites prepared by twin screw extrusion," ed: ACS Publications, 2006.

[151] A. Chakraborty, M. Sain, and M. Kortschot, "Reinforcing potential of wood pulp-derived microfibres in a PVA matrix," 2006.

[152] M. I. Voronova, O. V. Surov, A. V. Afineevskii, and A. G. Zakharov, "Properties of polyacrylamide composites reinforced by cellulose nanocrystals," *Heliyon,* vol. 6, p. e05529, 2020.

[153] L. Forsgren, K. Sahlin-Sjövold, A. Venkatesh, J. Thunberg, R. Kádár, A. Boldizar*, et al.*, "Composites with surface-grafted cellulose nanocrystals (CNC)," *Journal of Materials Science,* vol. 54, pp. 3009-3022, 2019.

[154] Y. Zhang, L. Cui, H. Xu, X. Feng, B. Wang, B. Pukánszky*, et al.*, "Poly (lactic acid)/cellulose nanocrystal composites via the Pickering emulsion approach: Rheological, thermal and mechanical properties," *International journal of biological macromolecules,* vol. 137, pp. 197-204, 2019.

[155] M. Voronova, N. Rubleva, N. Kochkina, A. Afineevskii, A. Zakharov, and O. Surov, "Preparation and characterization of polyvinylpyrrolidone/cellulose nanocrystals composites," *Nanomaterials,* vol. 8, p. 1011, 2018.

[156] H. Sojoudiasli, M. C. Heuzey, and P. J. Carreau, "Mechanical and morphological properties of cellulose nanocrystal-polypropylene composites," *Polymer Composites,* vol. 39, pp. 3605-3617, 2018.

[157] X. Zhang and Y. Zhang, "Poly (butylene succinate-co-butylene adipate)/cellulose nanocrystal composites modified with phthalic anhydride," *Carbohydrate polymers,* vol. 134, pp. 52-59, 2015.

[158] X. Zhang, P. Ma, and Y. Zhang, "Structure and properties of surface-acetylated cellulose nanocrystal/poly (butylene adipate-co-terephthalate) composites," *Polymer Bulletin,* vol. 73, pp. 2073-2085, 2016.

[159] J. Fallon, B. Kolb, C. Herwig, E. Foster, and M. Bortner, "Mechanically adaptive thermoplastic polyurethane/cellulose nanocrystal composites: Process-driven structure–property relationships," *Journal of Applied Polymer Science,* vol. 136, p. 46992, 2019.

[160] M. Feldmann and A. K. Bledzki, "Bio-based polyamides reinforced with cellulosic fibres–processing and properties," *Composites Science and Technology,* vol. 100, pp. 113-120, 2014.

[161] E. Hablot, R. Matadi, S. Ahzi, and L. Avérous, "Renewable biocomposites of dimer fatty acid-based polyamides with cellulose fibres: thermal, physical and mechanical properties," *Composites science and technology,* vol. 70, pp. 504-509, 2010.

[162] Y. Peng, D. J. Gardner, and Y. Han, "Characterization of mechanical and morphological properties of cellulose reinforced polyamide 6 composites," *Cellulose,* vol. 22, pp. 3199-3215, 2015.

[163] K. C. Jajam and H. V. Tippur, "Quasi-static and dynamic fracture behavior of particulate polymer composites: a study of nano-vs. micro-size filler and loading-rate effects," *Composites Part B: Engineering,* vol. 43, pp. 3467-3481, 2012.

[164] J. Cho, M. Joshi, and C. Sun, "Effect of inclusion size on mechanical properties of polymeric composites with micro and nano particles," *Composites Science and Technology,* vol. 66, pp. 1941-1952, 2006.

[165] C. Ng, B. Ash, L. Schadler, and R. Siegel, "A study of the mechanical and permeability properties of nano-and micron-TiO2 filled epoxy composites," *Advanced Composites Letters,* vol. 10, p. 096369350101000301, 2001.

[166] S. Bhavikatti, *Finite element analysis*: New Age International, 2005.

[167] D. C. Rapaport and D. C. R. Rapaport, *The art of molecular dynamics simulation*: Cambridge university press, 2004.

[168] W. Dittrich and M. Reuter, *Classical and quantum dynamics*: Springer, 1994.

[169] B. Ji and H. Gao, "Mechanical properties of nanostructure of biological materials," *Journal of the Mechanics and Physics of Solids,* vol. 52, pp. 1963-1990, 2004.

[170] J. Meng, Y. Zhang, K. Song, and M. L. Minus, "Forming Crystalline Polymer-Nano Interphase Structures for High-M odulus and High-T ensile/S trength Composite Fibers," *Macromolecular Materials and Engineering,* vol. 299, pp. 144-153, 2014.

[171] S. Kundalwal and S. Kumar, "Multiscale modeling of stress transfer in continuous microscale fiber reinforced composites with nano-engineered interphase," *Mechanics of Materials,* vol. 102, pp. 117-131, 2016.

[172] W. Xu, Y. Wu, and M. Jia, "Elastic dependence of particle-reinforced composites on anisotropic particle geometries and reinforced/weak interphase microstructures at nano- and micro-scales," *Composite Structures,* vol. 203, pp. 124-131, 2018.

[173] M. Vacatello, "Chain dimensions in filled polymers: An intriguing problem," *Macromolecules,* vol. 35, pp. 8191-8193, 2002.

[174] M. Vacatello, "Phantom chain simulations of polymer− nanofiller systems," *Macromolecules,* vol. 36, pp. 3411-3416, 2003.

[175] M. Vacatello, "Molecular arrangements in polymer-based nanocomposites," *Macromolecular theory and simulations,* vol. 11, pp. 757-765, 2002.

[176] Z. Liu, Y. Li, and K. Kowk, "Mean interparticle distances between hard particles in one to three dimensions," *Polymer,* vol. 42, pp. 2701-2706, 2001.

[177] J. Kalfus and J. Jancar, "Relaxation processes in PVAc-HA nanocomposites," *Journal of Polymer Science Part B: Polymer Physics,* vol. 45, pp. 1380-1388, 2007.

[178] J. Karger-Kocsis and S. Fakirov, *Nano-and micro-mechanics of polymer blends and composites*: Hanser Munich, 2009.

[179] S. Simonian, "Particle damping applications," in *45th AIAA/ASME/ASCE/AHS/ASC Structures, Structural Dynamics & Materials Conference*, 2004, p. 1906.

[180] A. Fasana, A. Ferraris, D. B. Polato, A. G. Airale, and M. Carello, "Composite and damping materials characterization with an application to a car door," in *The International Conference of IFToMM ITALY*, 2018, pp. 174-184.

[181] J. M. Davis, *Composite materials in engineering structures*: Nova Science Publishers, 2011.

[182] R. Chandra, S. Singh, and K. Gupta, "Damping studies in fiber-reinforced composites–a review," *Composite structures,* vol. 46, pp. 41-51, 1999.

[183] A. Treviso, B. Van Genechten, D. Mundo, and M. Tournour, "Damping in composite materials: Properties and models," *Composites Part B: Engineering,* vol. 78, pp. 144-152, 2015.

[184] A. Etaati, S. A. Mehdizadeh, H. Wang, and S. Pather, "Vibration damping characteristics of short hemp fibre thermoplastic composites," *Journal of Reinforced Plastics and Composites,* vol. 33, pp. 330-341, 2014.

[185] E. Botelho, A. Campos, E. De Barros, L. Pardini, and M. Rezende, "Damping behavior of continuous fiber/metal composite materials by the free vibration method," *composites part B: Engineering,* vol. 37, pp. 255-263, 2005.

[186] M. Rajesh, J. Pitchaimani, and N. Rajini, "Free vibration characteristics of banana/sisal natural fibers reinforced hybrid polymer composite beam," *Procedia Engineering,* vol. 144, pp. 1055-1059, 2016.

[187] A. Patel, R. Das, and S. K. Sahu, "Experimental and numerical study on free vibration of multiwall carbon nanotube reinforced composite plates," *International Journal of Structural Stability and Dynamics,* vol. 20, p. 2050129, 2020.

[188] W. M. Groenewoud, *Characterisation of polymers by thermal analysis*: Elsevier, 2001.

[189] A. Kiziltas, D. J. Gardner, Y. Han, and H.-S. Yang, "Dynamic mechanical behavior and thermal properties of microcrystalline cellulose (MCC)-filled nylon 6 composites," *Thermochimica Acta,* vol. 519, pp. 38-43, 2011.

[190] M. Lahelin, I. Aaltio, O. Heczko, O. Söderberg, Y. Ge, B. Löfgren*, et al.*, "DMA testing of Ni–Mn–Ga/polymer composites," *Composites Part A: Applied Science and Manufacturing,* vol. 40, pp. 125-129, 2009.

[191] S. Mohanty, S. K. Verma, and S. K. Nayak, "Dynamic mechanical and thermal properties of MAPE treated jute/HDPE composites," *Composites Science and Technology,* vol. 66, pp. 538-547, 2006.

[192] D. Romanzini, A. Lavoratti, H. L. Ornaghi Jr, S. C. Amico, and A. J. Zattera, "Influence of fiber content on the mechanical and dynamic mechanical properties of glass/ramie polymer composites," *Materials & Design,* vol. 47, pp. 9-15, 2013.

[193] A. J. Nuñez, J. M. Kenny, M. M. Reboredo, M. I. Aranguren, and N. E. Marcovich, "Thermal and dynamic mechanical characterization of polypropylene-woodflour composites," *Polymer Engineering & Science,* vol. 42, pp. 733-742, 2002.

[194] B. Vieille, W. Albouy, and L. Taleb, "Viscoelastic viscoplastic model for aeronautical thermoplastic laminates at high temperature: Validation on high stress gradient structures," *Composites Part B: Engineering,* vol. 90, pp. 278-286, 2016.

[195] S. Ge, S. Samanta, B. Li, G. P. Carden, P.-F. Cao, and A. P. Sokolov, "Unravelling the Mechanism of Viscoelasticity in Polymers with Phase-Separated Dynamic Bonds," *ACS nano,* 2022.

[196] R. G. Ni and R. Adams, "A rational method for obtaining the dynamic mechanical properties of laminae for predicting the stiffness and damping of laminated plates and beams," *Composites,* vol. 15, pp. 193-199, 1984.

[197] Y. Haddad and J. Feng, "On the trade-off between damping and stiffness in the design of discontinuous fibre-reinforced composites," *Composites Part B: Engineering,* vol. 34, pp. 11-20, 2003.

[198] A. Hadi and J. Ashton, "Measurement and theoretical modelling of the damping properties of a uni-directional glass/epoxy composite," *composite structures,* vol. 34, pp. 381-385, 1996.

[199] J.-M. Berthelot and Y. Sefrani, "Damping analysis of unidirectional glass and Kevlar fibre composites," *Composites science and technology,* vol. 64, pp. 1261-1278, 2004.

[200] L. B. Crema, A. Castellani, and U. Drago, "Damping characteristics of fabric and laminated Kevlar composites," *Composites,* vol. 20, pp. 593-596, 1989.

[201] H. Rajoria and N. Jalili, "Passive vibration damping enhancement using carbon nanotube-epoxy reinforced composites," *Composites Science and Technology,* vol. 65, pp. 2079-2093, 2005.

[202] S. U. Khan, C. Y. Li, N. A. Siddiqui, and J.-K. Kim, "Vibration damping characteristics of carbon fiber-reinforced composites containing multi-walled carbon nanotubes," *Composites science and technology,* vol. 71, pp. 1486-1494, 2011.

[203] M. Botev, H. Betchev, D. Bikiaris, and C. Panayiotou, "Mechanical properties and viscoelastic behavior of basalt fiber-reinforced polypropylene," *Journal of Applied Polymer Science,* vol. 74, pp. 523-531, 1999.

[204] A. Noushini, B. Samali, and K. Vessalas, "Effect of polyvinyl alcohol (PVA) fibre on dynamic and material properties of fibre reinforced concrete," *Construction and Building Materials,* vol. 49, pp. 374-383, 2013.

[205] M. Goodarz, H. Bahrami, M. Sadighi, and S. Saber-Samandari, "Quasi-static indentation response of aramid fiber/epoxy composites containing nylon 66 electrospun nano-interlayers," *Journal of Industrial Textiles,* vol. 47, pp. 960-977, 2018.

[206] L. A. Pothan, Z. Oommen, and S. Thomas, "Dynamic mechanical analysis of banana fiber reinforced polyester composites," *Composites Science and technology,* vol. 63, pp. 283-293, 2003.

[207] B. Wielage, T. Lampke, H. Utschick, and F. Soergel, "Processing of natural-fibre reinforced polymers and the resulting dynamic–mechanical properties," *Journal of materials processing technology,* vol. 139, pp. 140-146, 2003.

[208] K. Cheour, M. Assarar, D. Scida, R. Ayad, and X.-L. Gong, "Effect of water ageing on the mechanical and damping properties of flax-fibre reinforced composite materials," *Composite Structures,* vol. 152, pp. 259-266, 2016.

[209] V. Geethamma, G. Kalaprasad, G. Groeninckx, and S. Thomas, "Dynamic mechanical behavior of short coir fiber reinforced natural rubber composites," *Composites Part A: Applied Science and Manufacturing,* vol. 36, pp. 1499-1506, 2005.

[210] L. Di Landro and W. Lorenzi, "Static and dynamic properties of thermoplastic matrix/natural fiber composites," *Journal of Biobased Materials and Bioenergy,* vol. 3, pp. 238-244, 2009.

[211] R. Gibson, S. Hwang, and H. Kwak, "Micromechanical modeling of damping in composites including interphase effects," in *36th Intern. SAMPE Symposium, Soc. for the Adv. of Mat. and Process Eng., Covina*, 1991, pp. 592-606.

[212] S. Dong and R. Gauvin, "Application of dynamic mechanical analysis for the study of the interfacial region in carbon fiber/epoxy composite materials," *Polymer composites,* vol. 14, pp. 414-420, 1993.

[213] H. L. Ornaghi Jr, A. S. Bolner, R. Fiorio, A. J. Zattera, and S. C. Amico, "Mechanical and dynamic mechanical analysis of hybrid composites molded by resin transfer molding," *Journal of Applied Polymer Science,* vol. 118, pp. 887-896, 2010.

[214] K. Yu, Y. Ding, J. Liu, and Y. Bai, "Energy dissipation characteristics of all-grade polyethylene fiber-reinforced engineered cementitious composites (PE-ECC)," *Cement and Concrete Composites,* vol. 106, p. 103459, 2020.

[215] M. Jalalvand, G. Czél, J. D. Fuller, M. R. Wisnom, L. P. Canal, C. D. González*, et al.*, "Energy dissipation during delamination in composite materials–An experimental assessment of the cohesive law and the stress-strain field ahead of a crack tip," *Composites Science and Technology,* vol. 134, pp. 115-124, 2016.

[216] J. Suhr, W. Zhang, P. M. Ajayan, and N. A. Koratkar, "Temperature-activated interfacial friction damping in carbon nanotube polymer composites," *Nano letters,* vol. 6, pp. 219-223, 2006.

[217] N. A. Koratkar, J. Suhr, A. Joshi, R. S. Kane, L. S. Schadler, P. M. Ajayan*, et al.*, "Characterizing energy dissipation in single-walled carbon nanotube polycarbonate composites," *Applied physics letters,* vol. 87, p. 063102, 2005.

[218] B. J. BRISCOE, "Interfacial friction of polymer composites. General fundamental principles," *Composite materials series,* vol. 1, pp. 25-59, 1986.

[219] W. Carter, E. Fuller Jr, and E. Butler, "Micro-mechanical aspects of asperity-controlled friction in fiber-toughened ceramic composites," *Scripta Metallurgica;(United States),* vol. 25, 1991.

[220] J. Schön, "Coefficient of friction for aluminum in contact with a carbon fiber epoxy composite," *Tribology International,* vol. 37, pp. 395-404, 2004.

[221] M. K. Chaudhury and M. J. Owen, "Adhesion hysteresis and friction," *Langmuir,* vol. 9, pp. 29-31, 1993.

[222] M. P. de Boer, J. A. Knapp, T. A. Michalske, U. Srinivasan, and R. Maboudian, "Adhesion hysteresis of silane coated microcantilevers," *Acta Materialia,* vol. 48, pp. 4531-4541, 2000.

[223] E. Evans, "Probing the relation between force—lifetime—and chemistry in single molecular bonds," *Annual review of biophysics and biomolecular structure,* vol. 30, pp. 105-128, 2001.

[224] J. N. Israelachvili, *Intermolecular and surface forces*: Academic press, 2011.

[225] J. Kenny and M. Marchetti, "Elasto-plastic behavior of thermoplastic composite laminates under cyclic loading," *Composite structures,* vol. 32, pp. 375-382, 1995.

[226] D. Curtis, D. Moore, B. Slater, and N. Zahlan, "Fatigue testing of multi-angle laminates of CF/PEEK," in *Composites Evaluation*, ed: Elsevier, 1987, pp. 40-50.

[227] R. S. Lakes, *Viscoelastic solids*: CRC press, 2017.

[228] R. J. Crawford and P. Martin, *Plastics engineering*: Butterworth-Heinemann, 2020.

[229] B. Jóźwiak, M. Orczykowska, and M. Dziubiński, "Fractional generalizations of maxwell and Kelvin-Voigt models for biopolymer characterization," *PloS one,* vol. 10, p. e0143090, 2015.

[230] R. L. Bagley and P. J. Torvik, "Fractional calculus-a different approach to the analysis of viscoelastically damped structures," *AIAA journal,* vol. 21, pp. 741-748, 1983.

[231] T. Pritz, "Five-parameter fractional derivative model for polymeric damping materials," *Journal of Sound and Vibration,* vol. 265, pp. 935-952, 2003.

[232] M. Razavy, *Classical and quantum dissipative systems*: World Scientific, 2005.

[233] H. Levine, *Unidirectional wave motions*: Elsevier, 2012.

[234] R. J. Rubin, "Momentum autocorrelation functions and energy transport in harmonic crystals containing isotopic defects," *Physical Review,* vol. 131, p. 964, 1963.

[235] M. Razavy, "Wave equation for dissipative systems derived from a quantized many-body problem," *Canadian Journal of Physics,* vol. 58, pp. 1019-1025, 1980.

[236] R. Zhou, W. Gao, L. Xia, H. Wu, and S. Guo, "The study of damping property and mechanism of thermoplastic polyurethane/phenolic resin through a combined experiment and molecular dynamics simulation," *Journal of materials science,* vol. 53, pp. 9350-9362, 2018.

[237] H. Sun, "COMPASS: an ab initio force-field optimized for condensed-phase applications overview with details on alkane and benzene compounds," *The Journal of Physical Chemistry B,* vol. 102, pp. 7338-7364, 1998.

[238] B. S. Khatri and T. C. McLeish, "Rouse model with internal friction: A coarse grained framework for single biopolymer dynamics," *Macromolecules,* vol. 40, pp. 6770-6777, 2007.

[239] L. Zhu, S. Zhao, C. Zhang, X. Cheng, J. Hao, X. Shao*, et al.*, "Effects of chain structure on damping property and local dynamics of phenyl silicone rubber: Insights from experiment and molecular simulation," *Polymer Testing,* vol. 93, p. 106885, 2021.

[240] B. Lauke, "Effect of particle size distribution on debonding energy and crack resistance of polymer composites," *Computational materials science,* vol. 77, pp. 53-60, 2013.

[241] J. Zhang and S. Ghosh, "Molecular dynamics based study and characterization of deformation mechanisms near a crack in a crystalline material," *Journal of the Mechanics and Physics of Solids,* vol. 61, pp. 1670-1690, 2013.

[242] F. F. Abraham and H. Gao, "How fast can cracks propagate?," *Physical Review Letters,* vol. 84, p. 3113, 2000.

[243] G. Formica, M. Talò, and W. Lacarbonara, "Nonlinear modeling of carbon nanotube composites dissipation due to interfacial stick–slip," *International Journal of Plasticity,* vol. 53, pp. 148-163, 2014.

[244] X. Zhou, K.-W. Wang, and C. Bakis, "The investigation of carbon-nanotube-based polymers for improved structural damping," in *Smart Structures and Materials 2004: Damping and Isolation*, 2004, pp. 162-173.

[245] A. Liu, K. Wang, and C. E. Bakis, "Multiscale damping model for polymeric composites containing carbon nanotube ropes," *Journal of composite materials,* vol. 44, pp. 2301-2323, 2010.

[246] L. Prandtl, "Ein Gedankenmodell zur kinetischen Theorie der festen Körper," *ZAMM-Journal of Applied Mathematics and Mechanics/Zeitschrift für Angewandte Mathematik und Mechanik,* vol. 8, pp. 85-106, 1928.

[247] D. Tomanek, W. Zhong, and H. Thomas, "Calculation of an atomically modulated friction force in atomic-force microscopy," *EPL (Europhysics Letters),* vol. 15, p. 887, 1991.

[248] Z.-J. Wang, T.-B. Ma, Y.-Z. Hu, L. Xu, and H. Wang, "Energy dissipation of atomic-scale friction based on one-dimensional Prandtl-Tomlinson model," *Friction,* vol. 3, pp. 170-182, 2015/06/01 2015.

[249] T. Kontorova and J. Frenkel, "On the theory of plastic deformation and twinning. II," *Zh. Eksp. Teor. Fiz.,* vol. 8, pp. 1340-1348, 1938.

[250] M. Weiss and F.-J. Elmer, "Dry friction in the Frenkel-Kontorova-Tomlinson model: Static properties," *Physical review B,* vol. 53, p. 7539, 1996.

[251] A. Filippov, J. Klafter, and M. Urbakh, "Friction through dynamical formation and rupture of molecular bonds," *Physical Review Letters,* vol. 92, p. 135503, 2004.

[252] I. Barel, M. Urbakh, L. Jansen, and A. Schirmeisen, "Multibond dynamics of nanoscale friction: the role of temperature," *Physical Review Letters,* vol. 104, p. 066104, 2010.

[253] A. Erbas, D. Horinek, and R. R. Netz, "Viscous friction of hydrogen-bonded matter," *Journal of the American Chemical Society,* vol. 134, pp. 623-630, 2012.

[254] A. Serr, D. Horinek, and R. R. Netz, "Polypeptide friction and adhesion on hydrophobic and hydrophilic surfaces: a molecular dynamics case study," *Journal of the American Chemical Society,* vol. 130, pp. 12408-12413, 2008.

[255] J. Israelachvili and A. Berman, "Irreversibility, Energy Dissipation, and Time Effects in Intermolecular and Surface Interactions," *Israel Journal of Chemistry,* vol. 35, pp. 85-91, 1995/01/01 1995.

[256] M. Nosonovsky, "Model for solid-liquid and solid-solid friction of rough surfaces with adhesion hysteresis," *The Journal of chemical physics,* vol. 126, p. 224701, 2007.

[257] K. Johnson, "Mechanics of adhesion," *Tribology International,* vol. 31, pp. 413-418, 1998.

[258] W. T. Kern, W. Kim, A. Argento, E. Lee, and D. F. Mielewski, "Mechanical behavior of microcellular, natural fiber reinforced composites at various strain rates and temperatures," *Polymer Testing,* vol. 37, pp. 148-155, 2014.

[259] W. Kim, A. Argento, F. W. Rozsa, and K. Mallett, "Constitutive behavior of ocular tissues over a range of strain rates," *ASME Journal of biomechanical engineering,* vol. 134, p. 061002, 2012.

[260] W. Kim and A. Argento, "11 - High strain rate testing of natural fiber composites," in *Natural Fibre Composites*, A. Hodzic and R. Shanks, Eds., ed: Woodhead Publishing, 2014, pp. 303-322.

[261] W. Kim, A. Argento, C. Flanigan, and D. F. Mielewski, "Effects of soy-based oils on the tensile behavior of EPDM rubber," *Polymer Testing,* vol. 46, pp. 33-40, 9// 2015.

[262] Y. Tian, W. Kim, A. Kiziltas, D. F. Mielewski, and A. Argento, "Effects of interfacial dynamics on the damping of biocomposites," *Submitted for publication,* 2022.

[263] W. T. Kern, W. Kim, A. Argento, E. Lee, and D. F. Mielewski, "Mechanical behavior of microcellular, natural fiber reinforced composites at various strain rates and temperatures," *Polymer testing,* vol. 37, pp. 148-155, 2014.

[264] X. Zhou, E. Shin, K. W. Wang, and C. E. Bakis, "Interfacial damping characteristics of carbon nanotube-based composites," *Composites Science and Technology,* vol. 64, pp. 2425-2437, 2004/11/01/ 2004.

[265] P. M. Ajayan, J. Suhr, and N. Koratkar, "Utilizing interfaces in carbon nanotube reinforced polymer composites for structural damping," *Journal of Materials Science,* vol. 41, pp. 7824-7829, 2006/12/01 2006.

[266] E. E. M. Ahmad and A. S. Luyt, "Morphology, thermal, and dynamic mechanical properties of poly(lactic acid)/sisal whisker nanocomposites," *Polymer Composites,* vol. 33, pp. 1025-1032, 2012/06/01 2012.

[267] Y. Tian, W. Kim, K. Elise, A. Kiziltas, D. Mielewski, and A. Argento, "Damping of micro- and nanocellulose reinforced PA610 composites and influences of moisture absorption," *submitted,* 2022.

[268] A. Erbaş, D. Horinek, and R. R. Netz, "Viscous Friction of Hydrogen-Bonded Matter," *Journal of the American Chemical Society,* vol. 134, pp. 623-630, 2012/01/11 2012.

[269] A. Kiziltas, D. J. Gardner, Y. Han, and H.-S. Yang, "Dynamic mechanical behavior and thermal properties of microcrystalline cellulose (MCC)-filled nylon 6 composites," *Thermochimica Acta,* vol. 519, pp. 38-43, 2011/05/20/ 2011.

[270] A. Shenoy and D. Saini, "Rheological models for unified curves for simplified design calculations in polymer processing," *Rheologica acta,* vol. 23, pp. 368-377, 1984.

[271] W. T. Kern, W. Kim, A. Argento, E. C. Lee, and D. F. Mielewski, "Finite element analysis and microscopy of natural fiber composites containing microcellular voids," *Materials & Design,* vol. 106, pp. 285-294, 2016.

[272] M. A. Ashraf, W. Peng, Y. Zare, and K. Y. Rhee, "Effects of Size and Aggregation/Agglomeration of Nanoparticles on the Interfacial/Interphase Properties and Tensile Strength of Polymer Nanocomposites," *Nanoscale Research Letters,* vol. 13, p. 214, 2018/07/17 2018.

[273] N. Jouault, P. Vallat, F. Dalmas, S. Said, J. Jestin, and F. Boué, "Well-Dispersed Fractal Aggregates as Filler in Polymer−Silica Nanocomposites: Long-Range Effects in Rheology," *Macromolecules,* vol. 42, pp. 2031-2040, 2009/03/24 2009.

[274] I. E. Dzyaloshinskii, E. M. Lifshitz, and L. P. Pitaevskii, "The general theory of van der Waals forces," *Advances in Physics,* vol. 10, pp. 165-209, 1961.

[275] N. Yu and A. A. Polycarpou, "Adhesive contact based on the Lennard–Jones potential: a correction to the value of the equilibrium distance as used in the potential," *Journal of Colloid and Interface Science,* vol. 278, pp. 428-435, 2004.

[276] K. Johnson and J. Woodhouse, "Stick–slip motion in the atomic force microscope," *Tribology Letters,* vol. 5, pp. 155-160, 1998.

[277] O. K. Dudko, A. E. Filippov, J. Klafter, and M. Urbakh, "Beyond the conventional description of dynamic force spectroscopy of adhesion bonds," *Proceedings of the National Academy of Sciences,* vol. 100, pp. 11378-11381, 2003.

[278] F. Heslot, T. Baumberger, B. Perrin, B. Caroli, and C. Caroli, "Creep, stick-slip, and dry-friction dynamics: Experiments and a heuristic model," *Physical review E,* vol. 49, p. 4973, 1994.

[279] G. A. Jeffrey and W. Saenger, *Hydrogen bonding in biological structures*: Springer Science & Business Media, 2012.

[280] H. Zeng, M. Tirrell, and J. Israelachvili, "Limit Cycles in Dynamic Adhesion and Friction Processes: A Discussion," *The Journal of Adhesion,* vol. 82, pp. 933-943, 2006/09/01 2006.

[281] V. M. Muller, V. S. Yushchenko, and B. V. Derjaguin, "On the influence of molecular forces on the deformation of an elastic sphere and its sticking to a rigid plane," *Journal of Colloid and Interface Science,* vol. 77, pp. 91-101, 1980/09/01/ 1980.

[282] H. C. Hamaker, "The London—van der Waals attraction between spherical particles," *Physica,* vol. 4, pp. 1058-1072, 1937/10/01/ 1937.

[283] S. L. Mayo, B. D. Olafson, and W. A. Goddard, "DREIDING: a generic force field for molecular simulations," *Journal of Physical chemistry,* vol. 94, pp. 8897-8909, 1990.

[284] W. Deng and H. Kesari, "Depth-dependent hysteresis in adhesive elastic contacts at large surface roughness," *Scientific reports,* vol. 9, pp. 1-12, 2019.

[285] C. Yang, U. Tartaglino, and B. N. J. Persson, "Influence of Surface Roughness on Superhydrophobicity," *Physical Review Letters,* vol. 97, p. 116103, 09/14/ 2006.

[286] H. Kesari, J. C. Doll, B. L. Pruitt, W. Cai, and A. J. Lew, "Role of surface roughness in hysteresis during adhesive elastic contact," *Philosophical Magazine Letters,* vol. 90, pp. 891-902, 2010/12/01 2010.

[287] M. Holmberg, J. Berg, S. Stemme, L. Ödberg, J. Rasmusson, and P. Claesson, "Surface Force Studies of Langmuir–Blodgett Cellulose Films," *Journal of Colloid and Interface Science,* vol. 186, pp. 369-381, 1997/02/15/ 1997.

[288] L. Bergström, S. Stemme, T. Dahlfors, H. Arwin, and L. Ödberg, "Spectroscopic Ellipsometry Characterisation and Estimation of the Hamaker Constant of Cellulose," *Cellulose,* vol. 6, pp. 1-13, 1999/03/01 1999.

[289] F. L. Leite, C. C. Bueno, A. L. Da Róz, E. C. Ziemath, and O. N. Oliveira, "Theoretical Models for Surface Forces and Adhesion and Their Measurement Using Atomic Force Microscopy," *International Journal of Molecular Sciences,* vol. 13, 2012.

[290] S. P. S. Chundawat, G. Bellesia, N. Uppugundla, L. da Costa Sousa, D. Gao, A. M. Cheh*, et al.*, "Restructuring the Crystalline Cellulose Hydrogen Bond Network Enhances Its Depolymerization Rate," *Journal of the American Chemical Society,* vol. 133, pp. 11163-11174, 2011/07/27 2011.

[291] Y. Dong, A. Vadakkepatt, and A. Martini, "Analytical Models for Atomic Friction," *Tribology Letters,* vol. 44, p. 367, 2011/09/17 2011.

[292] T. D. Jacobs, K. E. Ryan, P. L. Keating, D. S. Grierson, J. A. Lefever, K. T. Turner*, et al.*, "The effect of atomic-scale roughness on the adhesion of nanoscale asperities: a combined simulation and experimental investigation," *Tribology Letters,* vol. 50, pp. 81-93, 2013.

[293] W. C. Swope, H. C. Andersen, P. H. Berens, and K. R. Wilson, "A computer simulation method for the calculation of equilibrium constants for the formation of physical clusters of molecules: Application to small water clusters," *The Journal of Chemical Physics,* vol. 76, pp. 637-649, 1982/01/01 1982.

[294] W. Choi, A. Abraham, J. Ko, J. G. Son, J. Cho, B.-I. Sang*, et al.*, "Anisotropic Alignment of Bacterial Nanocellulose Ionogels for Unconventionally High Combination of Stiffness and Damping," *ACS Applied Materials & Interfaces,* 2022.

[295] H. Kesari, J. C. Doll, B. L. Pruitt, W. Cai, and A. J. Lew, "Role of surface roughness in hysteresis during adhesive elastic contact," *Philosophical Magazine & Philosophical Magazine Letters,* vol. 90, pp. 891-902, 2010.

[296] Y. Wang, K. Kho, W. S. Cheow, and K. Hadinoto, "A comparison between spray drying and spray freeze drying for dry powder inhaler formulation of drug-loaded lipid–polymer hybrid nanoparticles," *International journal of pharmaceutics,* vol. 424, pp. 98-106, 2012.